MILLIMETER-WAVE MONOLITHIC SCHOTTKY DIODE IMAGING ARRAYS

Thesis by

Chung-en Zah

In Partial Fulfillment of the Requirements

for the Degree of

Doctor of Philosophy

California Institute of Technology

Pasadena, California

1986

(Submitted July 30, 1985)

TO MY PARENTS

Acknowledgments

I would like to express my deepest appreciation to Professor David Rutledge, my thesis advisor, for his constant support and encouragement throughout my graduate studies at Caltech. His excellent guidance and insights stimulated me and made this work possible.

In the course of doing this work, many people have assisted me and offered their support. I am indebted to Professors William Bridges, Marc-Aurele Nicolet and Amnon Yariv at Caltech, and to Professors Neville Luhmann, Jr. and Harold Fetterman at UCLA, for the use of their facilities. I am especially thankful to Mr. Steve Smith and Dr. Tom Koch for growing the epitaxial wafers for my experiment. I would like to thank Dr. Zeev Ray-Noy for his collaboration during the early stage of my diode fabrication, Richard Compton for his collaboration in antenna efficiency calculations and Dayalan Kasilingam for his mixer calculations. My thanks are also due to Frank So and Ali Ghaffari for proton implantation, John Gilbert for taking SEM pictures, Perry McDonald and Sung Kim for their assistance in measurements. In addition, I thank Mrs. Joyce Liddell for her assistance and every member of the Millimeter-Wave Integrated-Circuit group, past and present, for their friendship.

Financially, I am grateful to the support from Caltech, Rockwell Graduate Fellowship and Li-Ming Scholarship.

My biggest debt is to my wife, Li Fung Chang, for her support, consideration and skillful typesetting of the manuscript.

Millimeter-Wave Monolithic Schottky Diode Imaging Arrays

Abstract

Inexpensive and compact imaging systems with high sensitivity are needed for millimeter waves. In this study, the calculated efficiencies of elementary integrated-circuit feed antennas show that the antennas with substrate lenses are potentially better feeds than those without substrate lenses. Planar Schottky diodes are integrated with bow-tie antennas to form a one dimensional array. The energy is focused onto the antenna through a silicon lens placed on the back of the gallium-arsenide substrate. Putting a polystyrene cap on the silicon lens has been demonstrated to be an effective way to reduce the reflection loss. A self-aligning process together with proton isolation has been developed to make the planar Schottky diodes with a 1.1-THz zero-bias cutoff frequency. The antenna coupling efficiency and imaging properties of the system are studied by video detection measurements at 94 GHz. As a heterodyne receiver, a double-sideband mixer conversion loss of 11.2 dB and noise temperature of 3770°K have been achieved at a local oscillator frequency of 91 GHz.

TABLE OF CONTENTS

Chapter 1

Introduction

1.1. Motivation

The frequency range of millimeter waves is from 30 GHz to 300 GHz, corresponding to wavelengths of 10 mm to 1 mm. It lies between microwaves and infrared. The three principal characteristics of millimeter waves, that is, short wavelengths, large bandwidth and interaction with atmospheric constituents, make millimeter-wave systems ideal candidates for many applications [1,2] in radars, radiometry [3], plasma diagnosis [4], spectroscopy, and communication [5]. In general, millimeter-wave imaging systems have better resolution than microwave radars and are less affected by smoke and fog than infrared imagers. Therefore, there is a need of millimeter-wave imaging systems.

In imaging, an array of detectors and associated antennas can partially reduce or even completely eliminate the mechanical scanning. It is absolutely necessary for imaging fast changing objects. It allows longer integration time for each detector in an array than a single detector system does. This improves the signal-to-noise ratio.

In millimeter wavelengths, metal waveguides and horns become lossy and expensive to build due to their small dimensions. In addition, it is difficult to form arrays. Quasi-optical structures become more attractive [6,7]. Since the typical detectors such as Schottky diodes are much smaller than a wavelength, they require an antenna to provide a large effective area. This antenna serves the same function as a feed horn in a microwave system. Lens-coupled antennas like the one shown in Fig. 1.1 have been widely used in monolithic circuits [8,9,10]. The idea is that energy is focused onto an antenna through a lens placed on the back of the substrate. This eliminates losses to substrate modes and takes

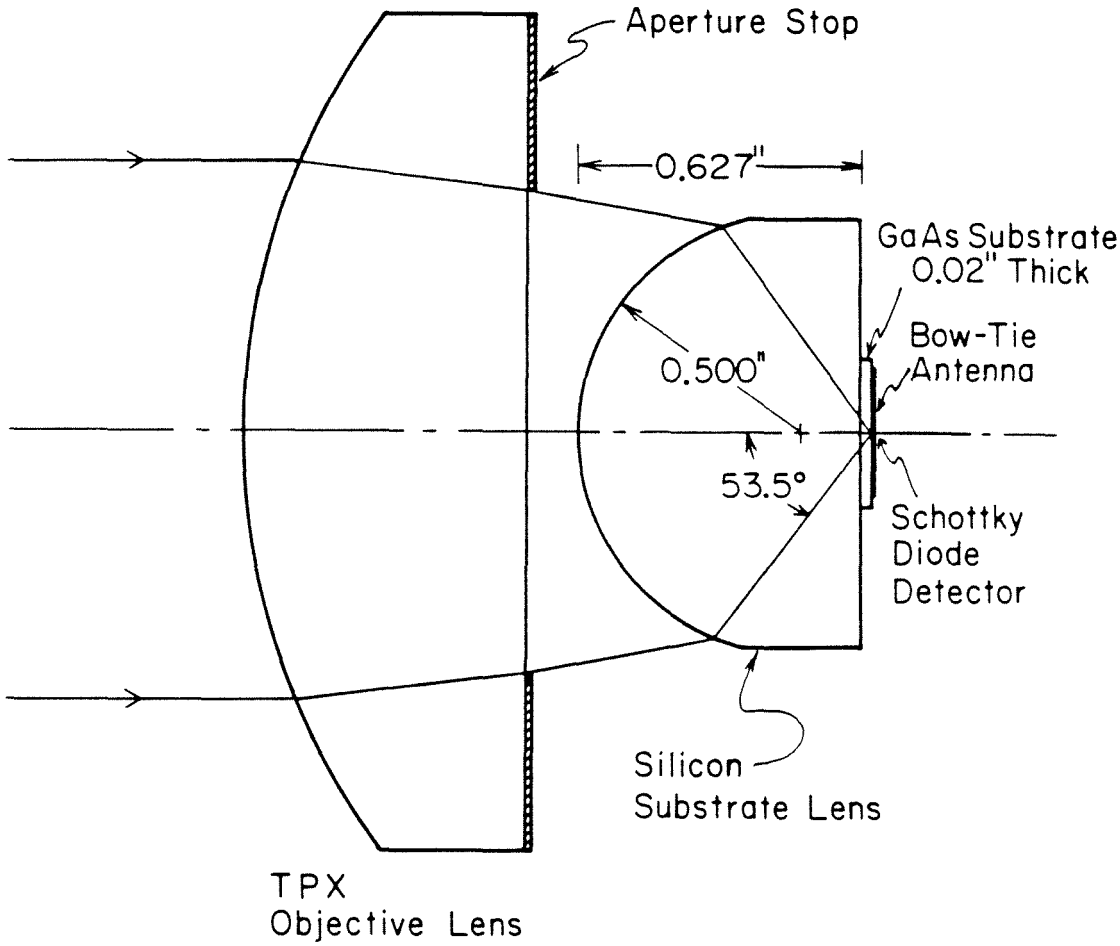

Fig. 1.1. Lens-coupled antenna used in this work

advantage of the fact that antennas on a substrate are more sensitive to radiation from the substrate side [11]. With this coupling structure, imaging arrays have been demonstrated by integrating bolometers with bow-tie antennas on quartz substrates [8,12,13].

Because there are few powerful millimeter-wave sources, it is desirable to have sensitive detectors. The Schottky diode is one of the most sensitive detectors in room temperature applications. Excellent results have been obtained with pointed-contacted Schottky diodes in waveguides [14] and quasi-optical mixer mounts [6], but the assembly is labor-intensive, time consuming, and expensive. Beam-lead Schottky diodes are fragile, and have considerable parasitic inductance and capacitance. These diodes are not suitable for making an array. Monolithic integration of a single planar Schottky diode with a slot antenna on a semi-insulating GaAs substrate has been demonstrated [15]. By integrated-circuit technology, making an array with many planar Schottky diodes and antennas together is no more complicated than making a single planar Schottky diode.

This is the motivation for making a millimeter-wave Monolithic Schottky diode imaging array with lens-coupled antennas. In this work, imaging arrays have been made by integrating the planar Schottky diodes (see Fig. 1.2) with bow-tie antennas (see Fig. 1.3) on semi-insulating gallium-arsenide substrate. This will lead to inexpensive and compact imaging systems with high sensitivity, which are desirable for missiles, satellites, and aircraft. Our imaging arrays were designed for 94 GHz since this frequency is in one of the low absorption windows in the atmosphere.

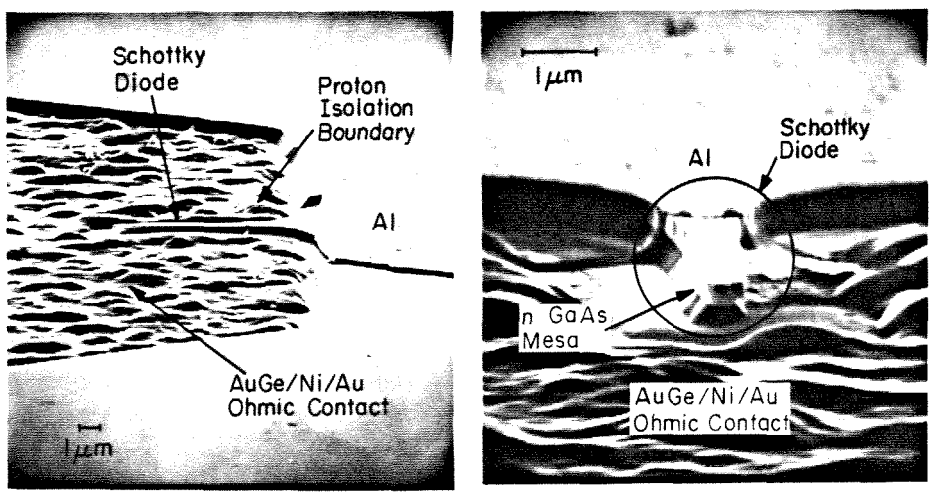

Fig. 1.2. SEM photograph of a planar Schottky diode. Side view (left) and head-on view (right).

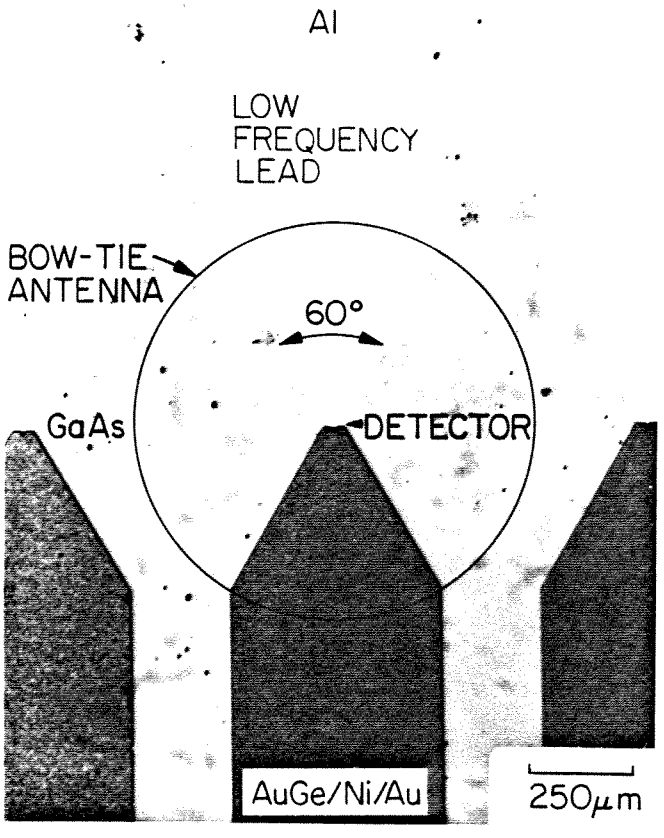

Fig. 1.3. Imaging array with a planar Schottky diode at the apex of each bow-tie antenna.

1.2. Overview of the Thesis

Chapter 2 discusses the calculated efficiencies of elementary integrated-circuit feed antennas considering both the substrate and optics [16]. The effect of substrate lenses, anti-reflection coatings, and adjustable backshorts is also considered. The purpose is to understand the system, make comparisons, and point to the promising antennas.

Chapter 3 presents a polystyrene cap for matching a silicon lens at millimeter wavelengths. The cap is 0.5 mm thick, made by thermal molding. It reduces the reflection loss at 94 GHz by 1.5 dB. The theory and the measured results will be described [17].

Chapter 4 describes the important features about how to fabricate and package our Schottky diode imaging arrays [9]. A self-aligning process together with proton isolation has been developed to make the planar Schottky diodes with a 1.1-THz zero-bias cutoff frequency. Appendix A gives the detailed fabrication process. The measured DC parameters of the Schottky diodes will be compared with the theoretical values. Appendix B describes the curve fitting procedure for the measured I–V characteristics of Schottky diodes. Appendix C is concerned with the theoretical series resistance and capacitance of the planar Schottky diodes.

Chapter 5 is devoted to video detection [18]. By comparing experimental results with theoretical predictions, we will be able to obtain some useful information about our imaging systems and devices, such as the optimum f-number of the objective lens, parasitic capacitance, antenna efficiency and imaging properties. Appendix D includes the theoretical calculation of system video responsivity.

Finally, in Chapter 6 we present the measured double-sideband (DSB) and single-sideband (SSB) heterodyne results [18]. The performance was evaluated under different DC and local oscillator power biases. Appendix E describes diplexers used in our measurement to combine the signal and the local oscillator power into a single beam. Appendix F is concerned with hot and cold measurements from which the DSB conversion loss and noise temperature were determined.

Rcferences

[1] J. C. Wiltse, "Introduction and Overview of Millimeter Waves," *Infrared and MIllimeter Waves*, Chap. 1, pp. 1–17, K. J. Button, ed., Academic Press, Inc., New York, 1981.

[2] P. Bhartia and I. J. Bahl, "Millimeter Wave Applications and Systems," *Millimeter Wave Engineering and Applications*, Chap 10, pp. 617–682, John Wiley & Sons, Inc., 1984.

[3] B. L. Ulich et al., "Absolute Brightness Temperature Measurements at 3.5 mm Wavelength," *IEEE* vol. AP–28, No. 3, pp. 367–377, May, 1980.

[4] N. C. Luhmann, Jr., "Instrumentation and Techniques for Plasma Diagnostics: An Overview," *Infrared and Millimeter Waves*, Chap. 1, pp. 1–66, K. J. Button, ed., Academic Press, Inc., 1979.

[5] K. Miyanchi, "Millimeter-Wave Communications," *Infrared and Millimeter Waves*, Chap. 1, pp. 1–94. K. J. Button, ed., Academic Press, Inc., New York, 1983.

[6] A. R. Kerr, P. H. Siegel and R. J. Mattauch, "A Simple Quasi-Optical Mixer for 100–120 GHz," *IEEE*, MTT–S, pp. 96–98, 1977.

[7] L. Yuan, J. Paul and P. Yeh, "140 GHz Quasi-Optical Planar Mixers," *IEEE*, MTT–S, S–5, pp. 374–375, 1982.

[8] D. P. Neikirk et al., "Far-Infrared Imaging Antenna Arrays," *Appl. Phys. Lett.*, vol. 40, pp. 203–205, 1982.

[9] C. Zah et al., "Progress in Monolithic Schottky Diode Imaging Arrays," *9th Int. Conf. on Infrared and Millimeter Wave*, Osaka, Japan, W–4–2, Oct. 1984.

[10] M. J. Wengler et al., "A Low Noise Receiver for Millimeter and Submillimeter

Wavelength," to be published, *Int. J. of Infrared and Millimeter Waves.*

[11] D. B. Rutledge, D. P. Neikirk and D. P. Kasilingam, "Integrated-Circuit Antennas," *Infrared and Millimeter Waves*, vol. 10, Chap. 1, pp. 1–90, K. J. Button, ed., Academic Press, Inc., New York, 1983.

[12] P. P. Tong et al., "Tracking Antenna Arrays for Near-Millimeter Waves," *IEEE*, vol. AP–31, No. 5, pp. 512–515, May, 1983.

[13] P. P. Tong, "Imaging Polarimeter Arrays for Near-Millimeter Waves," *IEEE*, vol. MTT–32, No. 5, pp. 507–512, May 1984.

[14] J. W. Archer and M. T. Faber, "A Very Low Noise Receiver for 80–120 GHz," *Int. J. Infrared and Millimeter Waves*, vol. 5, No. 8, pp. 1069–1081, Aug. 1984.

[15] B. J. Clifton et al., "High-Performance Quasi-Optical GaAs Monolithic Mixer at 110 GHz," *IEEE*, vol. ED–28, No. 2, pp. 155–157, Feb. 1981.

[16] C. Zah, R. C. Compton and D. B. Rutledge, "Efficiencies of Elementary Integrated-Circuit Feed Antennas," *Electromagnetics*, vol. 3, pp. 239–254, 1984.

[17] C. Zah and D. B. Rutledge, "A Polystyrene Cap for Matching a Silicon Lens at Millimeter Wavelengths," to be published in *J. of Infrared and Millimeter Waves*, Sept. 1985.

[18] C. Zah et al., "Millimeter-Wave Monolithic Schottky Diode Imaging Arrays," to be submitted for publication.

CHAPTER 2

Efficiencies of Elementary Integrated-Circuit Feed Antennas

Efficiencies of elementary integrated-circuit feed antennas are calculated considering both the substrate and the optics. Calculations are made for dielectric constants of 4, for fused-quartz substrates, and 12, for silicon and gallium-arsenide substrates. The effect of substrates lenses, anti-reflection coatings, and adjustable backshorts is also considered. A feed efficiency of 60% is predicted for a slot on a substrate and substrate lens with dielectric constant 12, and 63% for dipole on a substrate with dielectric constant 12 and lens of dielectric constant 4.

2.1. Integrated-Circuit Antennas

Millimeter waves are becoming important in many scientific and military applications. There is a need for monolithic integrated circuits for imaging systems that combine diodes, transistors, antennas and amplifiers on the same substrate [1,2]. In these systems, the antennas are the feeds for lenses and reflectors, and are usually thin-film metal patterns evaporated on substrates such as quartz, silicon, and gallium arsenide. Many different integrated-circuit antennas have been developed, including V antennas [3], Vivaldi antennas [4,24], dielectric-rod antennas [5,6], slots [7,8], slot arrays [9,10], dipole arrays [11], bow-ties [12,23], and circular slots [13]. In these antennas, the substrate is necessary for support, but it also affects the antenna pattern, and the efficiency through its substrate modes. Alexopoulos et al. [14,22] and Pozar [15] have investigated how these modes affect the radiation efficiency of elementary integrated-circuit antennas and resonant microstrip dipoles, and found the substrate modes important, par-

ticularly for high dielectric constants. The optics is also important. Yngvesson has looked at this, finding the aperture efficiency of different optical system [16], but the actual integrated-circuit antenna patterns were not considered in the analysis. The effect of substrate lenses has not been studied either. In this chapter we look at both parts of the problem, and see how the substrate and the optics together determine the feed efficiency of several elementary integrated-circuit antennas. The purpose is to understand the systems, make comparisons, and point to the promising antennas. The calculations are approximate because the patterns are those of elementary antennas rather than the resonant ones used in practice, and because diffraction-limited optics is assumed. Nevertheless, the results are useful because the radiation patterns of elementary antennas usually differ only slightly from the resonant patterns, and because it is relatively easy to make diffraction-limited optics at millimeter wavelengths.

The only efficiency measurements that have been reported for millimeter-wave integrated-circuit antennas are for a silicon waveguide antenna at 85 GHz [6] and for bow-ties in a 1.2 mm imaging array on a fused-quartz substrate and lens [1]. In these antennas there are additional losses from absorption in the dielectric and in the conductors. The efficiency of the silicon antenna was 50%. The efficiency of a single bow-tie, including absorption loss, was 25%. The efficiency for the array was 50%, with the additional power being received by neighboring antennas.

Fig. 2.1 shows the different antenna configurations: a dipole (a) and a slot (b) on a substrate with a lens, a dipole (c) and a slot (d) on underground substrates, and a microstrip dipole (e). The calculations are for substrates with dielectric constants of 4 (to approximate a fused-quartz substrate), and 12 (for the semiconductors silicon and gallium arsenide). We begin with antennas on substrates

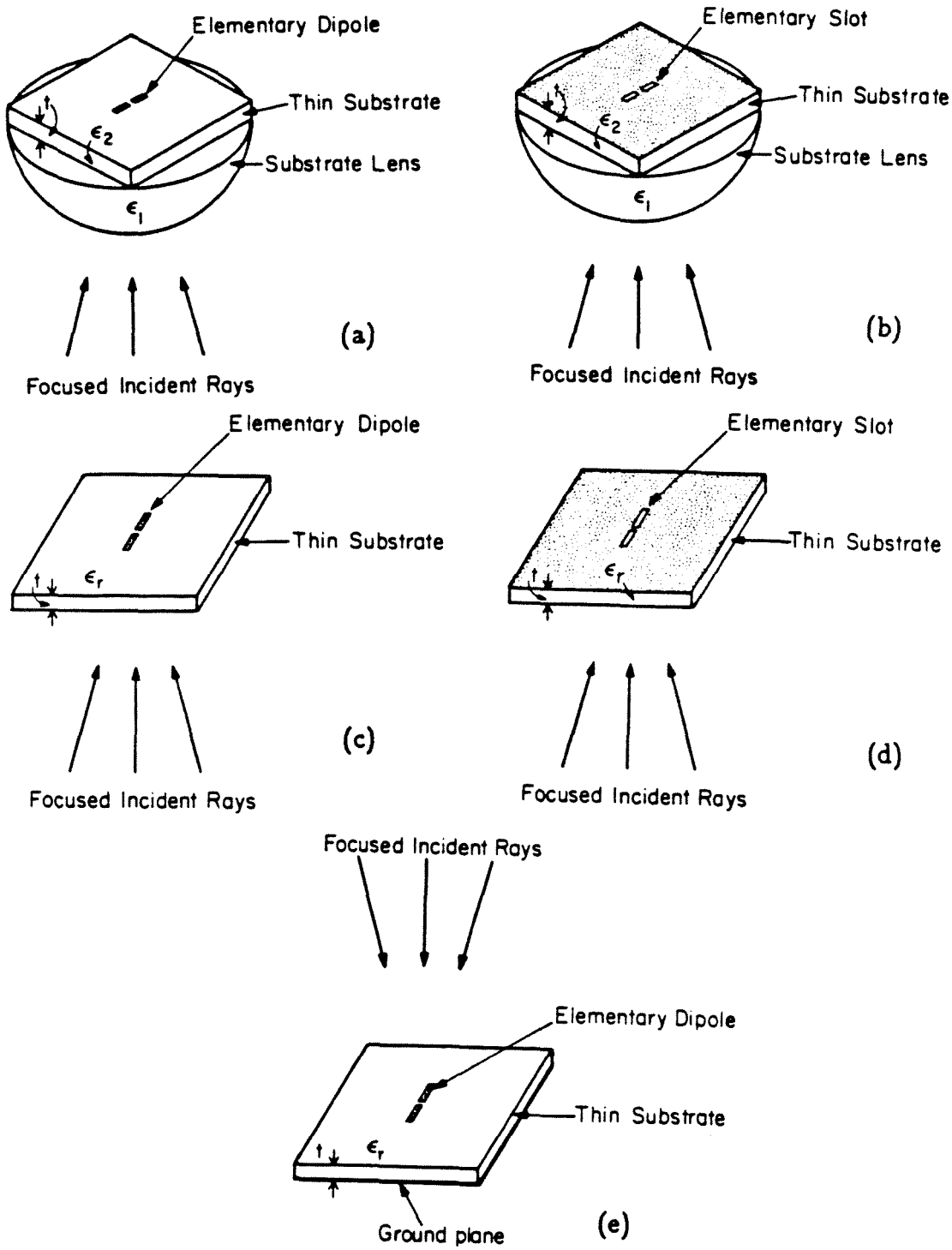

Fig. 2.1. Elementary integrated-circuit antennas: Substrate-lens coupled dipole (a) and slot (b), dipole (c) and slot (d) on an ungrounded substrate, and microstrip dipole (e).

and lenses that have the same dielectric constant. Calculations were also made for a quartz lens on a semiconductor substrate. In addition, the effect of an anti-reflection coating and an adjustable shorting plane behind the substrate are considered.

2.2. Theory

The antenna efficiency is found in reception as the ratio of the power available at the antenna terminals to the power incident on the lens. By reciprocity this efficiency is the same for a transmitting system. In all cases, it is assumed that there is a primary objective lens that is thin, lossless and aberration free (Fig. 2.2). The substrate lenses are assumed to be aspheric hyperhemisphere [1]. The substrate lens reflection loss is taken into account, but absorption loss is neglected because it varies with the wavelength, the quality of the material, and the temperature. The system is characterized by a maximum angle α. For antennas without substrate lenses, α is related to the f-number of the primary by the formula [20]

$$f-\text{number} = 1/(2\sin\alpha). \tag{2.1}$$

For an antenna with a substrate lens that is an aspheric hyperhemisphere, the f-number of the primary increases by a factor of n [1], because of refraction at the substrate lens.

For a dipole, the feed efficiency is found by calculating the open-circuit voltage V and the radiation resistance R, and for the slots, the short-circuit current I and the radiation conductance G. Determining V for the dipoles and I for the slots requires the focused fields, which are computed by integrating the angular spectrum of rays focused by the primary objective lens [18]. To take account of the substrate, we weighted this spectrum by the transmission coefficients for the

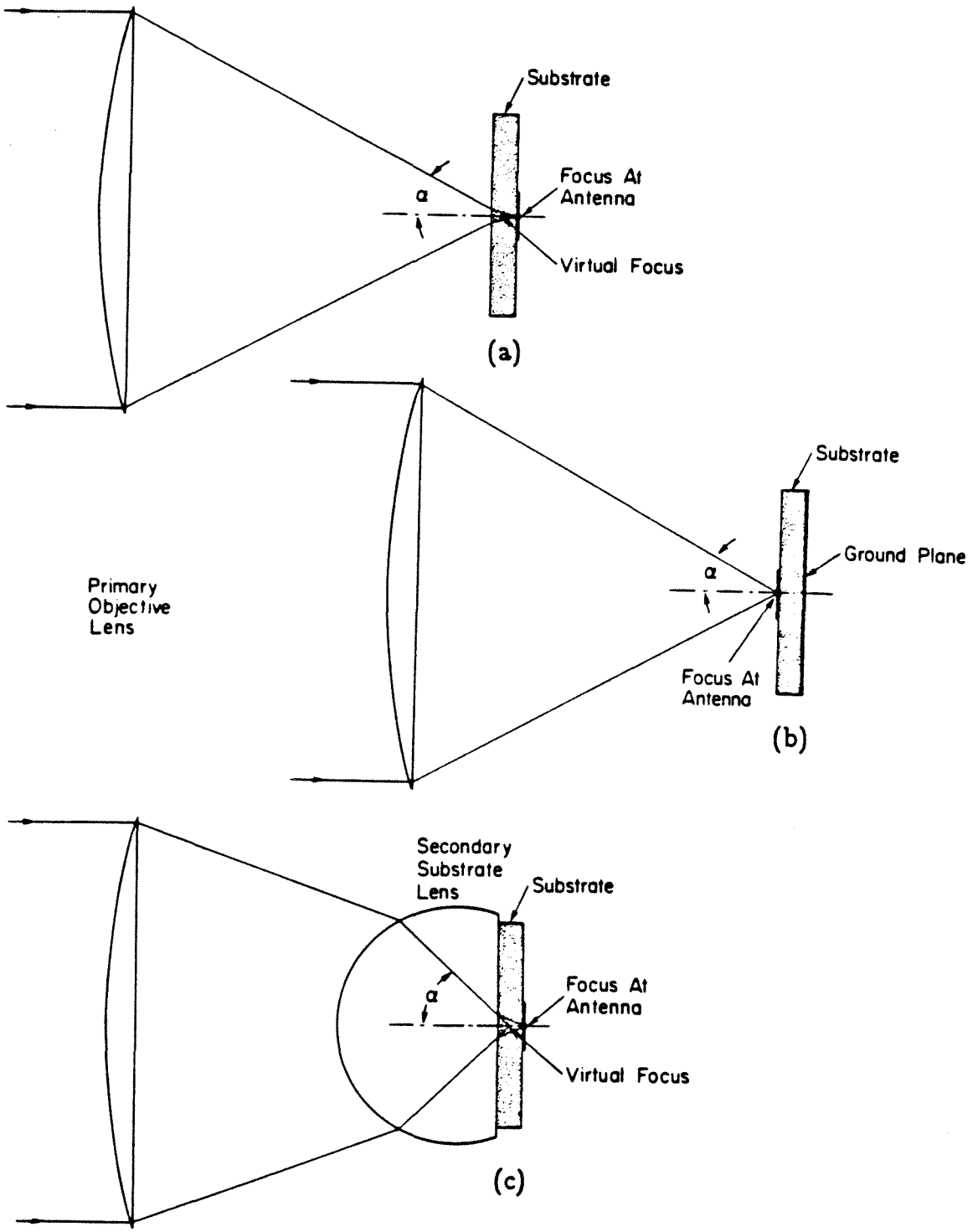

Fig. 2.2. The geometry of the focused beam for antennas on an ungrounded substrate (a), for a microstrip dipole (b), and for antennas with a substrate lens (c).

fields, which are calculated by a transmission-line analogy [19].

When there is no substrate lens, the magnitude of the electric field at the dipole is

$$E = \left(E_i \pi f/\lambda_0\right) \int_{\cos\alpha}^{1} (\tau_{te} + \tau_{tm} x)\, x^{-3/2} dx, \tag{2.2}$$

where E is the electric field at the focus, E_i is the incident electric field at the primary lens, f is the focal length of the primary, λ_0 is the wavelength in free space, α is the maximum angle of incidence shown in Fig. 2.2a and 2.2b, and τ_{te} and τ_{tm} are the transmission coefficients for the electric field, given by the ratio of the electric field at the focus to the electric field at the virtual focus. The magnetic field that we need for the slot is given by a similar expression,

$$H = (H_i \pi f/\lambda_0) \int_{\cos\alpha}^{1} (\tau_{te} x + \tau_{tm})\, x^{-3/2} dx, \tag{2.3}$$

where H_i is the incident magnetic field, and τ_{te} and τ_{tm} are now transmission coefficients for the magnetic field. Once the focused fields are known, it can be shown [21] that V is the product of the focused electric field and the effective length of the dipole, and similarly that I is the product of the focused magnetic field and the effective length of the slot. When there is a substrate lens (Fig. 2.2c), the formula for the electric field becomes

$$E = (E_i \pi f/\lambda_0) \int_{\cos\alpha}^{1} (t_{te}\tau_{te} + t_{tm}\tau_{tm} x) \frac{n^{3/2} x^{1/2}}{n^2 - 1 + x^2}\, dx, \tag{2.4}$$

where t_{te} and t_{tm} are the square roots of the transmittances at the surface of the substrate lens, and n is the refractive index of the substrate lens. For the magnetic field,

$$H = (H_i \pi f/\lambda_0) \int_{\cos\alpha}^{1} (t_{te}\tau_{te} x + t_{tm}\tau_{tm}) \frac{n^{5/2} x^{1/2}}{n^2 - 1 + x^2}\, dx. \tag{2.5}$$

These last two formulas reduce to the formulas for antennas without a substrate lens in the limit that n approaches 1.

The quantities R and G are calculated from the total power radiated from a transmitting antenna. This power, including both power that goes into the air and power trapped in substrate modes, was determined by reciprocity in the way described by Alexopoulos et al. [14]. If necessary, it is easy here to calculate the spillover loss, the transmitted power that misses the primary. For the dipole, we can write

$$R = \frac{2P_d}{I^2}, \tag{2.6}$$

where P_d is the total power radiated by dipole when excited by a current I. For the slot, we have

$$G = \frac{2P_s}{V^2}, \tag{2.7}$$

where P_s is the total power radiated by the slot by the voltage V. Once these quantities are known, we can write the available power for dipoles as $V^2/(8R)$ and for slots as $I^2/(8G)$, and efficiency is just the ratio of this power to the incident power on the objective lens. The integrals in the expressions were evaluated by Simpson's rule on IBM personal computers.

2.3. Results

Fig. 2.3 shows the efficiencies of dipoles on substrates with lenses with identical dielectric constants. The antenna efficiency may be considered as the product of two independent efficiencies: spillover and taper. The spillover efficiency is the fraction of the total radiated power that impinges on the primary lens. The taper efficiency results from non-uniform illumination of the primary, and in this case, includes substrate-lens reflection losses and cross-polarization losses. For a dielectric constant of 4 (Fig. 2.3a), the spillover efficiency improves as α increases, reaching 93% at 90°. The remaining 7% is lost power transmitted into the air behind the substrate. The taper efficiency, on the other hand, is best at small

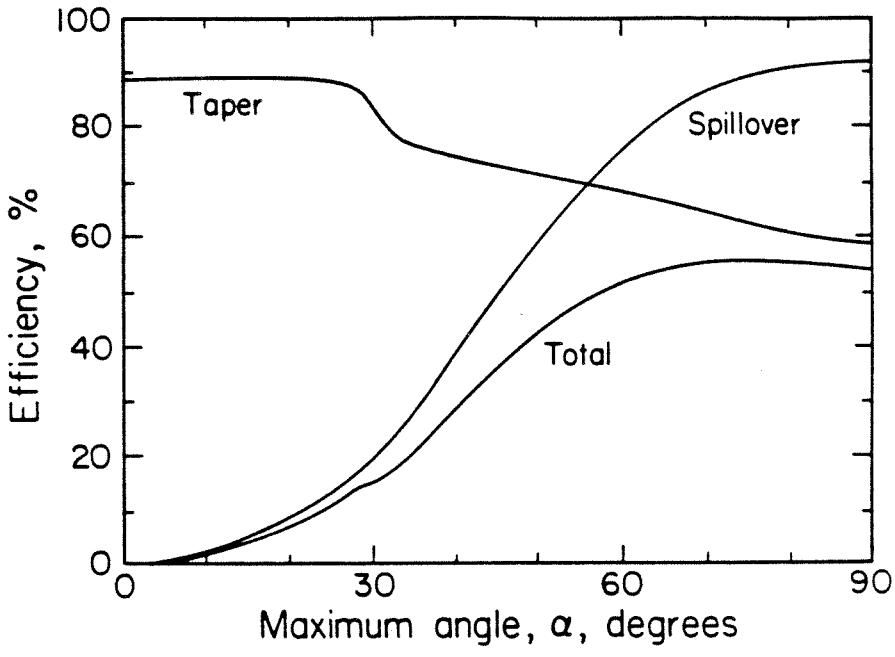

(a)

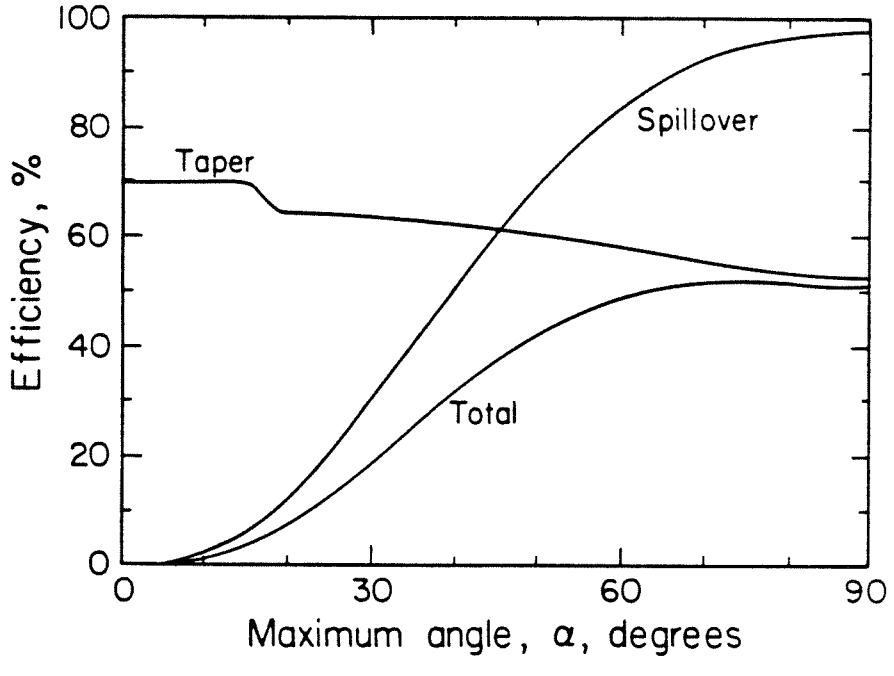

(b)

Fig. 2.3. Efficiency of dipoles with substrate lenses plotted against α for an ϵ_r of 4 (a) and 12 (b).

angles, where it is only limited by reflection loss. There is a drop at the critical angle that can be understood if we consider that dipole pattern varies rapidly at this angle [1], and that it differs in the two principal planes: the E-plane pattern has a null, while H-plane pattern has a sharp cusp. The overall efficiency has a broad maximum of 55%. A suitable objective lens would have an f-number of 1.1 ($\alpha = 65°$). The curves for dielectric constant 12 are similar, except that spillover loss at large angles has decreased to 2% because the losses into the air are reduced. The taper efficiency is worse at small angles because the reflection loss is larger. The maximum overall efficiency is 50% and a suitable objective lens would be $f/1.9$.

Fig. 2.4 shows the optimum efficiency as a function of dielectric constant. The curve has a broad peak around $\epsilon_r = 4$, falling off at higher dielectric constants because of reflection loss at the substrate lens, and at low dielectric constants because of radiation into the air behind the substrate. The optimum angle α for dipoles is near 75° for dielectric constants of 1.2 and larger.

These efficiencies could be raised if suitable anti-reflection coatings were available. Fig. 2.5 shows the effect of neglecting reflection loss. The improvement is an approximately constant factor equal to the reflection loss at normal incidence without an anti-reflection coating. The maximum efficiency becomes 65% for a dielectric constant of 4 and 74% for 12.

The antenna performance may also be enhanced by placing a shorting plane behind the dipole. If the shorting plane is placed at a suitable distance, radiation previously lost to the backside of the antenna is reflected back and adds constructively to the electric field at the dipole. Fig. 2.6 shows the improvement obtained by placing a shorting plane a quarter wavelength from the dipole. For a system with dielectric constant 4 the efficiency increases by about 5%. The

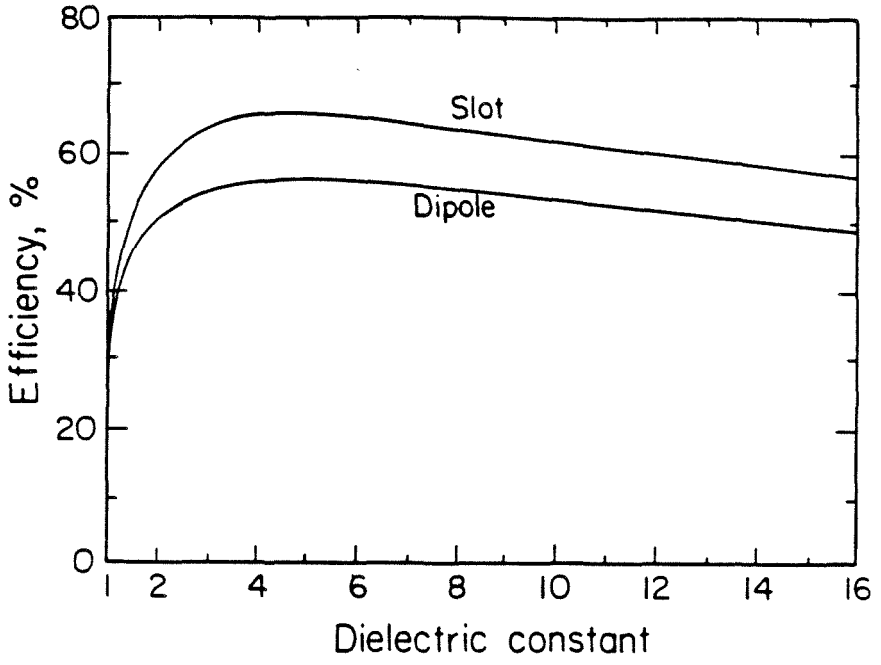

Fig. 2.4. Optimum efficiency of dipoles and slots with substrate lenses, plotted against dielectric constant.

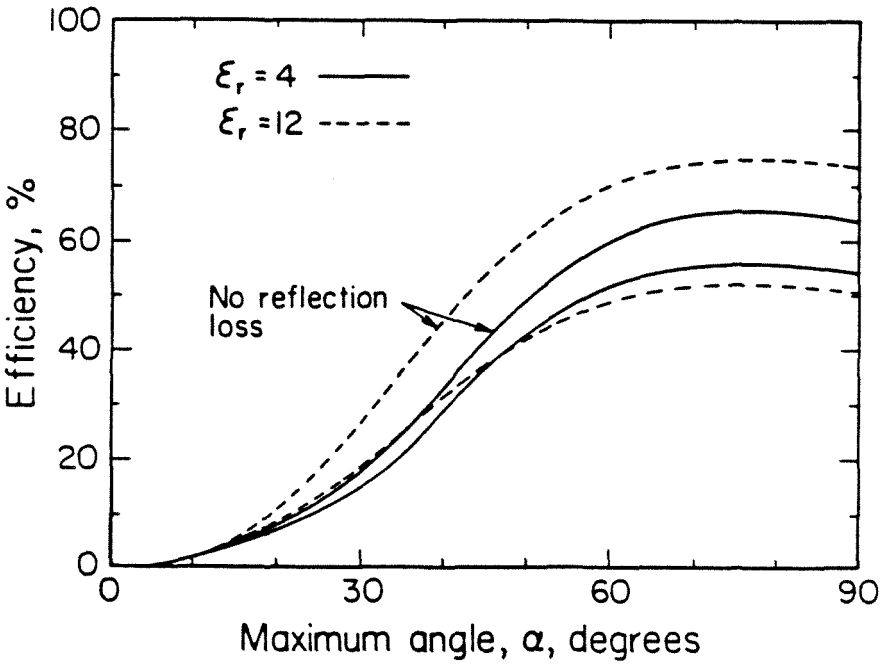

Fig. 2.5. Effect of an anti-reflection coating on the substrate lens for dipoles.

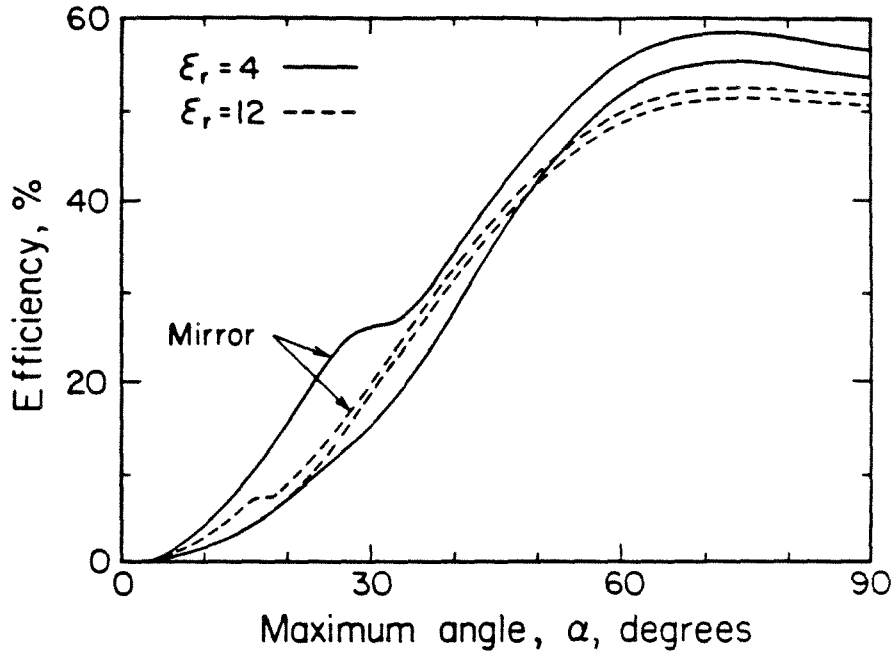

Fig. 2.6. Effect of a shorting plane a quarter of a free-space wavelength behind the substrate for dipoles with substrate lenses.

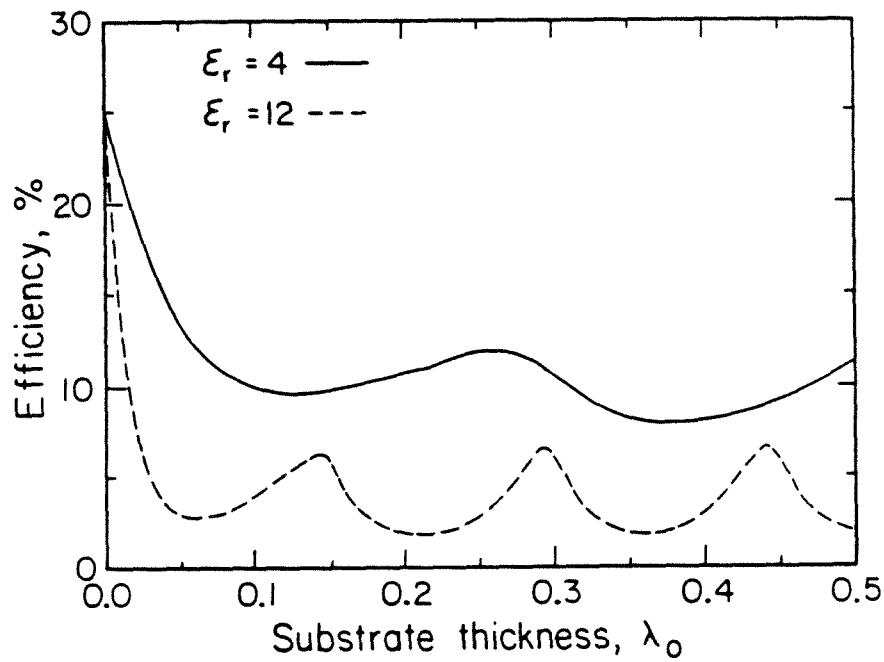

Fig. 2.7. Efficiency of dipoles on ungrounded substrates, plotted against the substrate thickness in free-space wavelengths for $\alpha = 60°$. The radiation comes through the substrate.

improvement for $\epsilon_r = 12$ is less because there is not as much backside radiation available for the mirror to reflect. The efficiency becomes much worse if the substrate lens is removed (Fig. 2.7). Now multiple reflections and substrate modes are present that depend on the substrate thickness. The substrate modes are responsible for the low efficiencies.

We now switch our attention from dipoles to slot antennas. Fig. 2.8 shows the efficiencies for slots on substrates with matching substrate lenses. For comparison, the lower efficiency of a slot in free space is also shown. The broad maxima characteristic of the dipole systems (Fig. 2.3) are absent. Instead, the curves peak at $\alpha = 90°$, with efficiencies of 65% for $\epsilon_r = 4$, and 60% for 12. The corresponding objective lenses are $f/1$ and $f/1.7$. These efficiencies are higher than for the dipoles, and the f-numbers are slightly smaller. A plot of peak efficiency against ϵ_r (Fig. 2.4) shows the same peak near $\epsilon_r = 4$ that dipoles had. For dielectric constants of 1.2 and larger, the optimum angle for α is 90°. If the substrate lens is removed, the efficiency drops dramatically because of losses to substrate modes (Fig. 2.9).

In the previous systems discussed the substrate lens was assumed to be matched so that it had the same dielectric constant as the substrate. In practice, quartz lenses are less expensive than silicon lenses, but it is desirable to fabricate monolithic integrated-circuit antennas and diodes on a semiconductor substrate. In Fig. 2.10 we consider a slot and a dipole on a semiconductor substrate with $\epsilon_r = 12$ and a quartz substrate lens ($\epsilon_r = 4$). The slot efficiencies are poor, except on very thin substrates, but for the dipole there is a thickness, 0.03 λ_0, with a high efficiency (63%) at $\alpha = 75°$ ($f/1$ primary). The reason the dipole is more efficient is that the lens and substrate form an asymmetric waveguide with all modes cutoff at this thickness, so that no power is lost to substrate modes.

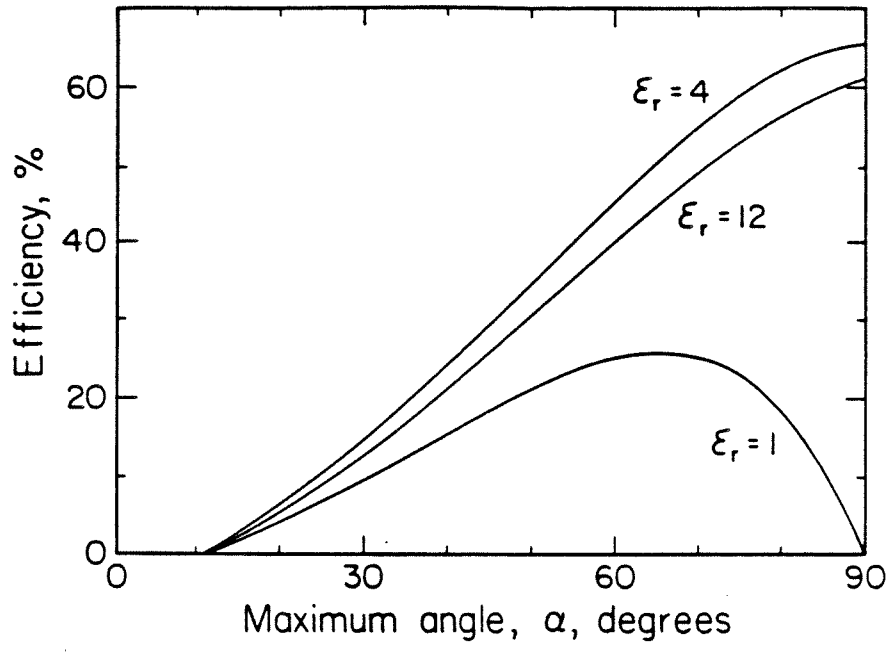

Fig. 2.8. Efficiency of slots with substrate lenses plotted against α.

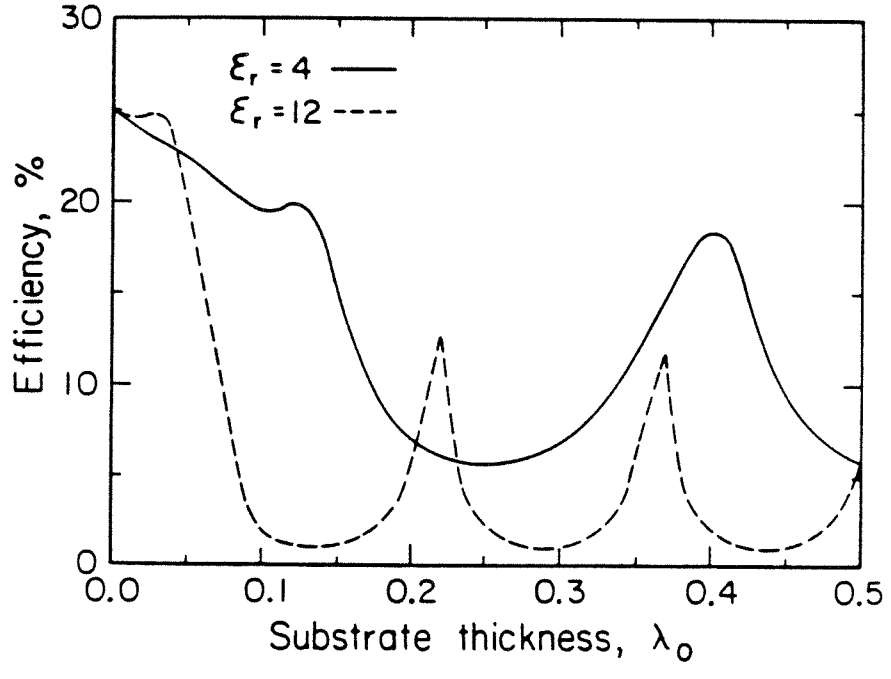

Fig. 2.9. Efficiency of slots on ungrounded substrates, plotted against substrate thickness for $\alpha = 60°$. The radiation comes through the substrate.

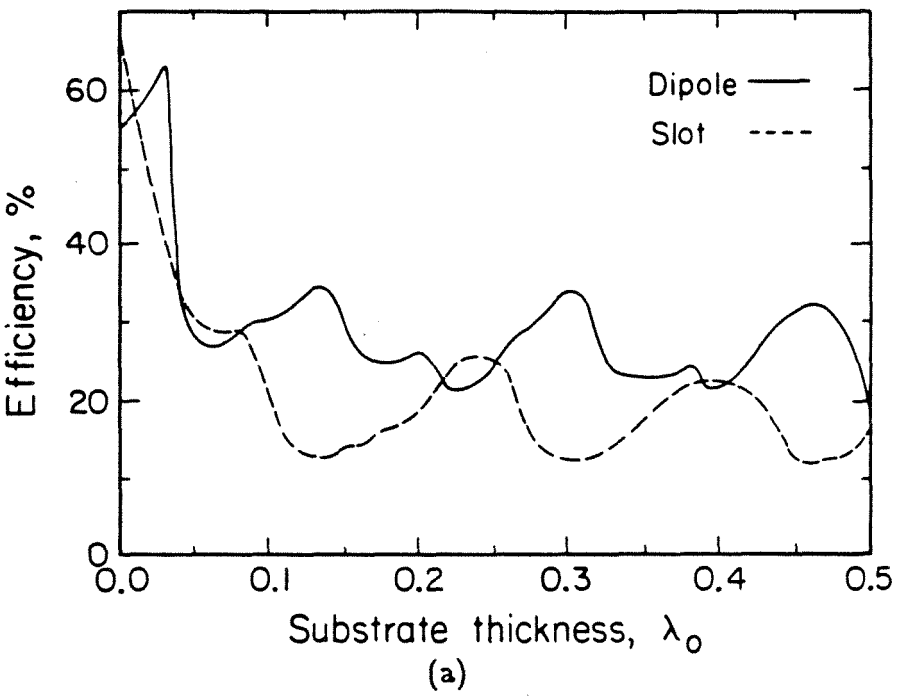

(a)

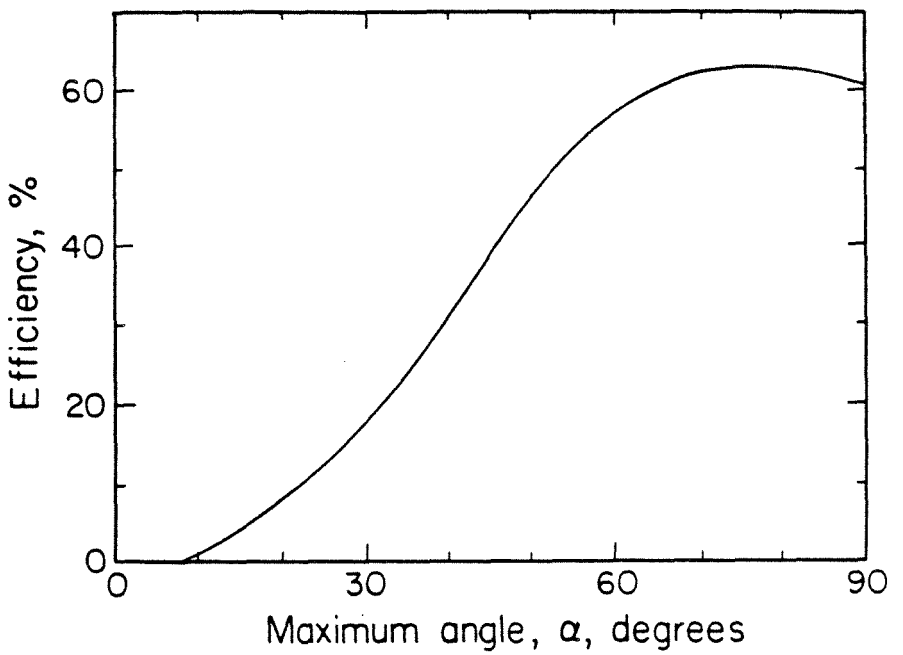

(b)

Fig. 2.10. (a) Optimum efficiency for dipoles and slots with substrate dielectric constant 12 and lens dielectric constant 4, plotted against substrate thickness in free-space wavelengths. (b) Dipole efficiency for a substrate thickness of 0.03 λ_0 plotted against α.

On the other hand, for the slot there is a ground plane on the substrate, and in this waveguide configuration there is a propagating TM mode at any thickness that will absorb power.

The final antenna considered is the microstrip antenna. Fig. 2.11 shows how the efficiency depends on substrate thickness. The peaks are close to odd-integral multiples of $\lambda_d/4$. Efficiencies above 40% are possible for this substrates at $\alpha = 60°$. Because there is no substrate lens, however, this angle requires $f/0.6$ primary optics. Making the substrate thin will also reduce the antenna impedance because of the ground plane on the back of the substrate. For $f/1$ optics ($\alpha = 30°$) the efficiency is limited to about 20%.

2.4. Conclusions

In comparing these antennas, it is important to keep practical considerations in mind. Absorption losses, particularly in substrate lenses, may be important, as well as problems in making a low f-number system with a wide field of view in imaging systems, and problems with making devices on very thin wafers. Calculations with different primary optics such as elliptical lenses and parabolic reflectors would give somewhat different results [16]. It should also be possible to improve any of these antennas by making a phased array. However, the results do show that the antennas with substrate lenses are potentially better feeds than those without substrate lenses. The substrate-lens coupled antennas are further improved by anti-reflection coatings.

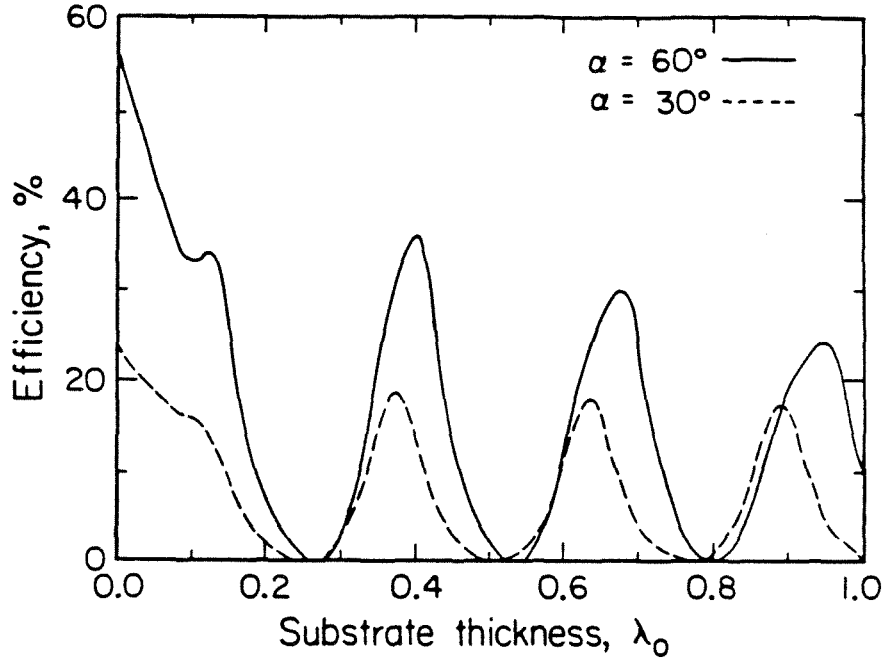

(a)

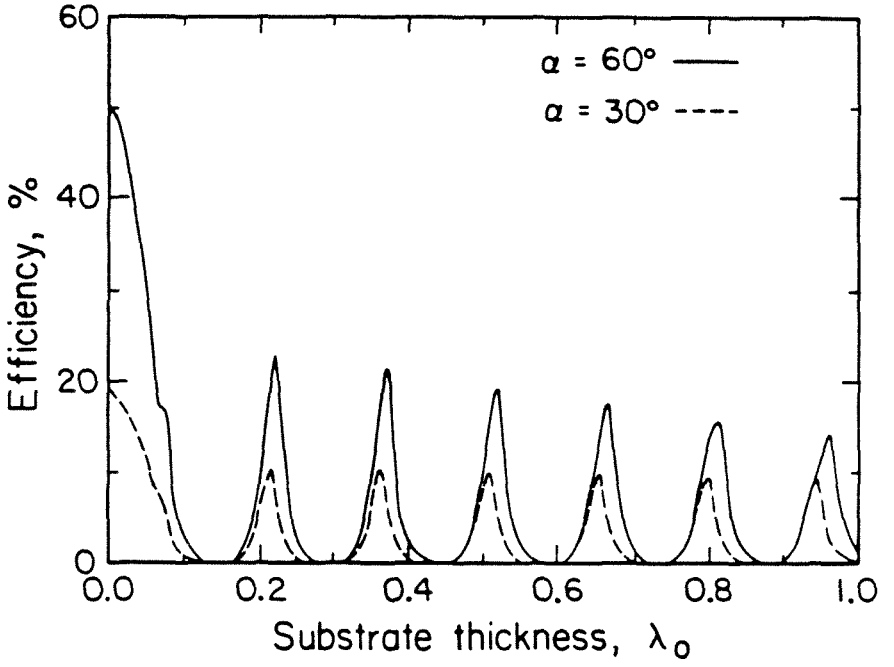

(b)

Fig. 2.11. Efficiency of microstrip dipoles with substrate dielectric constant 4 (a) and 12 (b), plotted against the substrate thickness.

References

[1] D. B. Rutledge, D. P. Neikirk and D. P. Kasilingam, "Integrated-Circuit Antennas," *Infrared and Millimeter-Waves Series*, vol. 10, pp. 1–90, K. J. Button, ed., Academic Press, New York, 1983.

[2] K. S. Yngvesson et al., "Planar Millimeter Wave Antennas with Application to Monolithic Receivers," *Proc. SPIE*, vol. 337, (Millimeter Wave Technology), 1982.

[3] T. L Hwang, D. B. Rutledge and S. E. Schwarz, "Planar Sandwich Antennas for Submillimeter Applications," *Appl. Phys. Lett.*, vol. 34, pp. 9–11, Jan. 1979.

[4] P. J. Gibson, "The Vivaldi Aerial," *9th Eur. Microwave Conf. Digest*, pp. 101–105, 1979.

[5] D. B. Rutledge and et al., "Antennas and Waveguides for Far-Infrared Integrated Circuits," *IEEE J. Quantum Electron.*, vol. QE–16, pp. 508–516, May 1980.

[6] C. Yao, S. E. Schwarz and B. J. Blumenstock, "Monolithic Integration of a Dielectric Millimeter-Wave Antenna and Mixer Diode: An Embryonic Millimeter-Wave IC," *IEEE Trans. Microwave Theory Tech.*, vol. MTT–30, pp. 1241–1247, Aug. 1982.

[7] B. J. Clifton, R. A. Murphy and G. D. Alley, "Integrated Monolithic Mixers on GaAs for Millimeter and Submillimeter Wave Applications," *Conf. Dig., 4th Int. Conf. on Infrared and Millimeter Wave and Their Applications*, IEEE Cat. No. 79CH1384–7, MTT, pp. 84–86, 1979.

[8] B. J. Clifton et al., "High-Performance Quasi-Optical GaAs Monolithic Mixer at 110 GHz," *IEEE Trans. Electron Dev.*, vol. ED–28, pp. 155–157, Feb. 1981.

[9] A. R. Kerr, P. H. Siegel and R. J. Mattauch, "A Simple Quasi-Optical Mixer for 100–120 GHz," *IEEE MTT-S Int. Microwave Symp. Dig.*, pp. 96–98, 1977.

[10] L. Yuan, J. Paul and P. Yen, "140 GHz Quasi-Optical Planar Mixers," *IEEE MTT-S Int. Microwave Symp. Dig.*, pp. 374–375, 1982.

[11] P. T. Parrish and et al., "Printed Dipole Schottky Diode Millimeter Wave Antenna Array," *SPIE Proc.*, vol. 337–30, 1982.

[12] D. P. Neikirk et al., "Far Infrared Imaging Antenna Arrays," *Appl. Phys. Lett.*, vol. 40, pp. 203–205, Feb. 1982.

[13] K. D. Stephan, N. Camilleri and T. Itoh, "A Quasi-Optical Polarization-Duplexed Balanced Mixer for Millimeter-Wave Applications," *IEEE Trans. Microwave Theory Tech.*, vol. MTT–31, pp. 169–170, Feb. 1983.

[14] N. G. Alexopoulos, P. B. Katehi and D. B. Rutledge, "Substrate Optimization for Integrated Circuit Antennas," *IEEE Trans. Microwave Theory Tech.*, vol. MTT–31, pp. 550–557, July 1983.

[15] D. M. Pozar, "Considerations for Millimeter Wave Printed Antennas," *IEEE Trans. Antenna Propagat.*, vol. AP–31, pp. 740–747, Sept. 1983.

[16] K. S. Yngvesson, "Near Millimeter Imaging with Integrated Planar Receptors: I. General Requirements and Constraints," *Infrared and Millimeter Waves*, vol. 10, K. J. Button, ed., Academic Press, New York, 1983.

[17] D. B. Rutledge and M. S. Muha, "Imaging Antenna Arrays," *IEEE Trans. Antennas Propagat.*, vol. AP–30, pp. 535–540, July 1982.

[18] J. W. Goodman, *Introduction to Fourier Optics*, McGraw-Hill, New York, pp. 48–54, 1968.

[19] S. Ramo, J. R. Whinnery and T. van Duzer, *Fields and Waves in Communi-*

cation Electronics, Chap. 6, John Wiley & Sons, New York, 1965.

[20] M. Born and E. Wolf, *Principles of Optics*, 6th ed. Pergamon Press, Oxford, pp. 168, 1980.

[21] R. S. Elliott, *Antenna Theory and Design*, Chap. 1, sec. E, Prentice-Hall, Inc., Englewood Cliffs, N.J., 1981.

[22] N. G. Alexopoulos and D. Jackson, "Enhancement of Printed-Circuit Antenna Gain for Millimeter-Wave Applications," *7th Int. Conf. on Infrared and Millimeter Waves*, pp. 278, Marseilles, France, April 1983.

[23] K. G. Stephan and Tatsuo Itoh, "A Planar Quasi-Optical Subharmonically Pumped Mixer Characterized by Isotropic Conversion Loss," *IEEE Trans. Microwave Theory and Tech.*, vol. MTT-32, pp. 97–102, 1984.

[24] E. L. Kollberg et al., "New Results on Tapered Slot Endfire Antennas on Dielectric Substrates," *8th Int. Conf. Infrared and Millimeter Waves*, pp. F3.6–3.7, Miami, Florida, Dec. 1983.

Chapter 3

A Polystyrene Cap for Matching a Silicon Lens at Millimeter Wavelengths

The lens-coupled antennas shown in Fig. 3.1 have been widely used in monolithic circuits [1,2,3]. The idea is that energy is focused onto an antenna through a lens placed on the back of the substrate. This eliminates losses to substrate modes and takes advantage of the fact that antennas on a substrate are more sensitive to radiation from the substrate side [4]. For a gallium-arsenide substrate, it is convenient to use a silicon lens, since the indices of refraction are well matched ($n_{Si} = 3.42$ and $n_{GaAs} = 3.59$ at 94 GHz [5]). Unfortunately the reflection loss of the silicon lens is quite high, 1.55 dB at normal incidence, and it is necessary to reduce this loss.

Several different matching techniques have been demonstrated at other wavelengths. In optics, lenses may be coated with quarter-wave layers by vacuum deposition. In microwaves, these matching layers may be simulated by machining grooves or drilling holes [6], or with reactive grids [7]. In the far infrared, polyethylene sheets have been thermally bonded to quartz, silicon, and sapphire filters [8]. For millimeter wavelengths, a thin plastic cap made by thermal molding turns out to be a simple way to reduce the reflection loss of a silicon lens. A polystyrene cap has been fabricated and put on our silicon substrate lens. The cap is 0.5 mm thick, and it reduces the reflection loss at 94 GHz by 1.5 dB. The theory and the measured results will be described.

3.1. Theory

Fig. 3.2 shows the calculated reflection losses at 94 GHz for silicon lenses with polystyrene and polyethylene caps of varying thickness. The refractive index for

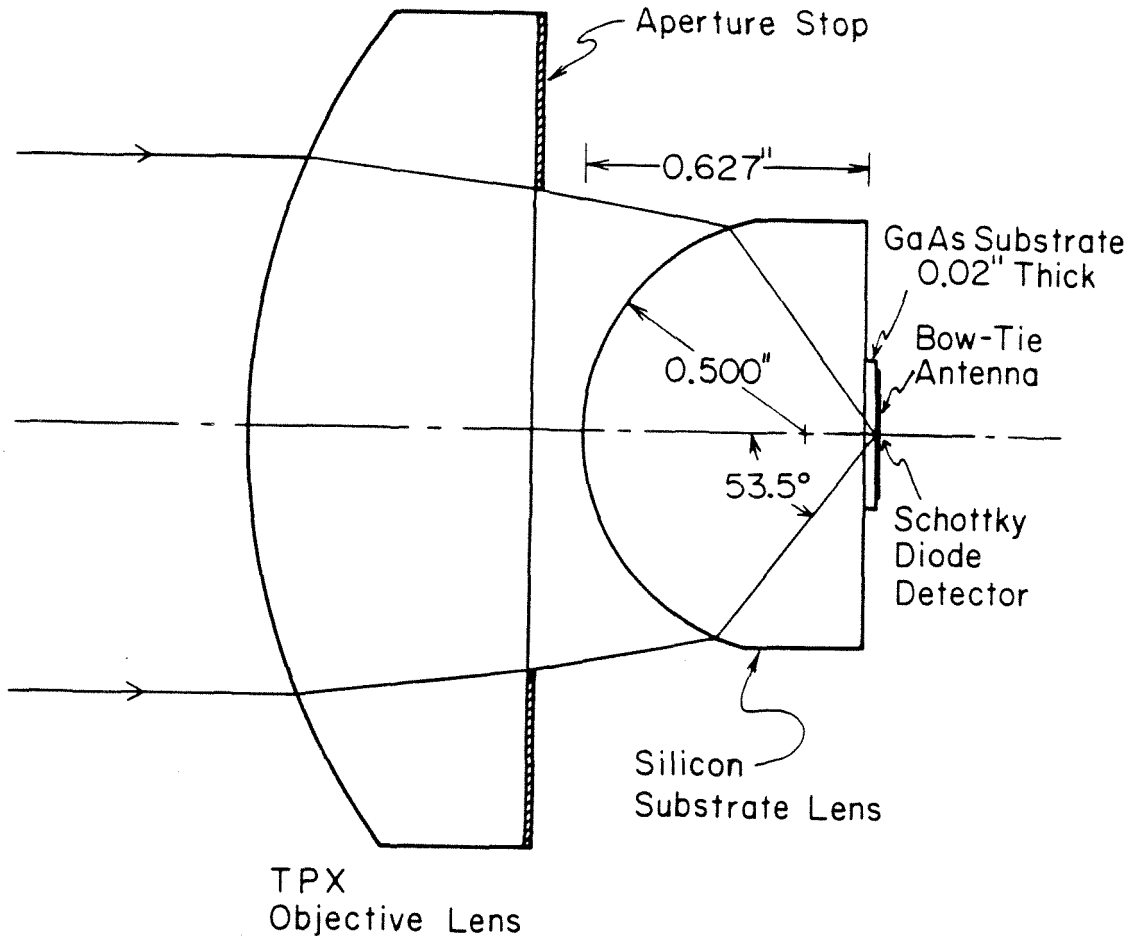

Fig. 3.1. Lens-coupled antenna used in the measurements.

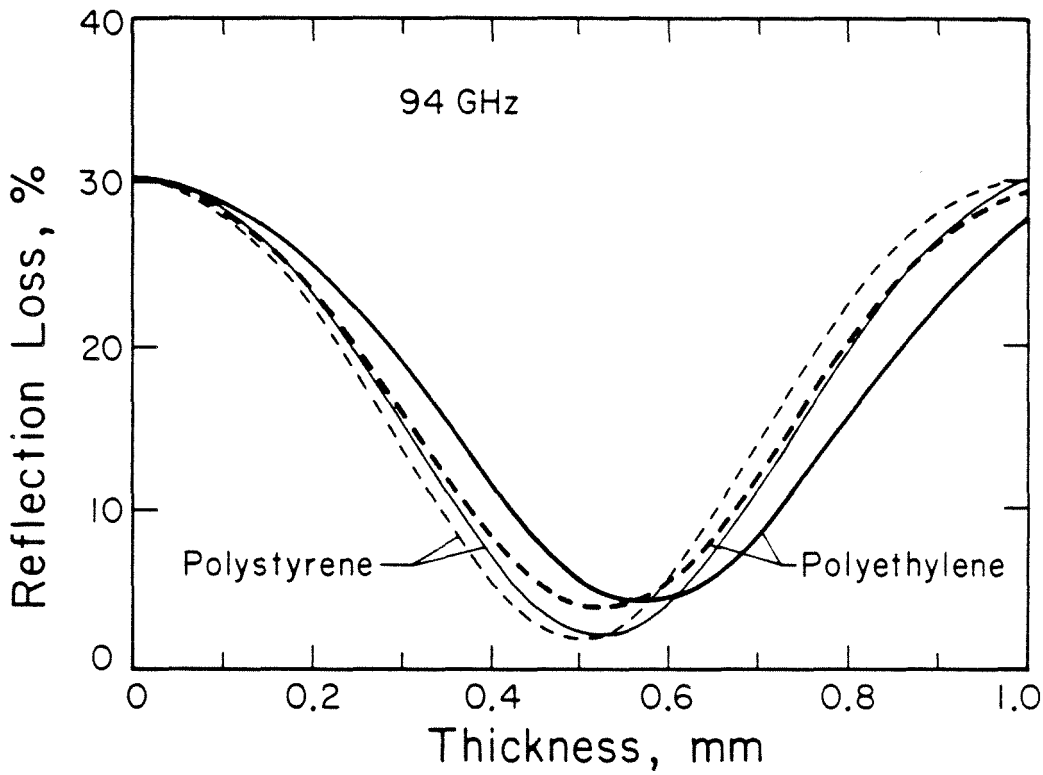

Fig. 3.2. The calculated reflection loss at 94 GHz for a silicon substrate lens vs. the thickness of plastic matching cap. The dashed lines show the normal incidence loss. For the solid lines the different angles of incidence across the lens are considered.

polystyrene is 1.60 and the refractive index of polyethylene is 1.52 [5]. The dashed lines show the normal incidence losses. The solid lines are from more detailed calculations that take the different angles of incidence and polarization across the lens into account. This loss is found by integrating the angular power spectrum, weighted by the transmittance at each angle [9]. It is assumed that the thickness of the matching layer is uniform. The $f/\#$ of the objective lens is taken to be 2.1, corresponding to a maximum angle of incidence within the silicon lens of 53.5° (see Fig. 3.1). Aberrations in the objective lens are neglected. In practice the antenna pattern will also affect the results, but this effect is not included.

The minimum losses predicted by the two calculations are quite close. At normal incidence the minimum is at a thickness of a quarter wavelength. The more detailed calculations show that the layer should be somewhat thicker, depending on the $f/\#$ and the index of the refraction. This is to be expected, because the matching layers for oblique angles of incidence must be thicker than those for normal incidence. However, the thickness of the plastic layer is not critical. For polystyrene, the loss is less than 5% for thickness from 0.42 mm to 0.62 mm.

It is perhaps surprising that the reflection losses for normal incidence are so close to the more precise values that consider the different angles of incidence across the lens. From Fig. 3.1, we can see that the angle of incidence can be quite large. When we look at the calculations in detail, it is clear that this is a polarization effect. Half of the power is incident on the substrate lens with TE polarization, and the transmission worsens as the angle of incidence increases. The other half is TM polarized, but this transmission improves as the angle of incidence approaches the Brewster angle. The two effects nearly cancel, so that

the normal incidence calculation is quite accurate.

3.2. Experiment

Polystyrene was chosen because of its low loss and ease of machining and molding. A flat polystyrene sheet with 0.5 mm thickness was deformed by a heat gun into the mold that was originally used to grind the silicon lens. At the same time the silicon lens is used to press the cap to make it smooth. Several tries were needed to get a uniform thickness. Fig. 3.3 shows the polystyrene cap which was glued to the lens by applying Shipley photoresist to the edge of the cap. Photoresist is a convenient glue because it dissolves easily in acetone.

We measured the improvement by comparing video responsivities with and without the cap. The detector was a monolithic gallium-arsenide Schottky diode integrated with a bow-tie antenna. Fig. 3.4 shows the measured improvement from 75 GHz to 170 GHz. For comparison, the dashes show the improvement expected if there were no reflection loss at all, and the solid line shows the improvement predicted by the same calculations that were used for Fig. 3.2 that considered the different angles of incidence. The dots are the experimental values. Uncertainties in power-meter calibration factors and system losses contribute to the scatter in the points. The matching layer gives 1.5 dB improvement at the design frequency of 94 GHz, and very little improvement at 170 GHz, where the cap acts as a half-wave window.

3.3. Conclusion

The measurements against frequency show that the cap behaves according to theory. This makes a silicon substrate lens for a gallium-arsenide monolithic cir-

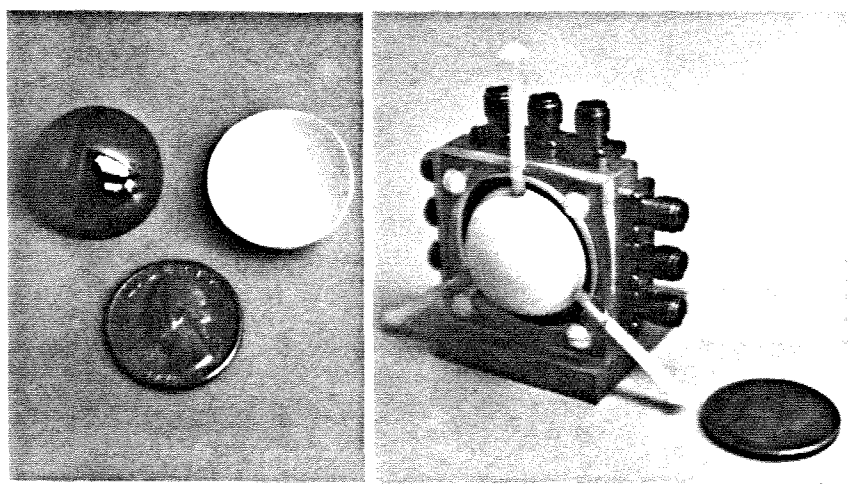

Fig. 3.3. (a) Silicon substrate lens (right) and polystyrene cap (left), and (b) assembled.

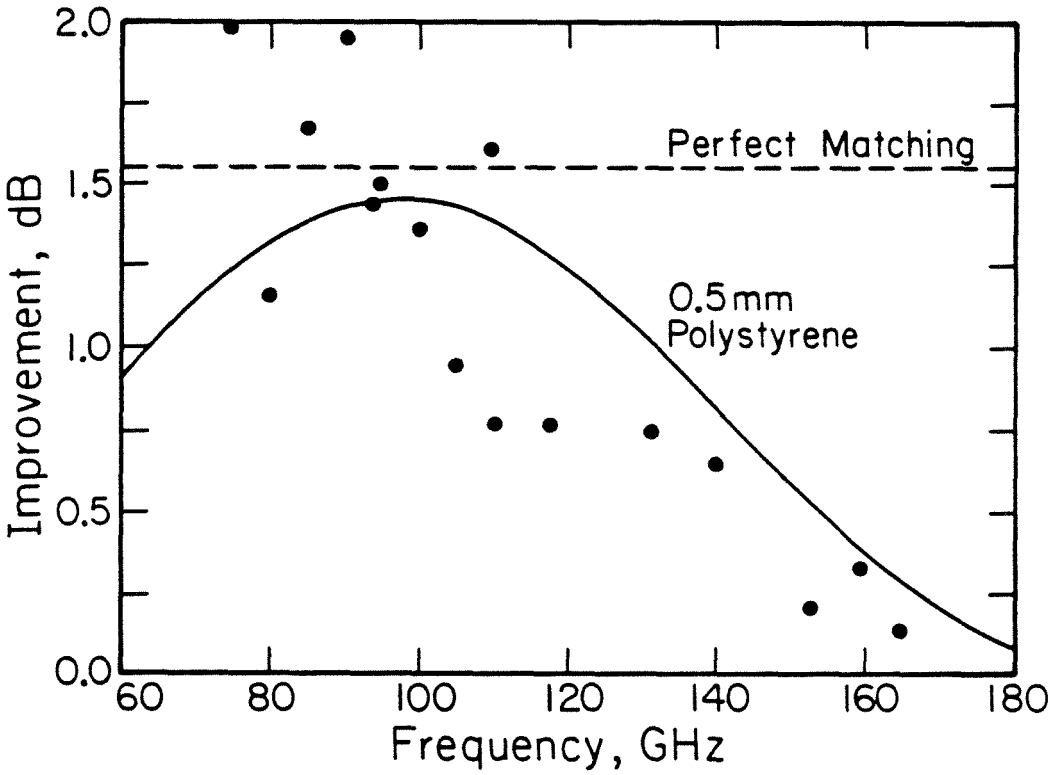

Fig. 3.4. The measured improvement of reflection loss for a silicon substrate lens with a 0.5 mm polystyrene cap at different frequencies. The theory is calculated as in Fig. 3.2, considering the different angles of incidence. Uncertainties in power-meter calibration factors and system losses contribute to the scatter in the points

cuit much more attractive than before. For the absorption loss of high-resistivity silicon reported in the literature, 0.6 dB/cm [5], the total reflection and absorption loss of a 1 inch diameter silicon lens with the cap should be 1.1 dB.

References

[1] D. P. Neikirk et al., "Far-Infrared Imaging Antenna Arrays," *Appl. Phys. Lett.*, 40, pp. 203–205, 1982.

[2] C. Zah et al., "Progress in Monolithic Schottky Diode Imaging Arrays," *9th Int. Conf. on Infrared and Millimeter Waves*, Osaka, Japan, W–4–2, Oct. 1984.

[3] M. J. Wengler et al., "A Low Noise Receiver for Millimeter and Submillimeter Wavelength," to be published, *Int. J. of Infrared and Millimeter Waves.*

[4] D. B. Rutledge, D. P. Neikirk and D. P. Kasilingam, "Integrated-Circuit Antennas," *Infrared and Millimeter Waves*, vol. 10, Chap. 1, pp. 1–90, K. J. Button, ed., Academic Press, New York, 1983.

[5] M. N. Afsar and K. J. Button, "Millimeter-Wave Dielectric Properties of Materials," *Infrared and Millimeter Waves*, vol. 12, Chap. 1, pp. 1–42, K. J. Button, ed., Academic Press, New York, 1984.

[6] T. Morita and S. B. Cohn, "Microwave Lens Matching by Simulated Quarter-Wave Transformers," *IRE Trans.*, AP–4, pp. 33–39, 1956.

[7] E. M. T. Jones and S. B. Cohn, "Surface Matching of Dielectric Lenses," *J. Appl. Phys.*, 26, pp. 452–457, 1955.

[8] K. R. Armstrong and F. J. Low, "Far-Infrared Filters Utilizing Small Particle Scattering and Antireflection Coatings," *Appl. Opt.*, 13, pp. 425–430, 1974.

[9] C. Zah, R. C. Compton and D. B. Rutledge, "Efficiencies of Elementary Integrated-Circuit Feed Antennas," *Electromagnetics*, vol. 3, pp. 239–254, 1984.

Chapter 4

Fabrication and Packaging

A fabrication process has been developed to make our imaging array on semi-insulating GaAs substrates. Planar Schottky diodes and bow-tie antennas are integrated together on one chip. A self-aligning process and proton isolation have been developed to make these planar Schottky diodes with a 1.1-THz zero-bias cutoff frequency. A special package has been made to hold the chip and the substrate lens. The important features of fabrication and packaging will be described [1]. The detailed fabrication process is given in Appendix A. The measured DC parameters of the Schottky diodes will be compared with the theoretical values.

4.1. Design of the Planar Schottky Diode

The critical element of our monolithic imaging array is the planar Schottky diode. Fig. 4.1 shows SEM photographs of the diode. Its area is about 5 μm^2. The way to make a Schottky diode that works at millimeter frequencies is to make it small to reduce the shunting effect of the junction capacitance. There is a trade-off between the series resistance and the junction capacitance [2]. In order to reduce the series resistance as well as the junction capacitance, the Schottky electrode is designed to be a narrow stripe, which gives a high periphery-to-area ratio as shown in Fig. 4.2a. For a given junction capacitance which is roughly proportional to the diode area, the series resistance can be reduced by maximizing the periphery-to-area ratio. The width of the Schottky electrode is defined to be 0.8 μm by a self-aligning process (see Fig. 4.1 and 4.2c). The length of the Schottky diode is defined to be 6 μm by the proton bombardment (see Fig. 4.1 and 4.2b). These processes will be described in the following sections.

The diodes were made on top of a semi-insulating GaAs substrate. The

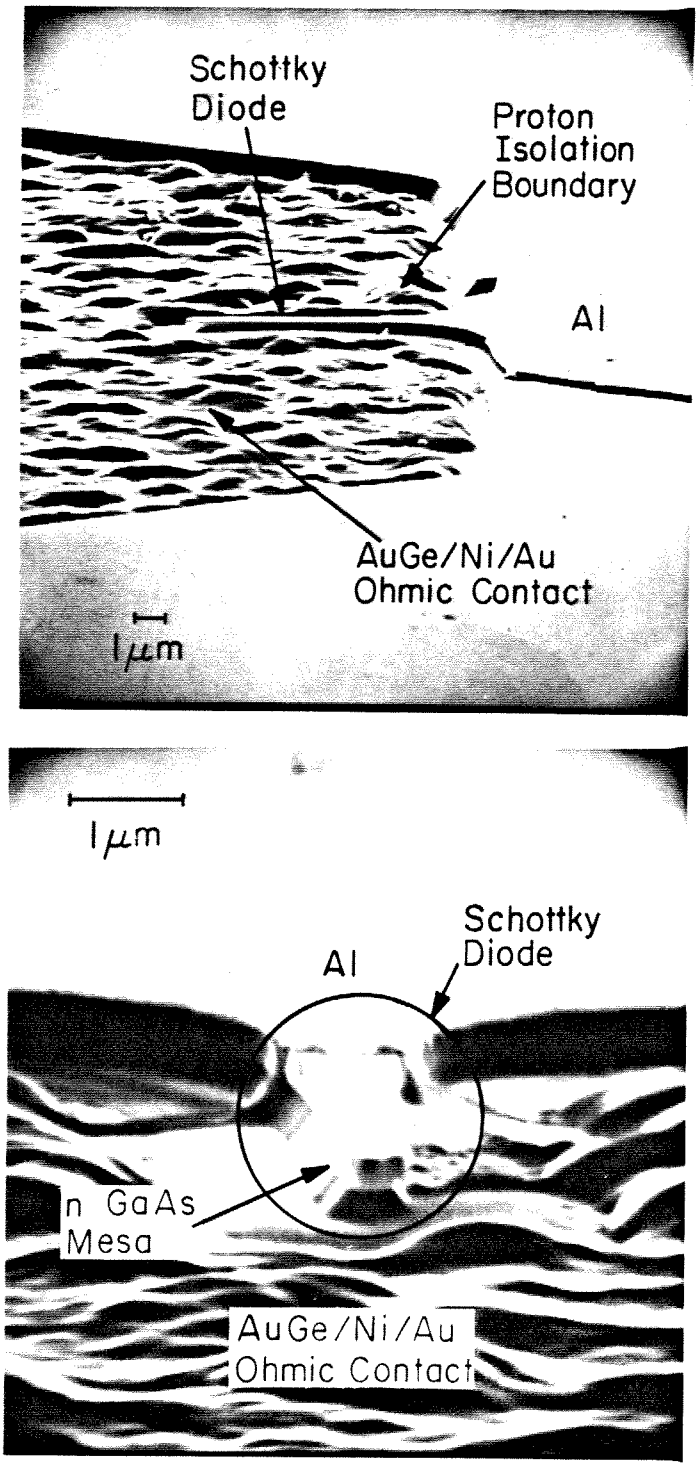

Fig. 4.1. SEM photographs of a planar Schottky diode. Side view (top) and head-on view (bottom).

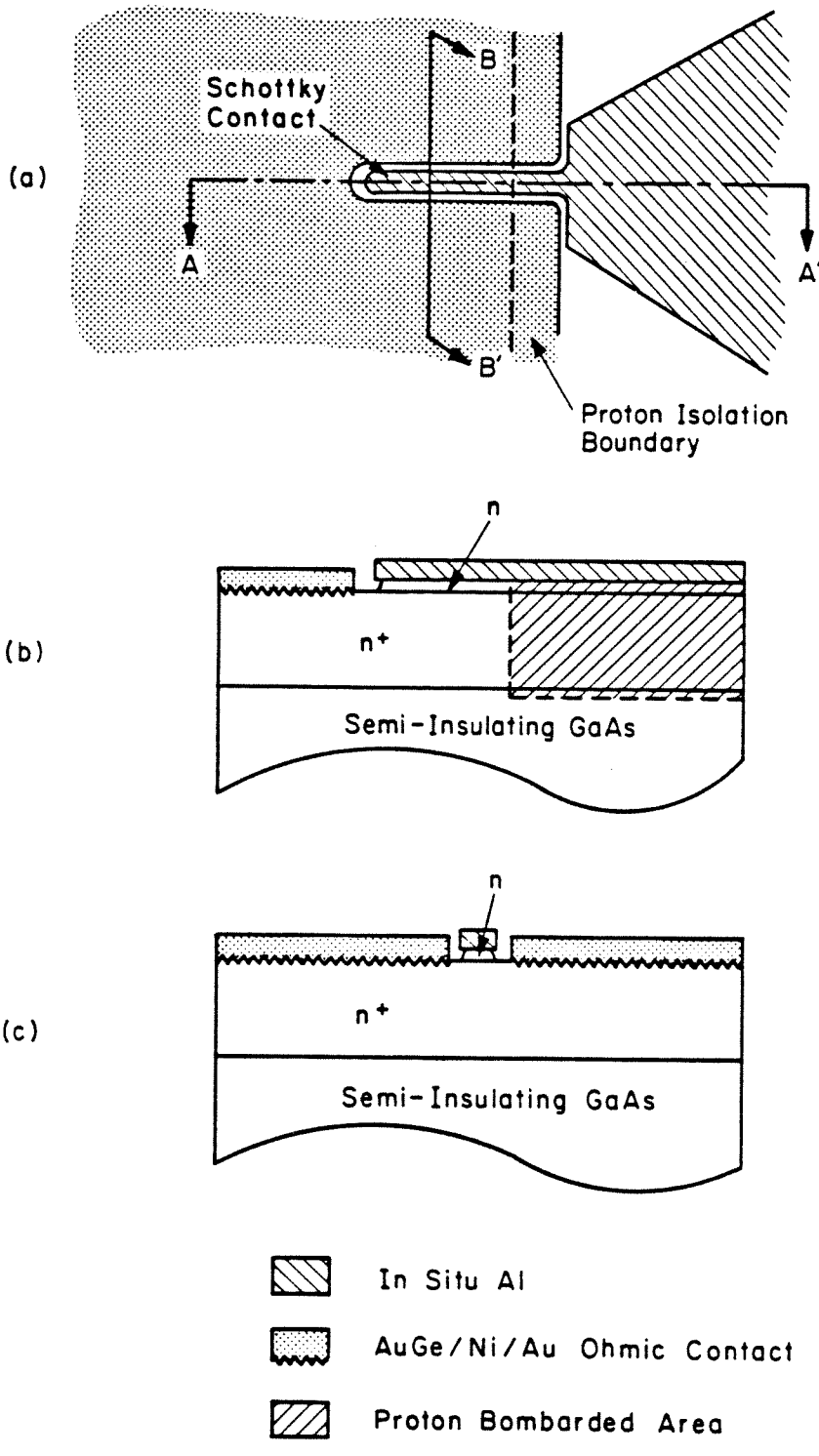

Fig. 4.2. Schematic drawing of our planar Schottky diode. (a) top view, (b) A-A' section view, and (c) B-B' section view.

gallium arsenide was chosen rather than other semiconductors because of its high mobility, easy isolation, and good Schottky contact. At 100 GHz the absorption loss for a Cr-doped gallium arsenide substrate 20 mils thick is negligible (0.013 dB calculated from data in [4]). Fig. 4.3 gives the cross section of the epitaxial layers. All the epitaxial layers and the aluminum were grown in situ by molecular beam epitaxy (MBE). The bottom n^+ layer is approximately 1.4 μm thick with a doping concentration of 3×10^{18} cm^{-3}. Its thickness is chosen so that it can be completely converted into a semi-insulating layer by proton bombardment with an energy of 300 KeV. The n layer is 0.1 μm thick with a doping concentration of 10^{17} cm^{-3}. It is designed to be depleted at zero bias to reduce the series resistance due to an undepleted n layer. The doping concentration of the n layer is chosen to achieve a relatively small tunnel current at room temperature and a small series resistance in the n layer. The top aluminum layer is 0.2 μm thick. Since it is grown at ultra-high vacuum, the Schottky contact between the aluminum and the GaAs substrate should be excellent.

4.2. Self-Aligning Process

In order to reduce the series resistance, a self-aligning process has been developed to make the Schottky electrode narrow and to reduce the gap between the electrode and the ohmic contact. The idea for this process comes from the closely spaced electrode (CSE) FET structure [5]. As shown in Fig. 4.4, one photoresist mask first protects the Schottky electrode during etching and then defines the ohmic contact by lift off after evaporating AuGe/Ni/Au. Therefore, the Schottky electrode and the ohmic contact are self-aligned. The distance between the ohmic contacts is the same as the width of the photoresist mask which is about 3 μm. The Schottky electrode is formed by side-etching from the photoresist

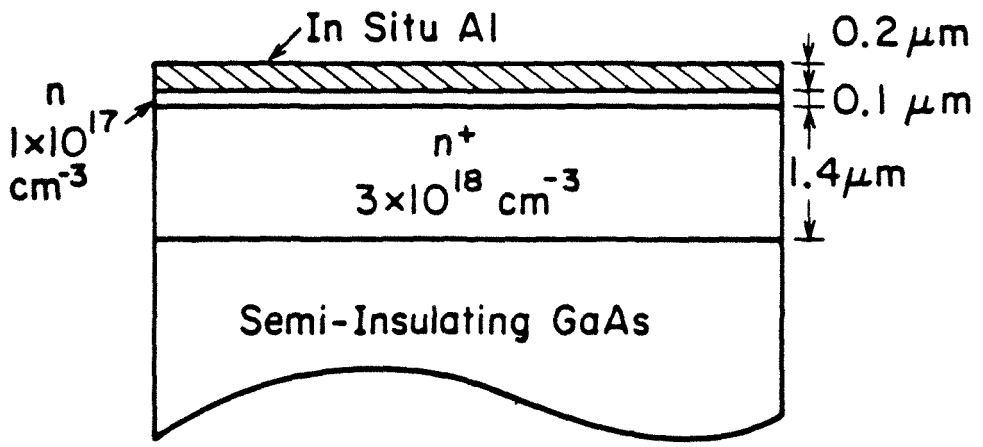

Fig. 4.3. Cross section of epitaxial layers.

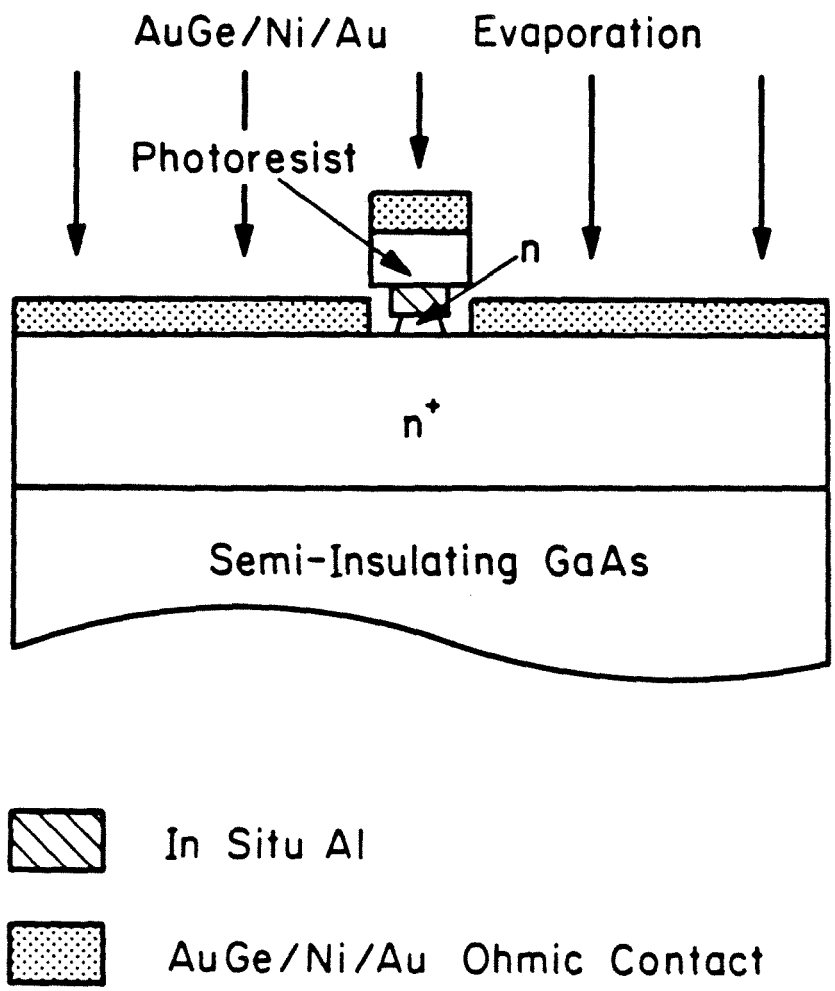

Fig. 4.4. Self-aligning process.

mask. With the proper undercut during etching, a submicron electrode 0.8 μm wide (see Fig. 4.1) has been achieved using optical contact lithography.

4.3. Ohmic Contact

After lifting off the photoresist, the ohmic contact is formed by alloying the evaporated AuGe/Ni/Au onto the n^+ layer at 430° for 30 sec. in an H_2 ambient. Gold germanium is a eutectic alloy (88% Au, 12% Ge by weight). The eutectic melts at 360°C. Germanium is an amphoteric dopant of GaAs and becomes an n type dopant only if it rests on the gallium sites of the crystal after alloying. Gold helps germanium move to the desired position by the diffusion of gallium into gold. Nickel enhances diffusion and prevents the metal from balling up. The rise and fall times of substrate heating should be as short as possible [6]. The linear transmission line model has been applied to determine the contact resistivity and the resistivity of the n^+ layer [7]. Our ohmic contact has a 5 $\mu\Omega$-cm^2 contact resistivity. The resistivity of the n^+ layer is 1.36×10^{-3} Ω-cm^2.

4.4. Proton Isolation

A proton bombardment procedure (shown in Fig. 4.5) was chosen to isolate the diode, since it avoids the step coverage problem in mesa etching and is easier than selective epitaxy [8,9]. The protons create damage centers when they penetrate into the GaAs substrate. These damage centers reduce the conductivity of the epi layers by trapping mobile electrons [10]. The required implantation energy and dose are determined experimentally. Two consecutive proton implantations (320 KeV with a 5×10^{14} cm^{-2} dose and 200 KeV with a 3×10^{14} cm^{-2} dose) completely isolate our diodes. A multiple-energy bombardment is supposed to be superior to a single-energy bombardment in creating high-resistivity layers

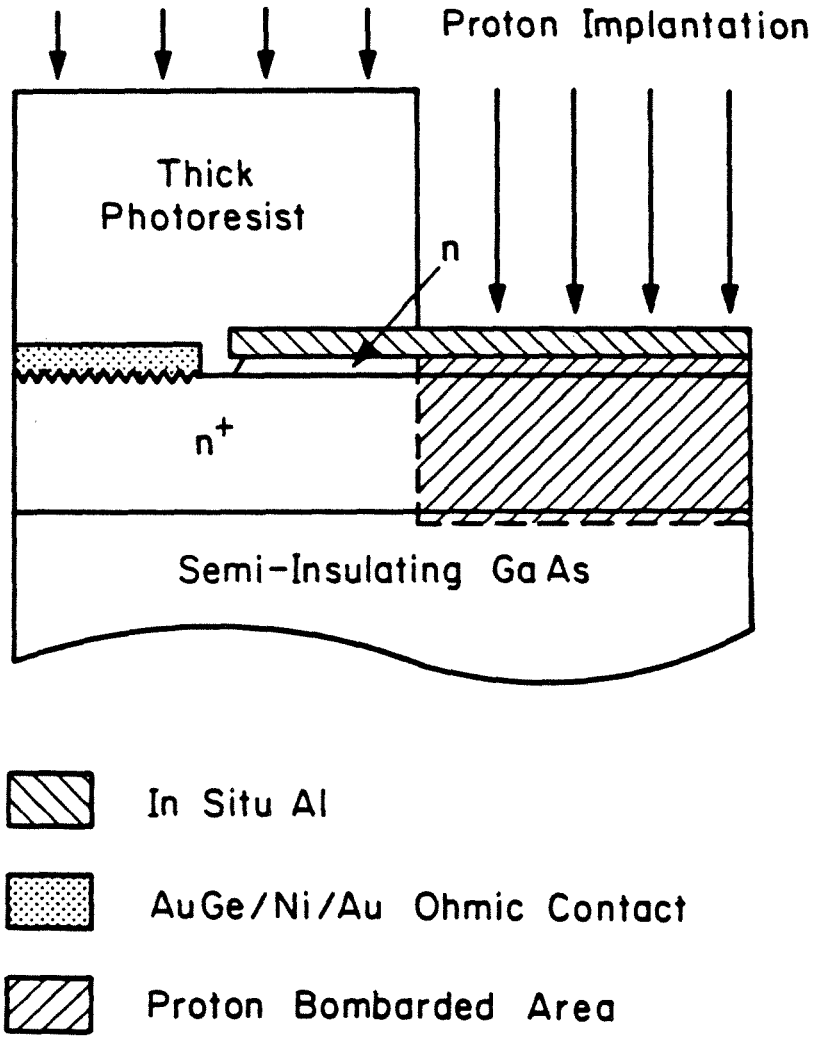

Fig. 4.5. Proton isolation process.

in n^+ GaAs [11]. The photoresist was chosen as a mask rather than gold to protect the active area because it is easier and cheaper. The photoresist should be thick enough to block the protons and it should have a well-defined boundary. Fig. 4.6 shows a SEM photograph of the thick photoresist. It looks like a cliff at the edge. From our experience, photoresist 3.5 μm thick blocks 320 KeV protons.

4.5. Packaging

Fig. 4.7 shows the imaging array with a planar Schottky diode at the apex of each bow-tie antenna. Each chip has nine bow-tie antennas and Schottky diodes. The spacing between the antennas is 0.75 mm. The bow-tie antenna was chosen because it is a broadband antenna and its extended low frequency leads automatically provide RF choking [12]. Fig. 4.8 shows a package designed to hold the chip and the substrate lens, as well to make the IF connections. Fig. 4.9 shows parts of the package. The package contains nine IF ports which are SMA connectors mounted on a copper block. The back piece has three screws that act as backshorts behind the wafer and three screws shorted to the front piece to provide a better IF ground. The low frequency leads of the array are connected to the SMA connectors through 50-Ω striplines made out of printed circuit board (RT/duroid 5870). The printed circuit was soldered on the copper block by low temperature solder (Indalloy No. 290(E), 97% In/ 3% Ag) bought from the Indium Corperation of America. The chip was glued to the package by Shipley photoresist. Photoresist is a convenient glue because it dissolves easily in acetone. The connections between low frequency leads of the array and striplines are made by 1 mil aluminum bond wires. The substrate lens is pressed against the chip by the nylon screws. The white polystyrene cap is put on the silicon lens to reduce the reflection loss at 94 GHz. One can get a feeling for how high the

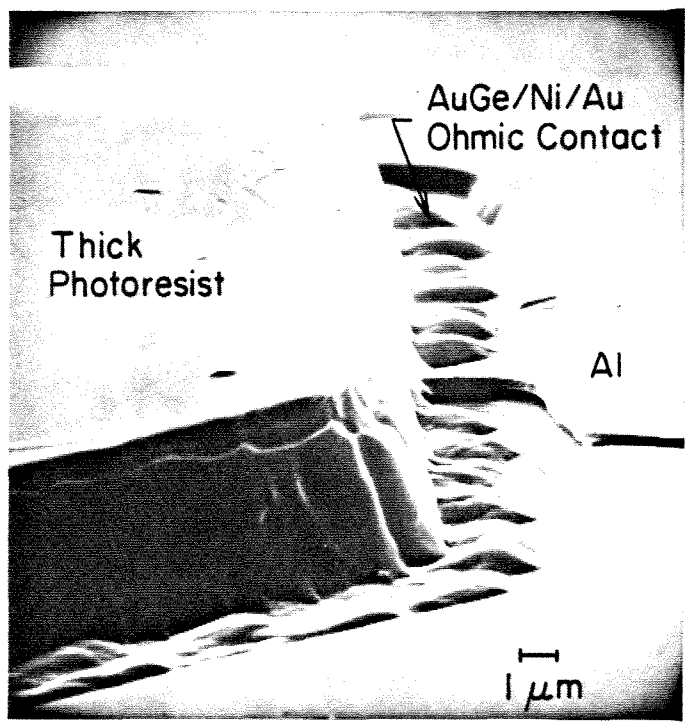

Fig. 4.6. SEM photograph of a thick photoresist used as proton isolation mask.

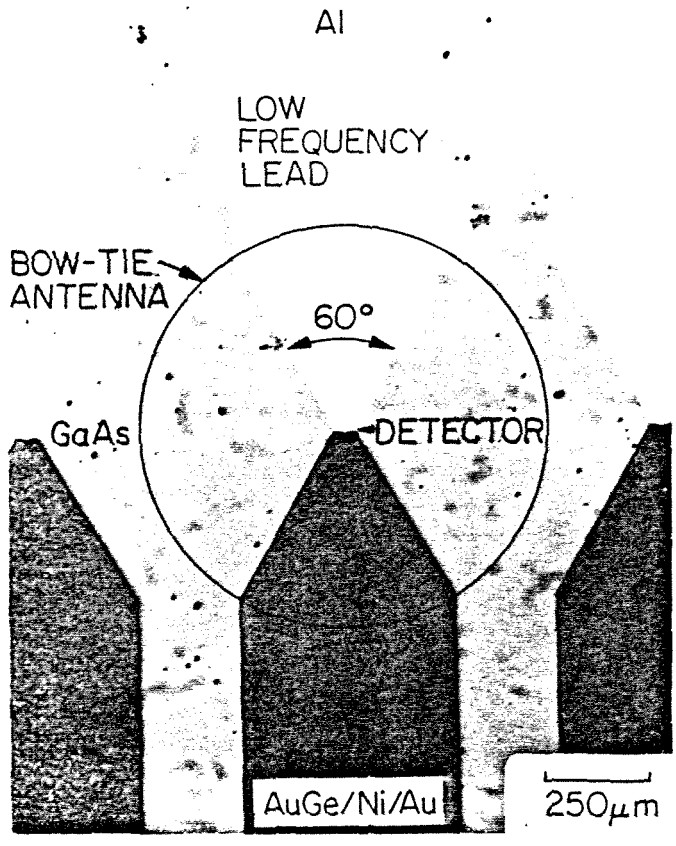

Fig. 4.7. Imaging array with a planar Schottky diode at the apex of each bow-tie antenna.

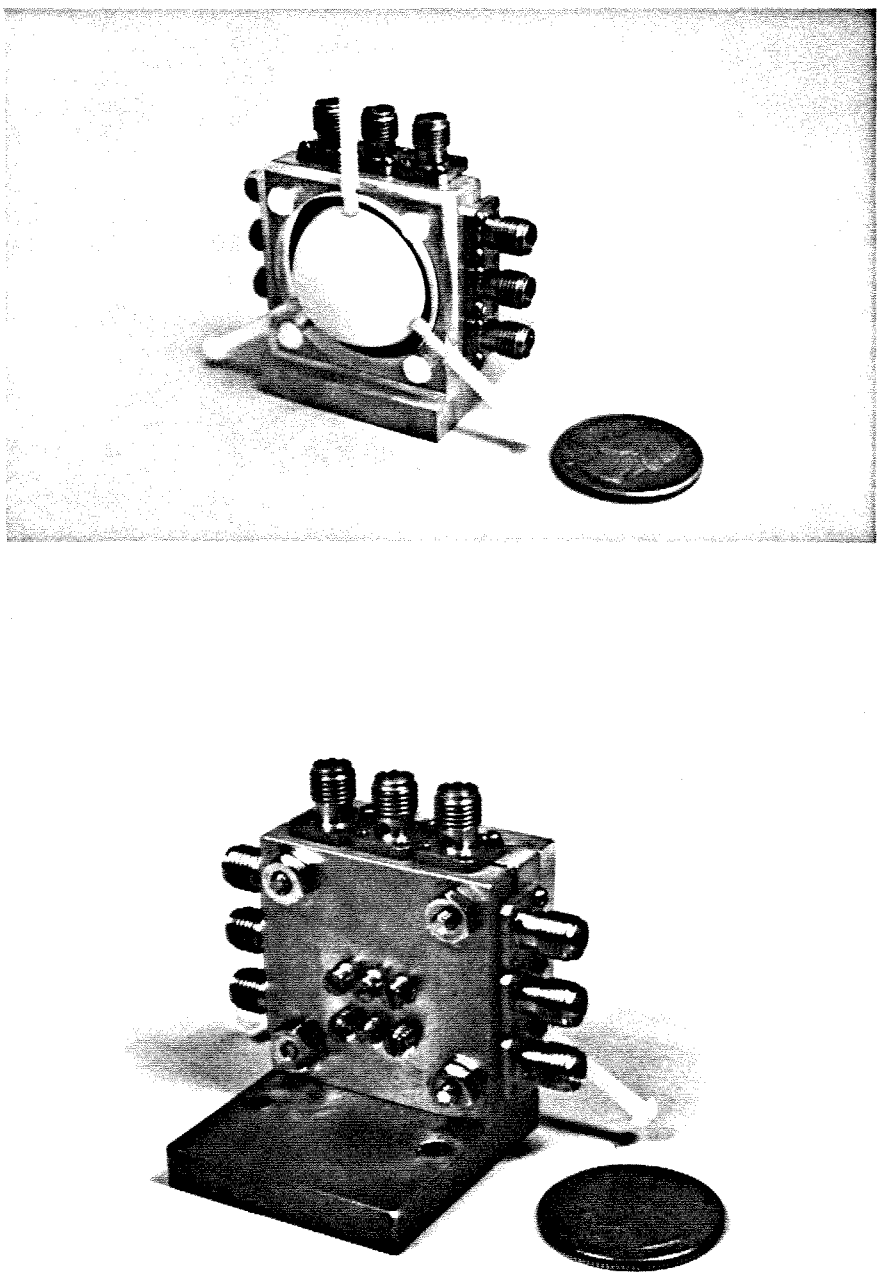

Fig. 4.8. Front view of the package in assemble form (top). Back-side view of the package (bottom).

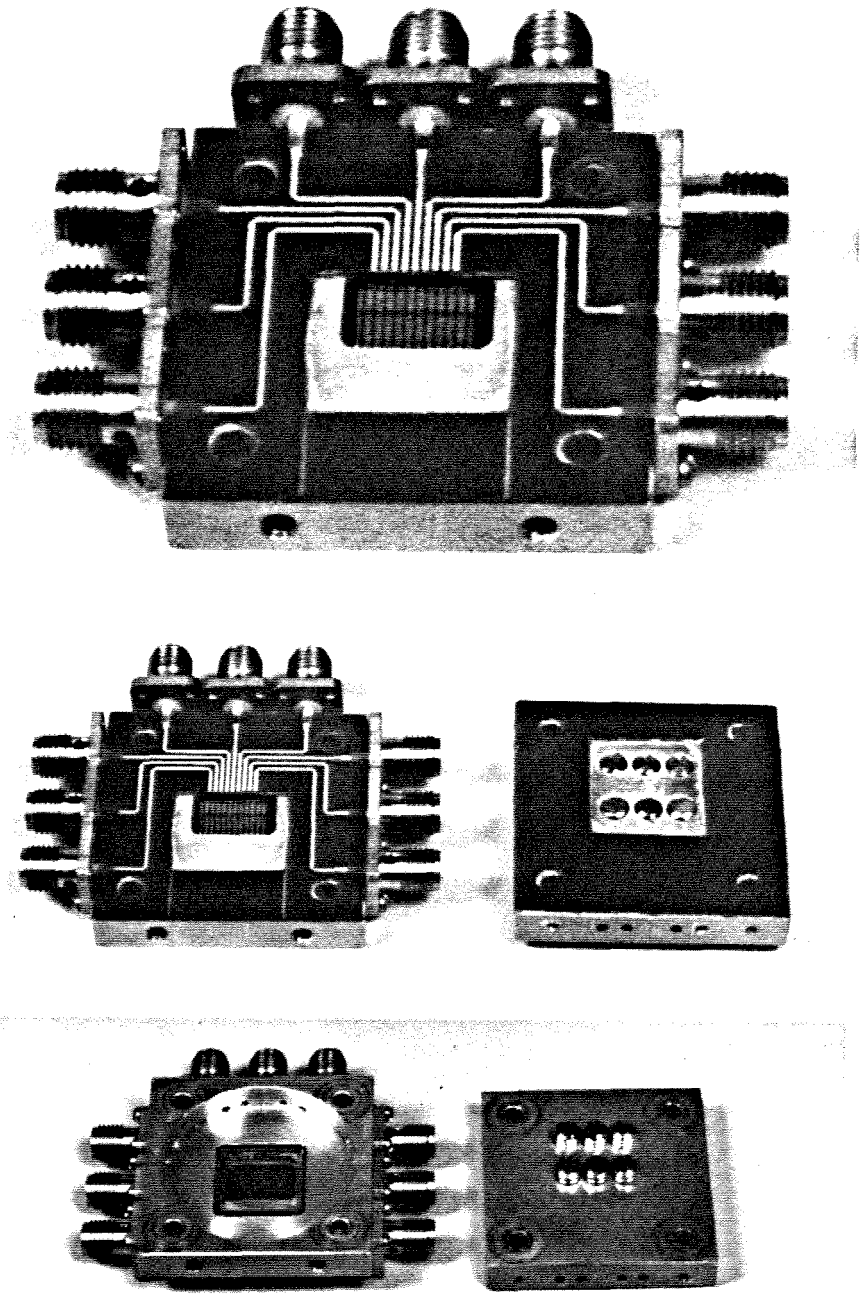

Fig. 4.9. Close up view of the front piece (top). Parts of the package (bottom).

reflection losses are by looking at the reflections in Fig. 4.10. The refraction index at millimeter wavelengths and at optical wavelengths is similar. The theory and the measured performance of the matching layer have been discussed in Chap. 3.

4.6. DC Parameters of the Schottky Diode

Fig. 4.11 shows the current-voltage measurement performed on the Schottky diodes after each fabrication. The series resistance, the ideality factor and the barrier height are obtained by fitting the diode equation to the measured data represented by circles. The least mean square fit method is used and the calculation is done by a personal computer. Appendix B gives the detail description of the curve fittings. After packaging, the measured series resistance is 15.9 Ω, the ideality factor is 1.20, and the barrier height is 0.755 eV. The breakdown voltage (at 1 μA) is 5 volt and the shunt resistance is 7 MΩ, measured from the curve tracer. The estimated zero bias junction capacitance is 5.5 fF.

The series resistance and the capacitance of the Schottky diode are also calculated from the geometry and the doping concentrations of the diode. Appendix C gives the detail description of the calculation. The calculated results are listed in Table 4.1. The measured series resistance (15.9 Ω) is somewhat higher than the theoretical value (13 Ω). The extra resistance might be due to the undepleted n layer introduced by the forward bias during I-V measurement and errors in estimating parameters of our Schottky diode. The calculated results show that the contact resistance 5.14 Ω is the major contributor of the series resistance and should be reduced by increasing the doping and the thickness of the n^+ layer if possible. The calculation also shows 3.54 fF parasitic capacitance that is mainly due to the fringing field within the small gap on the semi-insulating area as shown in Fig. 4.12. The cutoff frequency of our planar Schottky diode is

1.1 THz, calculated from the RC product at zero bias.

Table 4.1. Theoretical Series Resistance and Capacitance of Our Planar Schottky Diode.

R_S^*	R_{n1}	R_{n2}	R_{n3}	R_C	R_{A0}	R_{A1}	R_{A2}	R_{O1}	R_{O2}
13 (15.9)**	0	1.35	1.02	5.14	2	0.66	1.35	0.36	1.08

C_j^{***}	C_p	C_{f1}	C_{f2}
5.5	3.54	0.23	3.31

* : all resistances are in ohms.

** : measured from I–V characteristic

*** : all capacitances are in fF

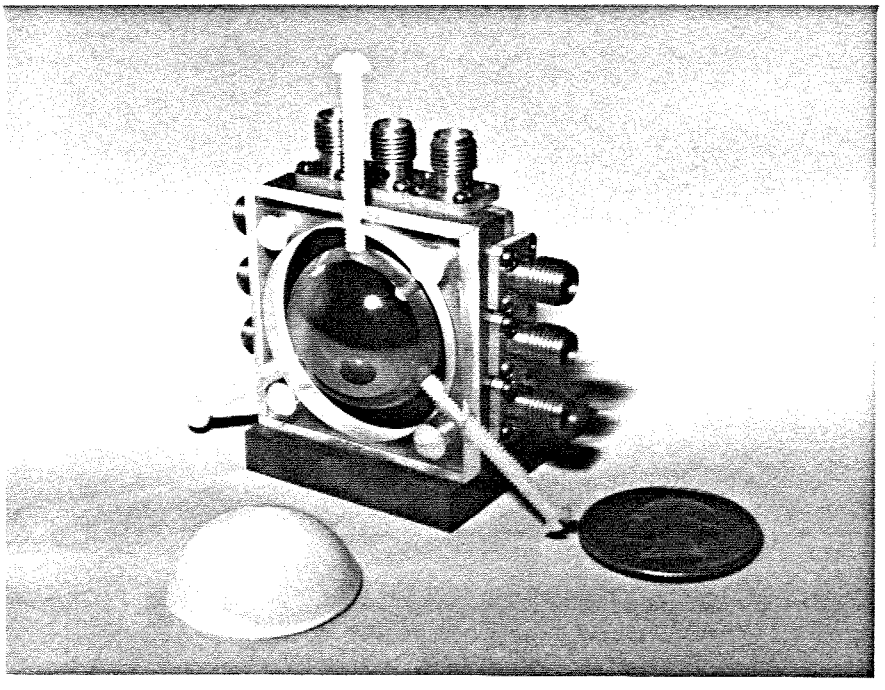

Fig. 4.10. Front view of the assembly with silicon lens. The white polystyrene cap is used to reduce the reflection loss of the silicon lens.

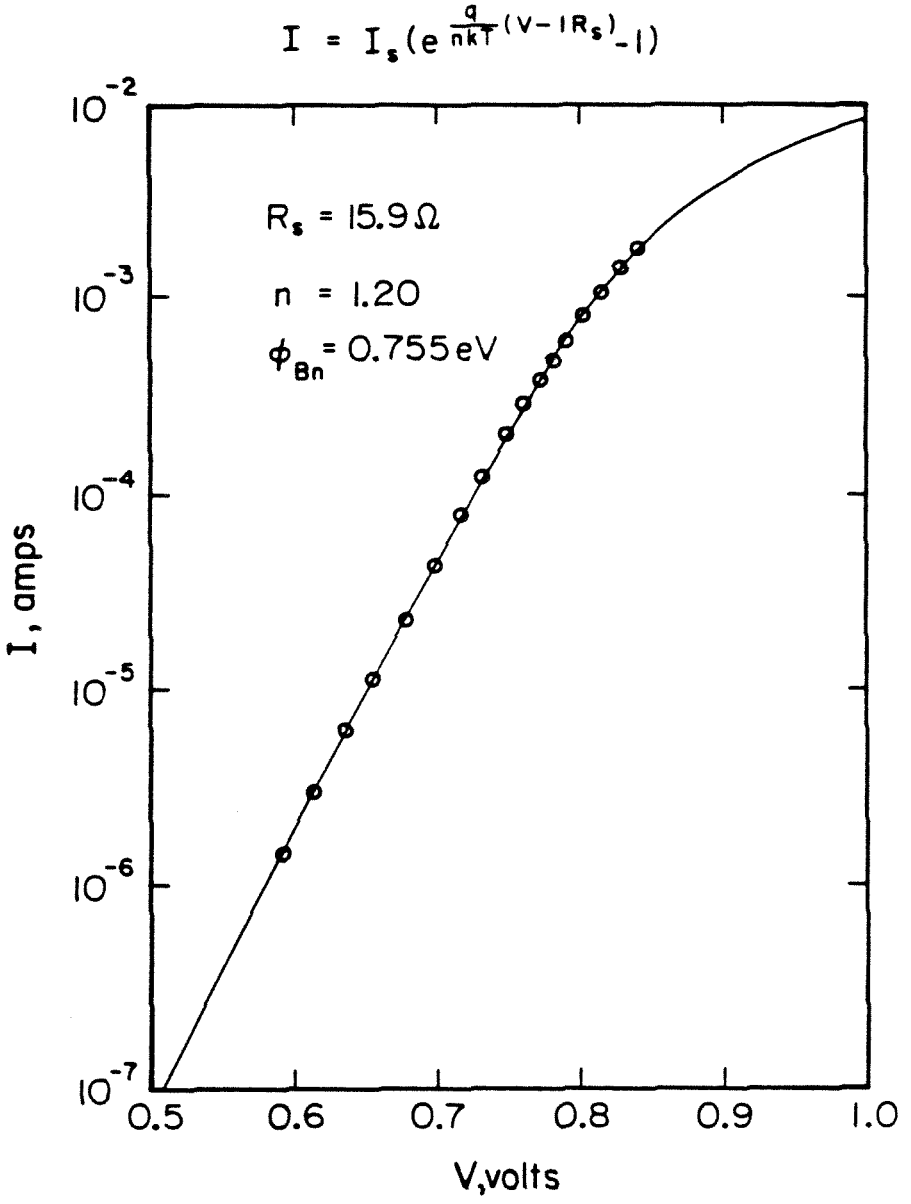

Fig. 4.11. I–V characteristic of our planar Schottky diode.

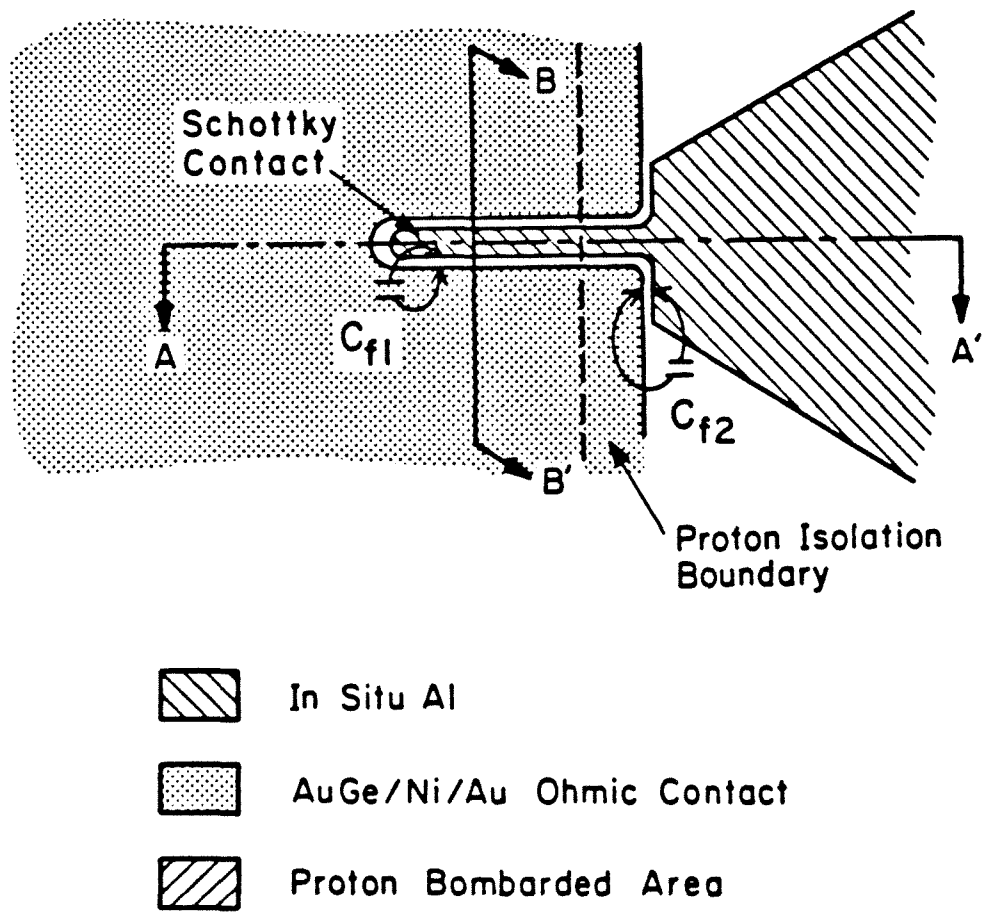

Fig. 4.12. Parasitic capacitance due to the fringing field within the gap. C_{f1} is the fringing capacitance on the n^+ area and C_{f2} is the fringing capacitance on the semi-insulating area.

References

[1] C. Zah el al., "Progress in Monolithic Schottky Diode Imaging Arrays," *Proceeding of 9th Int. Conf. on Infrared and Millimeter Waves*, W–4–2, Oct. 1984.

[2] W. M. Kelly and G. T. Wrixon, "Optimization of Schottky-Barrier Diodes for Low-Noise, Low-Conversion Loss Operation at Near-Millimeter Wavelengths," *Infrared and Millimeter Waves*, vol. 3, pp. 77–110, K. J. Button, ed., Academic Press, New York, 1980.

[3] M. V. Schneider, " Metal-Semiconductor Junctions as Frequency Converters," *Infrared and Millimeter Waves*, vol. 6, pp. 210–275, K. J. Button, ed., Academic Press, New York, 1980.

[4] M. N. Afsar, "Dielectric Measurements of Millimeter-Wave Materials," *IEEE*, vol. MTT–32, No. 12, Dec. 1984.

[5] T. Sugiura el al., "12-GHz-Band Low-Noise GaAs Monolithic Amplifiers," *IEEE*, vol. ED–30, No. 12, Dec. 1983.

[6] M. Ogawa, "Alloying Behavior of Ni/Au-Ge film on GaAs," *J. Appl. Phys.*, vol. 51, No. 1, pp. 406–419, 1980.

[7] H. H. Berger, "Models for Contacts to Planar Devices," *Solid-State Electronics*, vol. 15, pp. 145–158, 1972.

[8] J. L. Heaton et al., "Millimeter Wave GaAs Mixer Diodes Fabricated Using Selective Epitaxial Deposition or Deep Mesa Etching," *Proc. IEEE/Cornell Conf. on High-Speed Semiconductor Devices and Circuits*, pp. 47–59, Aug. 1984.

[9] J. A. Griffn et al., "Formation of Planar n^+ Packets in GaAs for Mixer Diode

Fabrication," *IEEE*, vol. ED–31, No. 8, Aug. 1984.

[10] D. C. Dávanzo, "Proton Isolation for GaAs Integrated Circuits," *IEEE*, vol. MTT-30, No. 7, pp. 955–962, July 1982.

[11] J. P. Donnelly and F. J. Leonberger, "Multiple-Energy Proton Bombardment in n^+-GaAs," *Solid-State Electronics*, vol. 20, pp. 183–189, 1977.

[12] D. B. Rutledge, D. P. Neikirk and D. P. Kasilingam, "Integrated-Circuit Antennas," *Infrared and Millimeter Waves*, vol. 10, Chap. 1, pp. 1–90, K. J. Button, ed., Academic Press, New York, 1983.

Chapter 5

Video Detection

The envelope of the high frequency signal can be detected by direct rectification of the signal by nonlinear devices such as Schottky diodes. This detection scheme is commonly known as video detection or direct detection [1]. The sensitivity of video detection is lower than heterodyne detection. However, video detection circuits are much simpler and this makes video detection an inexpensive and attractive method for measuring power in many laboratory experiments. In addition, the detector is operated in the small signal region which eases the theoretical analysis. Fig. 5.1 shows equivalent circuits of a Schottky diode video detector. The theoretical calculation of system video responsivity is included in Appendix D. By comparing experimental results from video detection with theoretical predictions, we will be able to obtain some useful information about our imaging systems and devices, such as the optimum f-number of the objective lens, parasitic capacitance, antenna efficiency and imaging properties.

5.1. Experimental Set-Up

Most of measurements were done at 94 GHz at Caltech, with the remainder at UCLA. Fig. 5.2a shows the experimental set-up for video detection. The signal is generated by a 94 GHz Gunn diode and is square-wave modulated at 1 KHz. The signal is radiated from a standard-gain horn. The receiver shown in Fig. 5.2b is put in the far field 100 inches away. An objective lens made out of TPX plastic focuses the signal onto the array through a silicon substrate lens. Its focal length is calculated from the geometry of the lens to be 8.58 cm. The system video responsivity is calculated from the ratio of the diode output voltage to the signal power incident on the objective lens. The signal power is measured by an

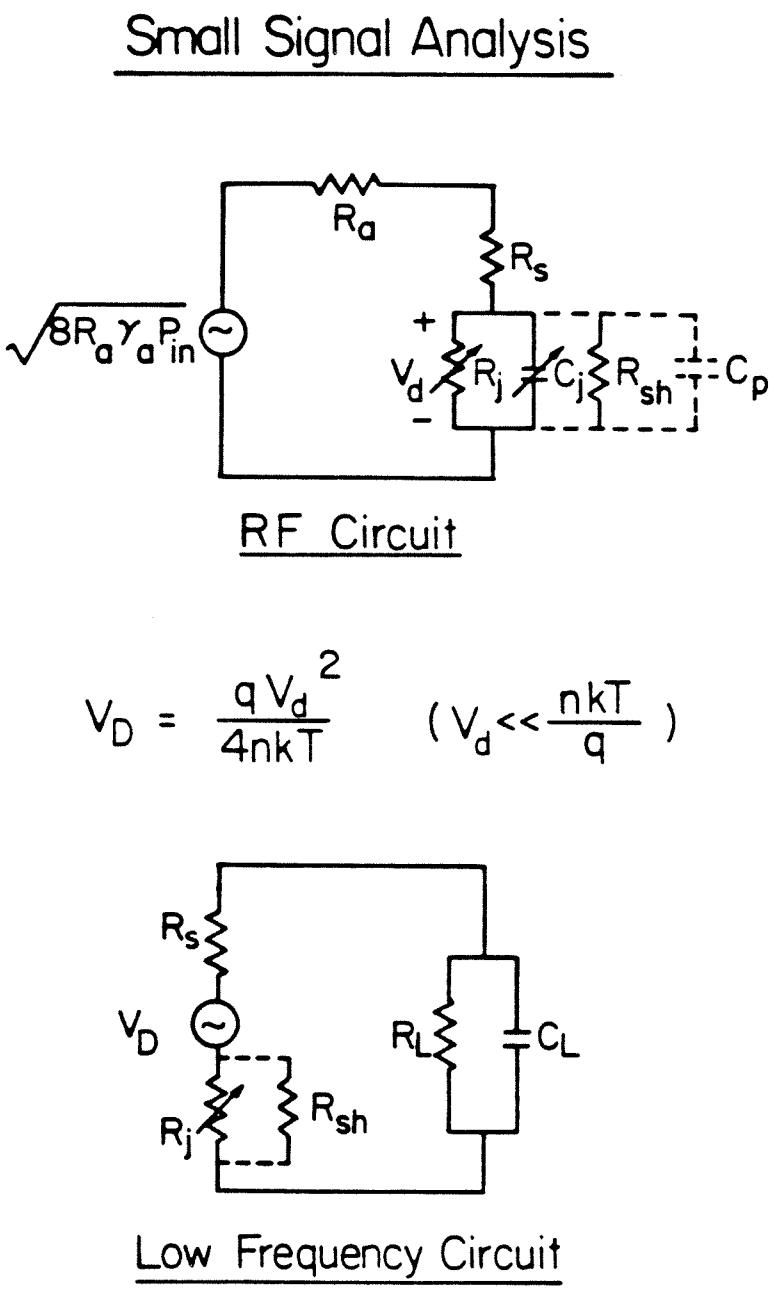

Fig. 5.1. Equivalent circuits of a Schottky diode video detector.

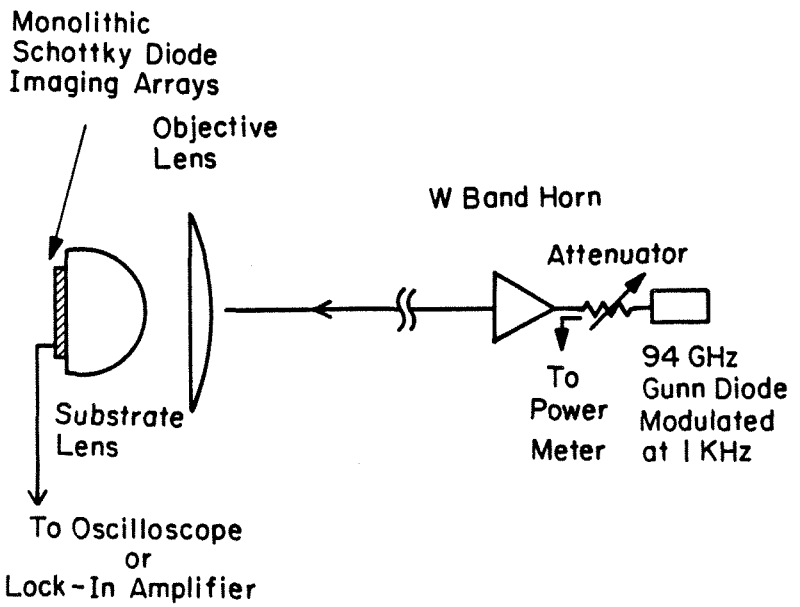

(a)

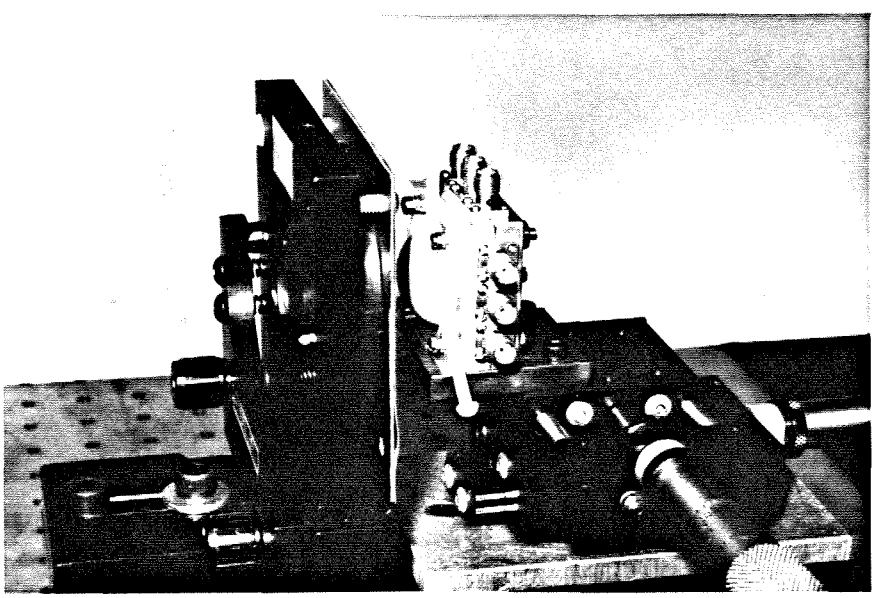

(b)

Fig. 5.2. (a) Experimental set-up for video detection. (b) Close-up view of the receiver.

HP 432A power meter. The gain of the standard gain horn is calculated from the horn dimensions. The power incident on the objective lens can be calculated from standard antenna formulas. The output voltage is measured by a lock-in amplifier or an oscilloscope. The 75–170 GHz measurements are done at UCLA with a similar set-up, except that the signal is generated by a backward-wave oscillator and modulated by a mechanical chopper at 110 Hz. W band horn is used for the 75–110 GHz measurements while D band horn is used for the 110–170 GHz measurements. The distance between the receiver and the horn is 62 inches.

5.2. Detected Voltage versus Input Power

Fig. 5.3 shows the detected voltage from a Schottky diode versus 94 GHz input power. The bias current is 10 μA and the load resistance is 100 KΩ. It acts as a square law detector until the detected voltage reaches nkT/q, or about 30 mV. This agrees with Eq. 2 in Appendix D. The system video responsivity is 810 V/W. One data point at very low input power is slightly off the line. This error probably comes from drift in the setting of the power-meter zero. The noise equivalent power is 2×10^{-11} watt/$\sqrt{\text{Hz}}$ at 100 KHz modulation frequency.

5.3. System Video Responsivity versus Aperture Size

Fig. 5.4 shows the system video responsivity versus front aperture size. In this experiment, an aluminum plate with a hole in the middle (Fig. 5.5a) serves as an aperture stop. For convenience, it is put on the backside of the objective lens. However, the input power is calculated from the front aperture size determined from the ray tracing diagram in Fig. 5.5b. By the same ray tracing diagram, the maximum angle α inside the silicon lens is found for each aperture size. This

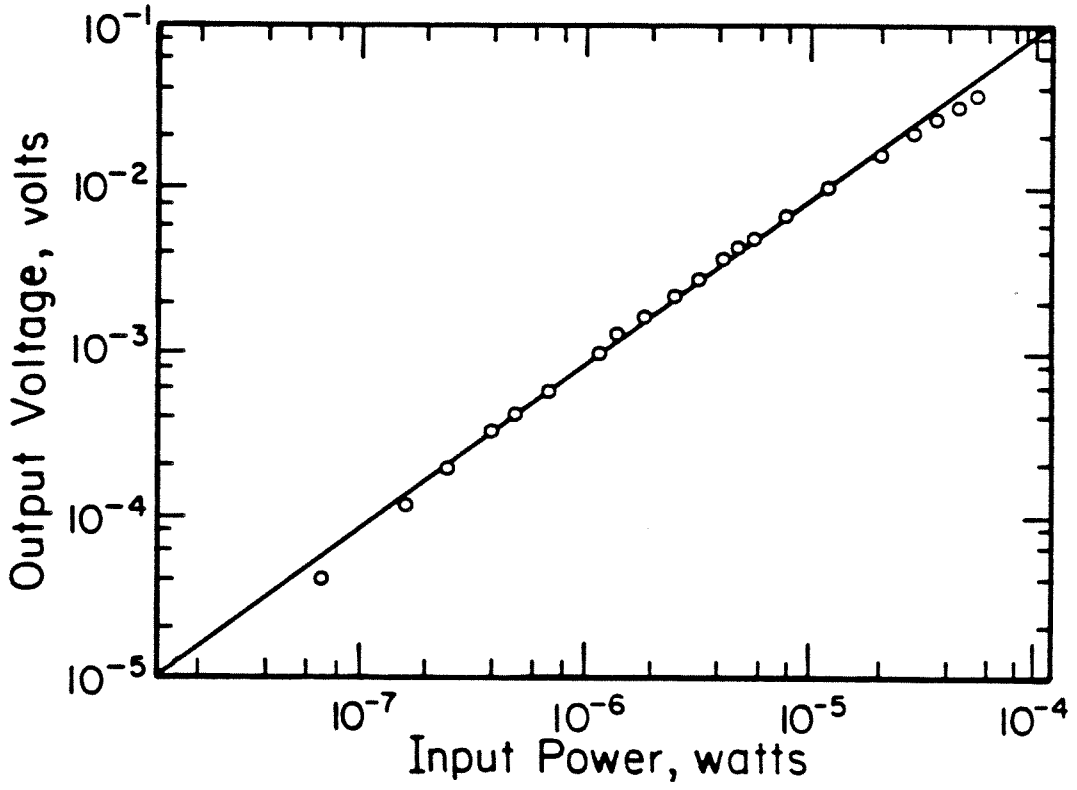

Fig. 5.3. Detected voltage from a Schottky diode versus 94 GHz input power. The bias current is 10 μA and the load resistance is 100 KΩ. One data point at very low input power end is slightly off the line. This error probably comes from drift in the setting of the power-meter zero.

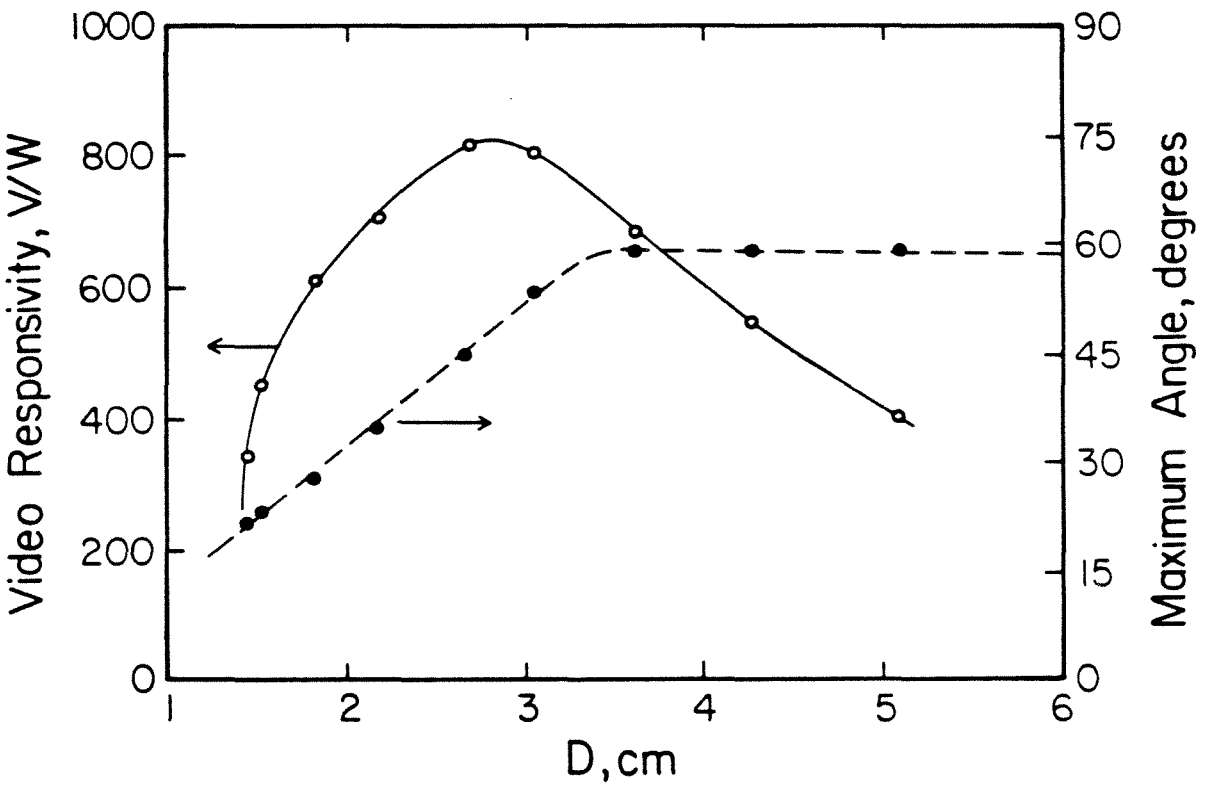

Fig. 5.4. System video responsivity and maximum angle inside the silicon lens versus front aperture size D

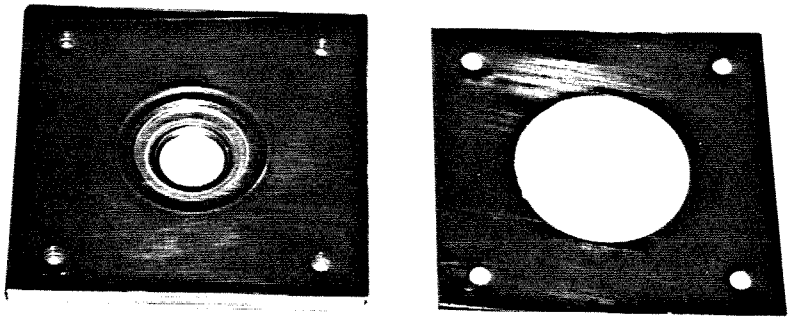

Fig. 5.5a. Aperture stops made out of aluminum plates.

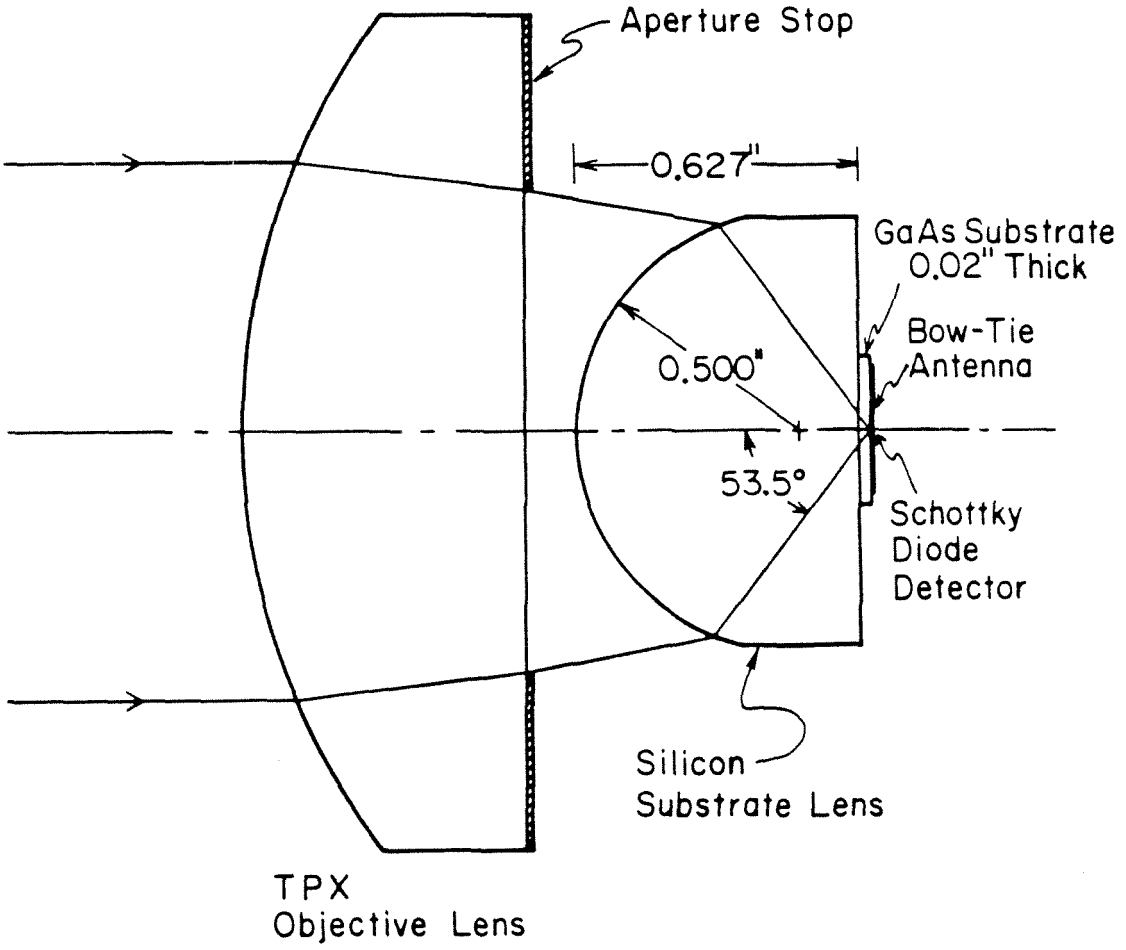

Fig. 5.5b. Ray tracing diagram of lens-coupled antenna in scale. The maximum angle α inside the silicon lens changes with the aperture size.

is also shown in Fig. 5.4. For aperture sizes larger than 3.6 cm, the maximum angle remains 59°, limited by the substrate lens. The diode is biased at 10 μA with a 100 KΩ load resistance. Fig. 5.4 shows a peak system video responsivity of 820 V/W at a 2.7 cm front aperture. This corresponds to a maximum angle of 45° ($f/2.4$ objective lens).

This peak can be understood by considering spillover efficiency and taper efficiency [2]. The spillover efficiency causes the responsivity to decrease for small apertures. If the Airy spot at the focal plane is larger than the effective area of the antenna, the power outside the antenna effective area will not be received efficiently. The Airy spot is inversely proportional to the square of aperture diameter [3] while the gain of the antenna determines its effective area [4]. Therefore, the responsivity decreases roughly as the square of the aperture diameter for very small apertures. On the other hand, the responsivity goes down for large aperture because of the fixed beamwidth of the feed antenna. The power outside the main beam will not be coupled efficiently into the detector. Consequently, the responsivity decreases as the reciprocal of the square of the aperture diameter for very large apertures. At the peak, the spillover efficiency and the taper efficiency are approximately equal.

5.4. System Video Responsivity versus Bias Current

The 94 GHz system video responsivity versus bias current at two different load impedances is shown in Fig. 5.6. The dots are the measured experimental data. The solid lines are theoretical curves [derived in Appendix D] which are fitted to the experimental data by choosing system coupling efficiency of 24% and a parasitic capacitance of 3 fF. All the circuit parameters used in the calculations are listed in Table 5.1.

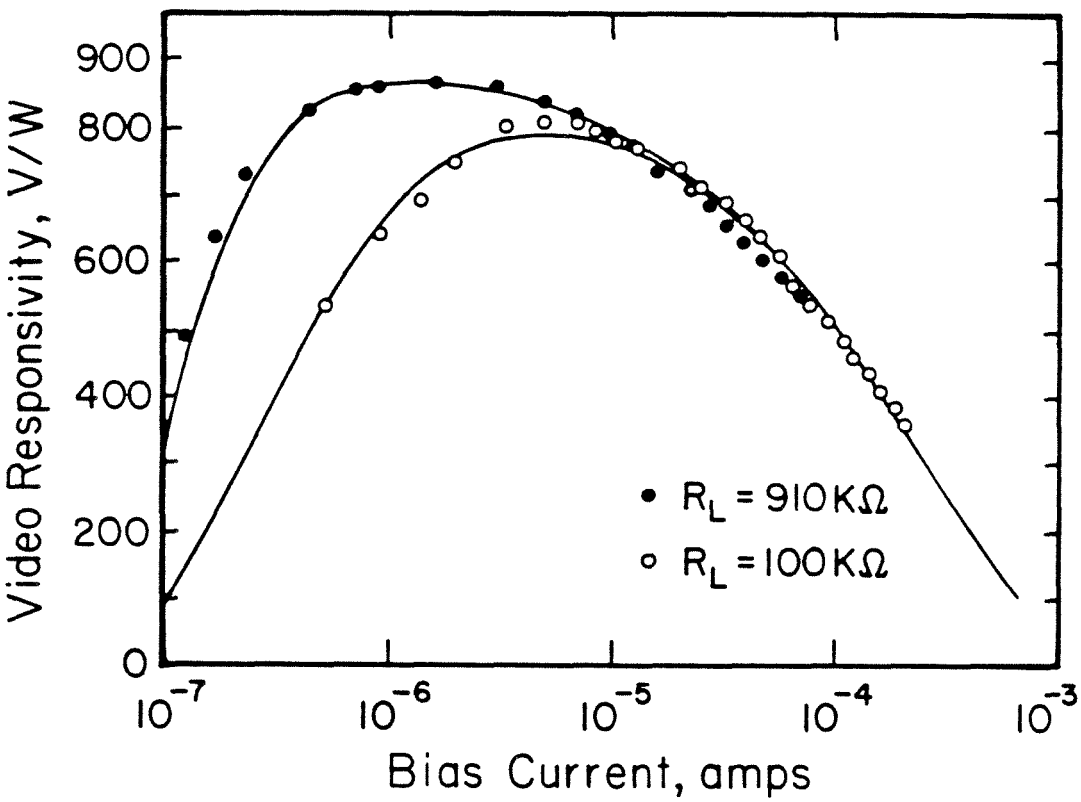

Fig. 5.6. The 94 GHz system video responsivity versus bias current at two different load impedances. The dots are measured experimental data. The solid lines are theoretical curves.

Table 5.1. Circuit parameters used in system video responsivity calculation in Fig. 5.6 & 5.8.

	γ_a	R_a	R_s	C_0	Φ_{bn}	C_p
Fig. 5.6	0.24	90Ω	15.9 Ω	5.5 fF	0.755 eV	3 fF
Fig. 5.8	0.23	90Ω	15.9 Ω	5.5 fF	0.755 eV	3 fF

	n	R_{sh}	R_L	C_L	f	f_0
Fig. 5.6	1.20	7MΩ	910/100 KΩ	500 pF	94 GHz	1 KHz
Fig. 5.8	1.20	7MΩ	100 KΩ	500 pF	60–180 GHz	110 Hz

γ_a: system coupling efficiency

R_a: antenna impedance

R_s: series resistance of the diode

C_0: zero bias junction capacitance

Φ_{bn}: barrier height of the metal-semiconductor barrier

C_p: parasitic capacitance

n: ideality factor of the diode

R_{sh}: shunt resistance of the diode

$R_L \parallel 1/(j\Omega C_L)$: load impedance

f: signal frequency

f_0: chopper frequency

The system coupling efficiency of 24% is attributed to the antenna coupling efficiency and losses due to the reflection and the absorption in lenses. The reflection and absorption losses in TPX objective lens and the polystyrene matching cap are about 0.5 dB [5]. The absorption loss in silicon with 1000 Ω-cm resistivity is estimated to be 0.6 dB/cm from data in [5]. The total absorption loss in the

silicon lens is about 1.0 dB. The remaining loss is directly due to the antenna coupling efficiency which is 4.7 dB (34%). The detailed loss breakdown is in Table 5.2.

Table 5.2. Estimated system losses

TPX objective lens	0.3 dB reflection loss
	0.1 dB absorption loss
Polystyrene matching cap	0.1 dB reflection loss
Silicon lens	1.0 dB absorption loss
Antenna coupling efficiency	4.7 dB (34%)
System coupling efficiency	6.2 dB (24%)

According to the calculation in Appendix C, the parasitic capacitance is mainly due to the small gap between the ohmic contact and the aluminum on the semi-insulating area, rather than the n^+ area (see Fig. 5.7). It results from the fringing field penetrating the semi-insulating substrate, which has a high dielectric constant of 12.9. It should be possible to reduce this parasitic capacitance by making the apexes of bow-tie narrower, and increasing the gap between the aluminum and the ohmic contact.

5.5. System Video Responsivity versus Frequency

In order to verify the circuit model and the performance of the matching cap, the system video responsivities were also measured from 75 GHz–170 GHz with and without the polystyrene matching cap shown in Fig. 5.8. The solid lines are calculated by using the equivalent circuits in Fig. 5.1. All the circuit parameters are listed in Table 5.1. The dots are the experimental values. Uncertainties in power-meter calibration factors and system losses contribute to the scatter in

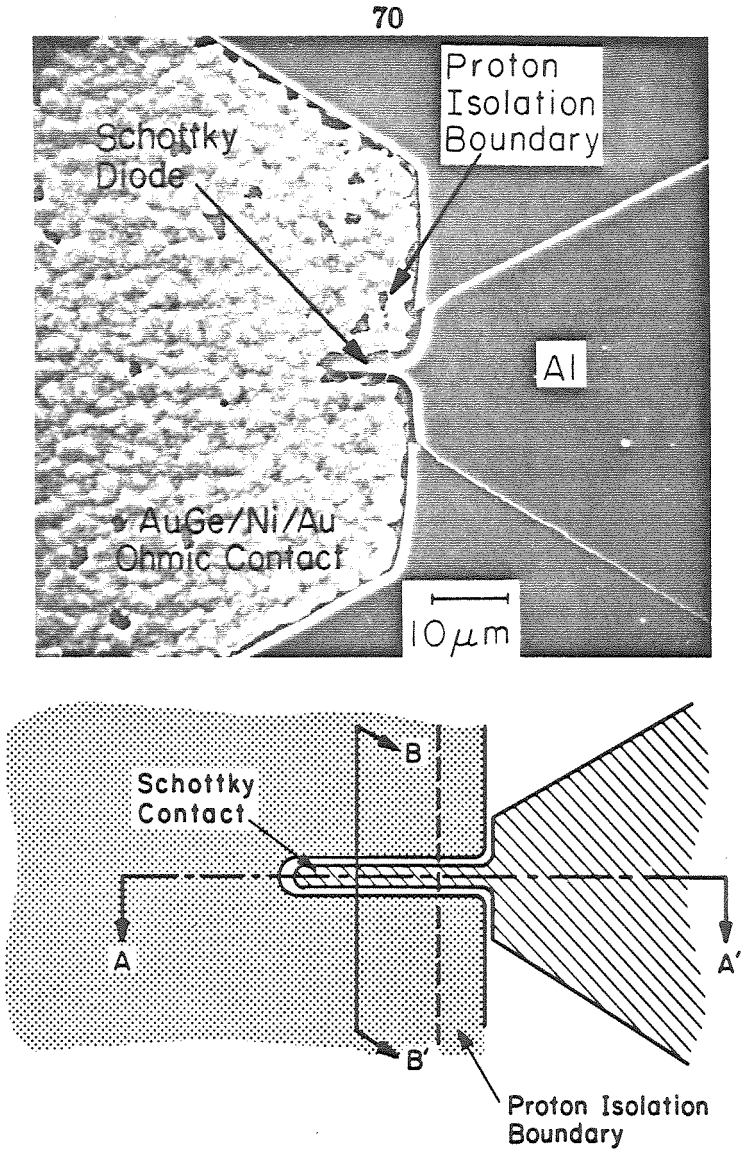

Fig. 5.7. SEM photograph of a planar Schottky diode (top). The schematic drawing, not in scale (bottom). Parasitic capacitance is due to the fringing field within the gap. C_{f1} is the fringing capacitance on the n^+ area and C_{f2} is the fringing capacitance on the semi-insulating area.

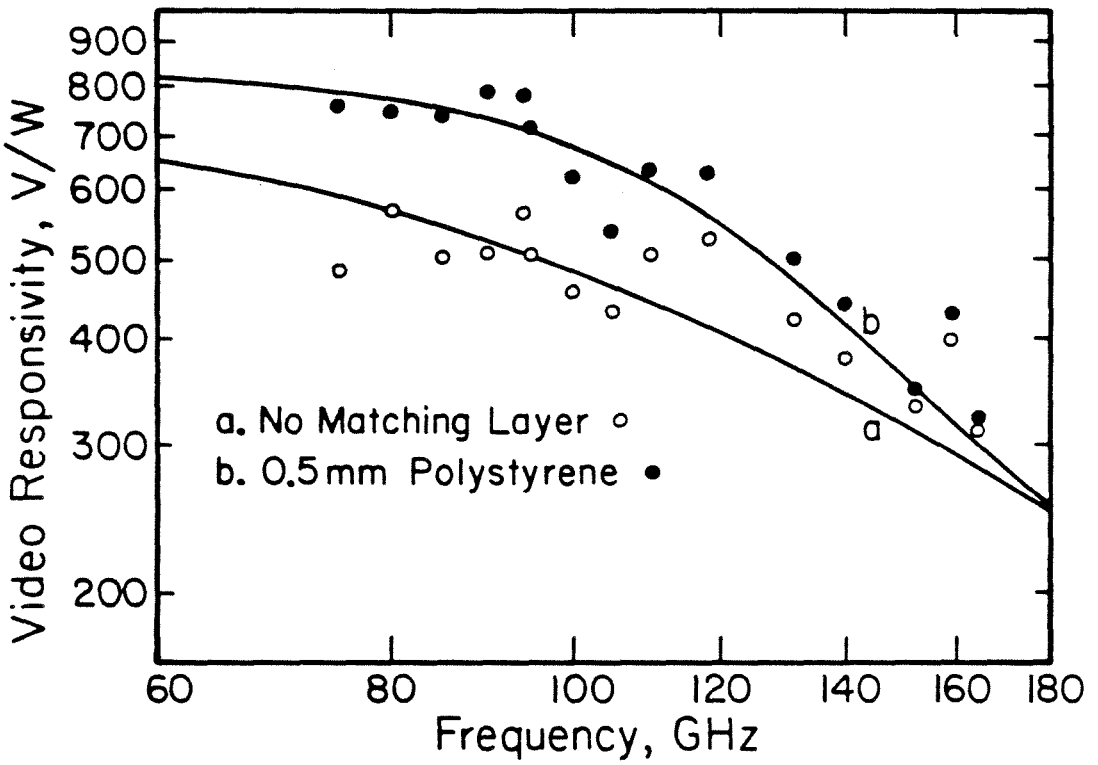

Fig. 5.8. System video responsivity versus frequency in log scale with and without the polystyrene matching cap. The dots are measured experimental data. The solid lines are the theoretical curves.

the points. The system coupling efficiency is chosen by curve fitting to be 23%. The 0.5 mm polystyrene cap gives a 1.5 dB improvement at the design frequency of 94 GHz, where the cap acts as a quarter-wave matching layer, but very little improvement at 170 GHz, where the cap acts as a half-wave window [6]. The 3 dB cutoff frequency of the diode is about 140 GHz. One can see the circuit model works quite well over a frequency range of 75–170 GHz even though the skin effect is not taken into account. It also proves that our planar Schottky diode is good for 100 GHz applications and the bow-tie antenna has an octave frequency bandwidth at least. The bow-tie antenna integrated with an SIS junction has been domenstrated to have a bandwidth of two octaves (116 GHz–466 GHz) by M. J. Wengler [7].

5.6. The Angular Field of View of the Imaging System

The imaging properties of the system are obtained by studying both the angular field of view and the spot response. The angular field of view of the imaging system has been measured by rotating the receiver as shown in Fig. 5.9 [8]. The entire receiver is rotated about the center of the objective lens. In this way it is possible to shift the focal spot from one antenna to the next. Fig. 5.10 shows the peak angle for each antenna and the system video responsivity for each antenna at its peak angle. The front aperture is set to be 3 cm. The full angular field of view determined from the half power points is approximately 40°, with an angular separation between adjacent antennas of 7.4°. The off-center antennas suffer from the power loss due to rays missing the substrate lens as well as the large angle of incidence at the focal plane (see Fig. 5.9). A larger substrate lens should alleviate this loss.

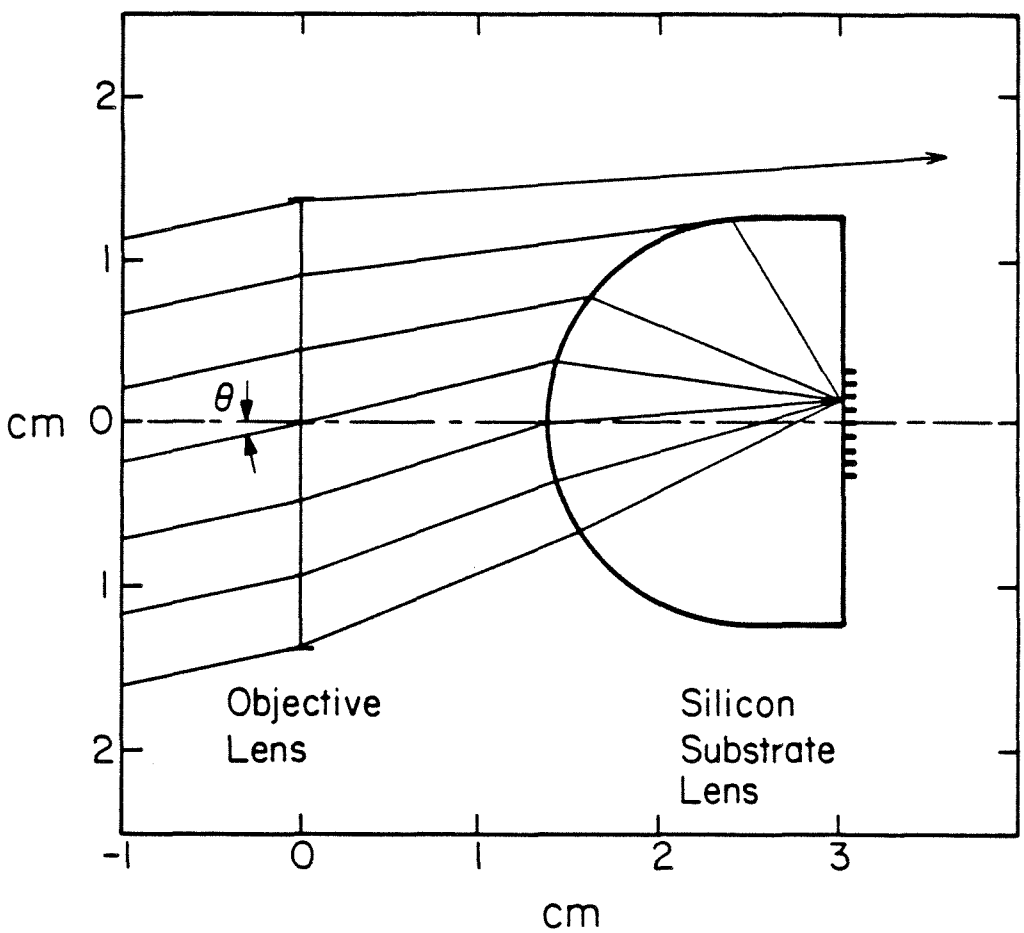

Fig. 5.9. The ray tracing diagram of a plane wave coming in a angle with respect to the optical axis. Each bar at the interface represents an antenna. The ray on the top misses the silicon lens after focusing by the objective lens.

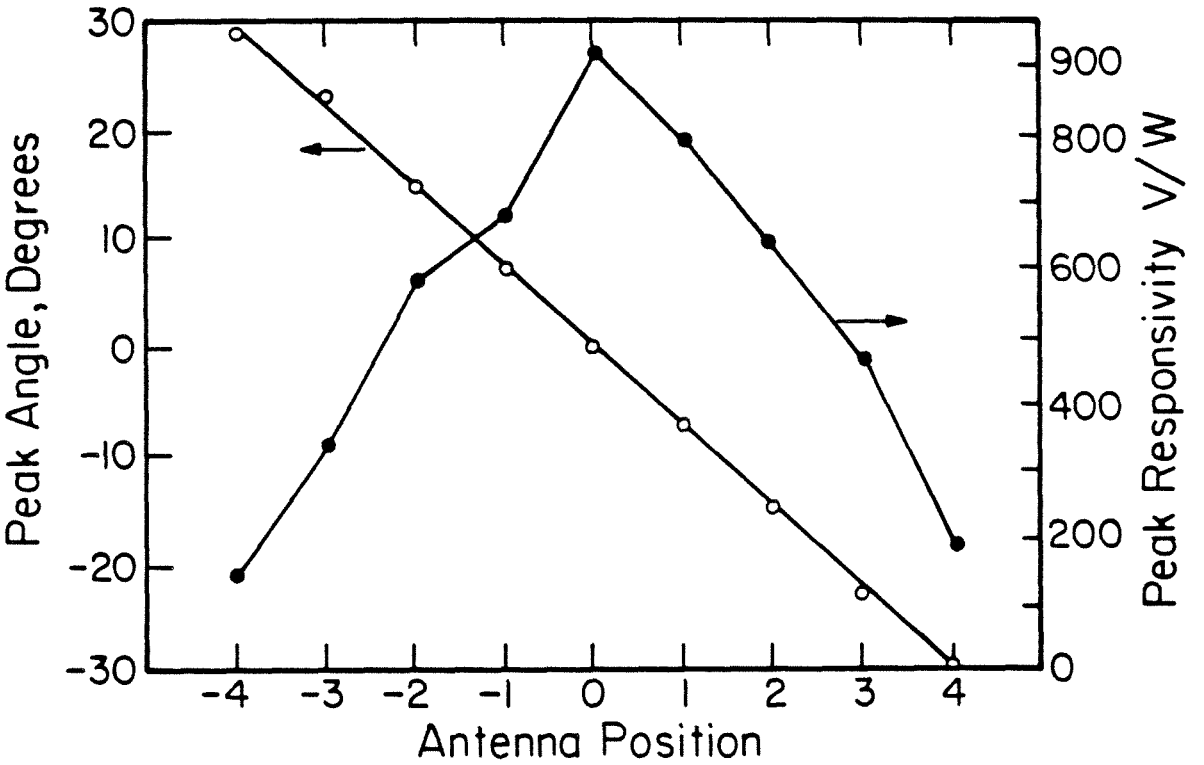

Fig. 5.10. Angular field of view of 94 GHz imaging system with 3 cm front aperture.

5.7. The Spot Response of the Imaging System

Using the same rotation technique, we measure the spot response of the imaging system by monitoring the output of the center antenna while the angle changes. Fig. 5.11 shows the measured spot response in the H-plane of the antenna which corresponds to a rotation axis perpendicular to the imaging line. It also shows the theoretical Airy pattern calculated by the following formula [9,10]:

$$\frac{I(\theta)}{I(0)} = \left[\frac{2J_1(kD\sin\theta/2)}{kD\sin\theta/2}\right]^2 \tag{5.1}$$

where D is the aperture diameter of the objective lens, θ is the angle between the optical axis and the incoming plane wave and $k = 2\pi/\lambda$. Although we use a 3 cm front aperture, the experiment data in circles fit the Airy pattern of a 2.5 cm aperture. Presumably this is due to non-uniform illumination of the aperture by the bow-tie antenna or edge effects of the aluminum stop. The 2.5 cm front aperture corresponds to a half antenna beamwidth of 40° inside the silicon lens, obtained from Fig. 5.4. The triangles in Fig. 5.11 are the experimental data obtained by normalizing the output voltage from the adjacent antenna position to its peak system video responsivity shown in Fig. 5.10, when a plane wave is normally incident upon the objective lens. These also lie on the Airy pattern for a 2.5 cm aperture.

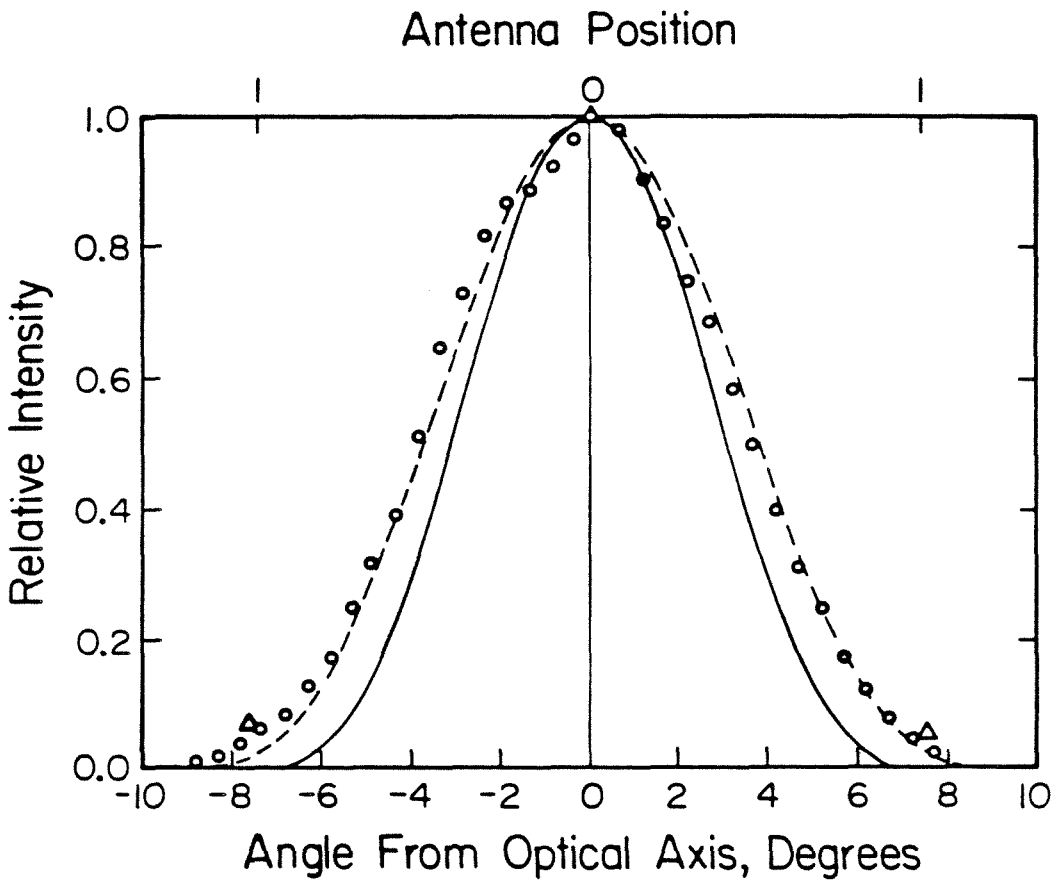

Fig. 5.11. Spot response for the 94 GHz imaging system with 3 cm front aperture. Data in circles are obtained by the rotation technique. Data in triangles are obtained by the array with a plane wave normally incident upon the objective lens. The calculated Airy patterns are shown in solid line for 3 cm aperture and dash line for 2.5 cm aperture.

References

[1] M. V. Schneider, "Metal-Semiconductor Junction as Frequency Converters," *Infrared and Millimeter Waves*, vol. 6, Chap. 4, pp. 209–275, K. J. Button, ed., Academic Press, New York, 1983.

[2] C. Zah, R. C. Compton and D. B. Rutledge, "Efficiencies of Elementary Integrated-Circuit Feed Antenna," *Electromagnetics* 3, pp. 239–254, 1984.

[3] E. Hecht and A. Zajac, *Optics*, Chap. 10, pp. 352, Addison-Wesley Publishing Company, Reading, Mass., 1974.

[4] S. Ramo, J. R. Whinnery and T. van Duzer, *Fields and Waves in Communication Electronics*, Chap. 12, pp. 716–717, John Wiley & Sons, Inc., New York, 1965.

[5] M. V. Afsar and K. J. Button, "Millimeter-Wave Dielectric Properties of Materials," *Infrared and Millimeter Waves*, vol. 12, Chap. 1, pp. 1–42, 1984.

[6] C. Zah and D. B. Rutledge, "A Polystyrene Cap for Matching a Silicon Lens at Millimeter Wavelengths," *to be published in J. of Infrared and Millimeter Waves*, Sept. 1985.

[7] M. J. Wengler et al., "A Low Noise Receiver for Millimeter and Submillimeter Wavelengths," to be published, *Int. J. of Infrared and Millimeter Waves.*

[8] D. P. Neikirk, "Integrated Detector Arrays for High Resolution Far-Infrared Imaging," *Ph. D. Thesis*, California Institute of Technology, 1984.

[9] Born and Wolf, *Principles of Optics*, pp. 396, 6th ed., Pergamon Press, New York, 1980.

[10] F. A. Jenkins and H. E. White, *Fundamentals of Optics*, pp. 166–167, 4th ed., Mcgraw-Hill, New York, 1976.

Chapter 6

Heterodyne Detection

In addition to video detection, our imaging array has been tested as a single-ended mixer. In this chapter, the measured double-sideband (DSB) and single-sideband (SSB) results will be discussed. The performances were evaluated under different DC and local oscillator power biases.

6.1. Definitions

In heterodyne detection, a nonlinear mixing element combines a low-level high frequency input signal (RF) with a local oscillator signal (LO) to produce a signal at the difference or intermediate frequency (IF). This IF signal can be amplified and processed by low-frequency circuits. The LO power is usually many orders of magnitude larger than the RF power in order to drive the mixer over a large portion of its nonlinear range. Since the LO also acts as a reference signal, the IF signal preserves the phase information of the RF signal. Therefore, heterodyne detection is coherent. The IF frequency can often be chosen high enough so that the $1/f$ noise of the mixer is negligible. In general, heterodyne detection gives much better sensitivity and noise performance than video detection [1].

A figure of merit often used for mixers is the noise temperature and the conversion loss [2]. The conversion loss L_M of a mixer in decibels is defined as

$$L_M(dB) = 10\log\left(\frac{P_{RF}}{P_{IF}}\right) \tag{6.1}$$

where P_{RF} and P_{IF} are the signal and IF powers at the respective ports. If equal power is fed into both input ports (signal and image), the DSB conversion loss can be written as

$$L_M(\mathrm{DSB}) = \frac{1}{1/L_S + 1/L_I} \tag{6.2}$$

where L_S and L_I are power conversion losses between the signal and the IF ports and between the image and the IF ports, respectively. The receiver noise temperature T_R is defined as the temperature of an input load which generates the same amount of the noise as the receiver itself at the IF port. The single-sideband noise temperature of a receiver, i.e. a mixer followed by an IF amplifier, is given by

$$T_R(\text{SSB}) = T_M(\text{SSB}) + L_S T_{IF} \tag{6.3}$$

where T_{IF} is the noise temperature of the IF amplifier and T_M is a measure of the noise created in the mixing process. For some occasions, a double-sideband noise temperature is measured, which is defined as

$$T_R(\text{DSB}) = T_M(\text{DSB}) + L_M(\text{DSB}) T_{IF} \tag{6.4}$$

and is related to $T_R(\text{SSB})$ by

$$T_R(\text{DSB})/L_M(\text{DSB}) = T_R(\text{SSB})/L_S \tag{6.5}$$

For a dual-response receiver with $L_S = L_I$, one obtains

$$L_M(\text{DSB}) = L_S/2 \tag{6.6}$$

$$T_R(\text{DSB}) = T_R(\text{SSB})/2 \tag{6.7}$$

$$T_M(\text{DSB}) = T_M(\text{SSB})/2 \tag{6.8}$$

In this work, the broadband bow-tie antenna couples the power to the planar Schottky diode used as a mixer. It is a dual-response receiver.

6.2. Experimental Set-Up

Fig. 6.1 shows the set-up for double-side band heterodyne detection measurements. The dual-beam interferometer is used as a diplexer to combine the signal

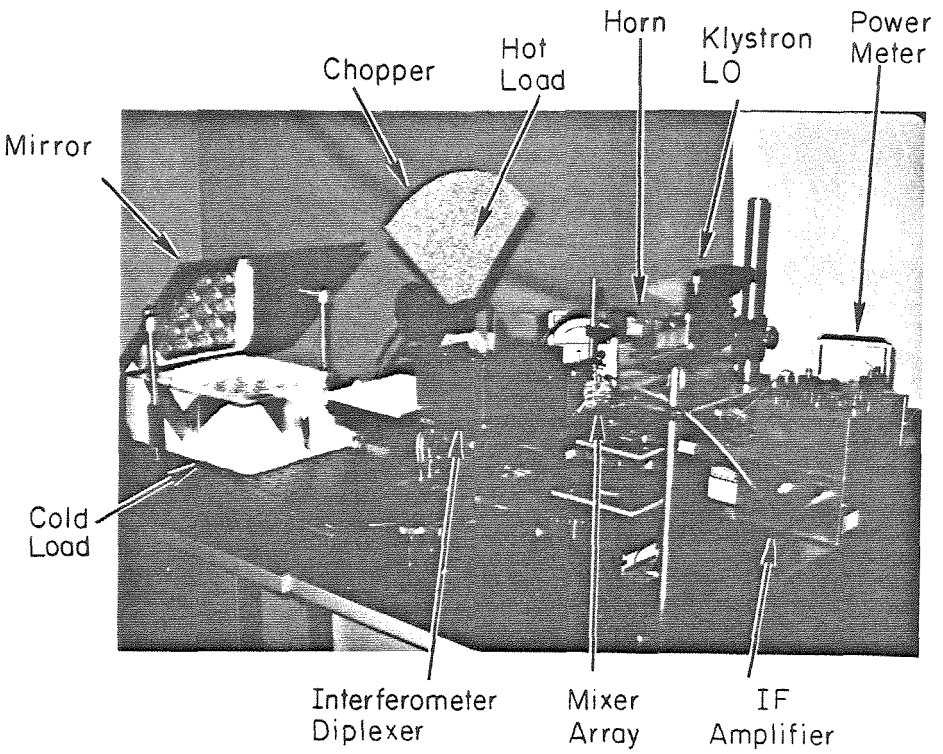

Fig. 6.1a. Photograph of double-sideband heterodyne detection set-up.

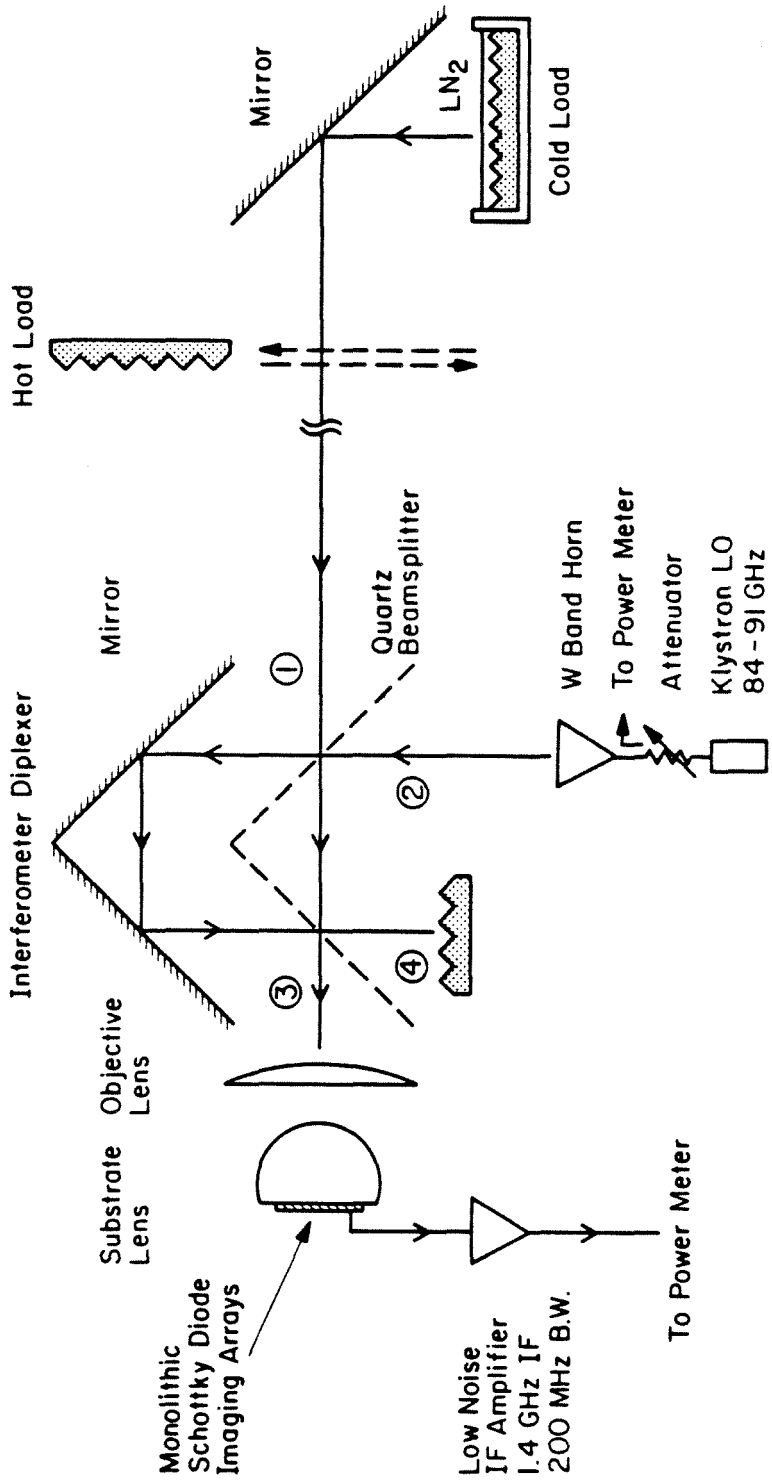

Fig. 6.1b. Schematic drawing of double-sideband heterodyne detection set-up.

and the LO power into a single beam. It is designed to combine beams with negligible loss and suppress any LO noise within the sidebands [3,4]. Appendix E gives a detailed description of the diplexers. The objective lens focuses the beam through the silicon substrate lens onto the bow-tie antenna at the focal plane.

The LO power is generated by a klystron and can be adjusted by the attenuator. 91 GHz is chosen as the LO frequency. The IF power is generated by the Schottky diode located at the apex of the bow-tie antenna. A low-noise IF amplifier chain amplifies the IF power so that it can be measured by the HP 435B power meter. Fig. 6.2a is a photograph of the low-noise IF amplifier chain. It has a 1.4 GHz center frequency and a 200 MHz bandwidth. Its circuit diagram is shown in Fig. 6.2b.

The mixer conversion loss and noise temperature are determined from hot and cold load measurements [5]. Appendix F gives a detailed description of the measurements. For convenience, microwave absorber (ECCOSORB CV3) at room temperature serves as hot load. The cold load is the same absorber soaked in liquid nitrogen in a styrofoam box and reflected to the receiver by a metallic mirror. The absorber must cover the whole antenna beamwidth to get an accurate measurement. The mixer conversion loss L_M and the mixer noise temperature T_M are calculated by

$$L_M(dB) = G_{IF}(dB) - G(dB) \tag{6.9}$$

$$T_M = T_R - L_M T_{IF} \tag{6.10}$$

where G and T_R are the gain and the noise temperatures of the entire receiver determined directly from hot and cold measurements, and G_{IF} and T_{IF} are the gain and the noise temperature of the IF amplifier chain (measured to be 80 dB and 106°K, respectively). Since the noise from black body radiation is broad band

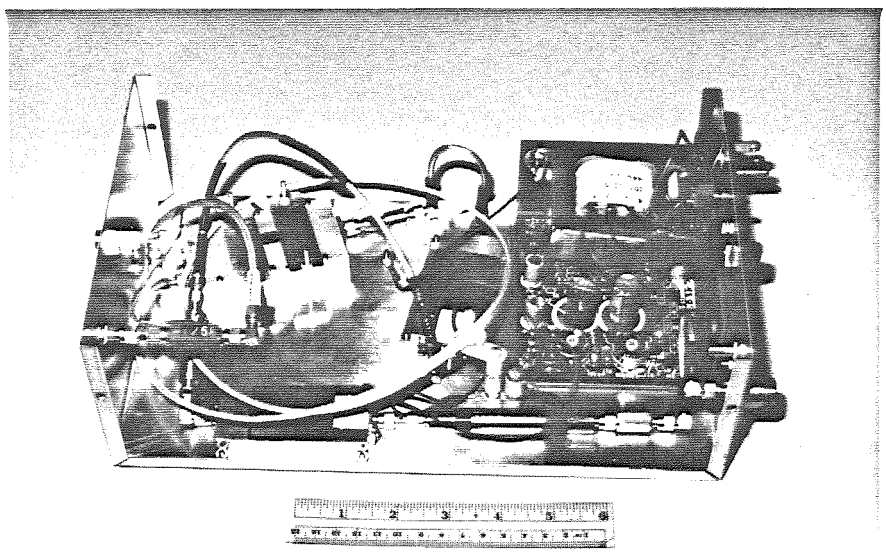

Fig. 6.2a. Photograph of low noise IF amplifier chain with 80 dB gain and 106°K noise temperature.

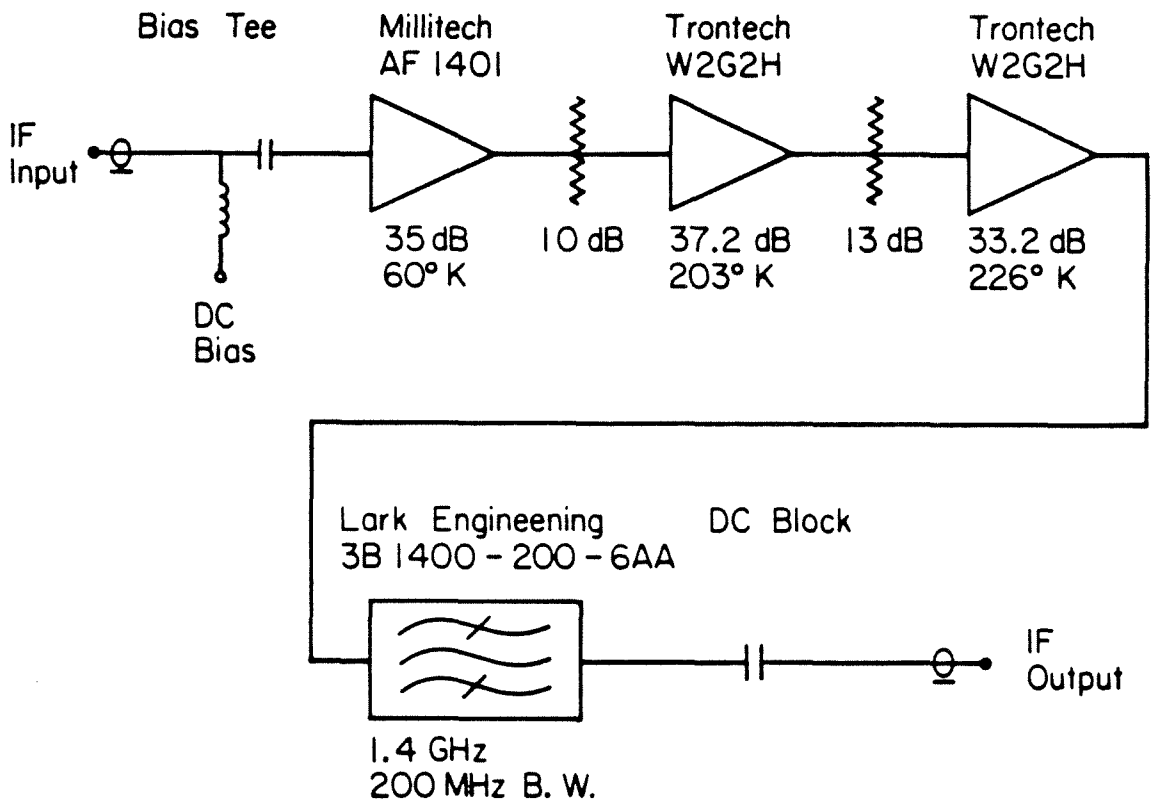

Fig. 6.2b. Circuit diagram. The gain and the noise temperature of each amplifier from specification are written below each amplifier.

and is accepted by the receiver at both signal and image frequencies, double-side band mixer conversion loss and noise temperature are obtained in this way.

We also did single-sideband heterodyne detection measurements as shown in Fig. 6.3. The 94 GHz signal generated by a Gunn diode is the upper sideband signal of the 91 GHz LO. The 3 GHz IF signal is amplified by a low noise IF amplifier (Avantek AFT-4233) with 39 dB gain and 3.15 dB noise figure. The amplifier is calibrated by a HP 8970 noise figure meter.

Since the barrier height of the Al-GaAs Schottky diode is quite high (0.755 eV), a DC bias is provided to reduce the LO power requirement. The effect of the bias voltage is to make the conversion loss at a reduced local-oscillator power almost as good as that at the normal power level. Since the LO noise within sidebands are proportionally reduced, an improvement in overall noise temperature often results [6].

6.3. Double-Sideband Results

Fig. 6.4 shows double-sideband mixer conversion loss and noise temperature versus LO power. Both conversion loss and noise temperature go down when LO power increases. A DSB mixer conversion loss of 11.2 dB and noise temperature of 3770°K have been achieved with a LO power of 9 dBm. This conversion loss is divided into the system coupling efficiency, the instrinsic conversion loss, the RF and IF impedance mismatch, series resistance losses, and the parasitic loss. The system coupling efficiency is 6.2 dB inferred from video detection measurements in Chap. 5. The intrinsic conversion loss is 0.9 dB for a broadband double-sideband mixer [7]. The RF and IF mismatch losses have been estimated by D. P. Kasilingam from a computer program provided by Kerr and Siegel [8]. The calculated RF impedance is $80 - j36\ \Omega$, giving an RF mismatch loss of 0.2 dB

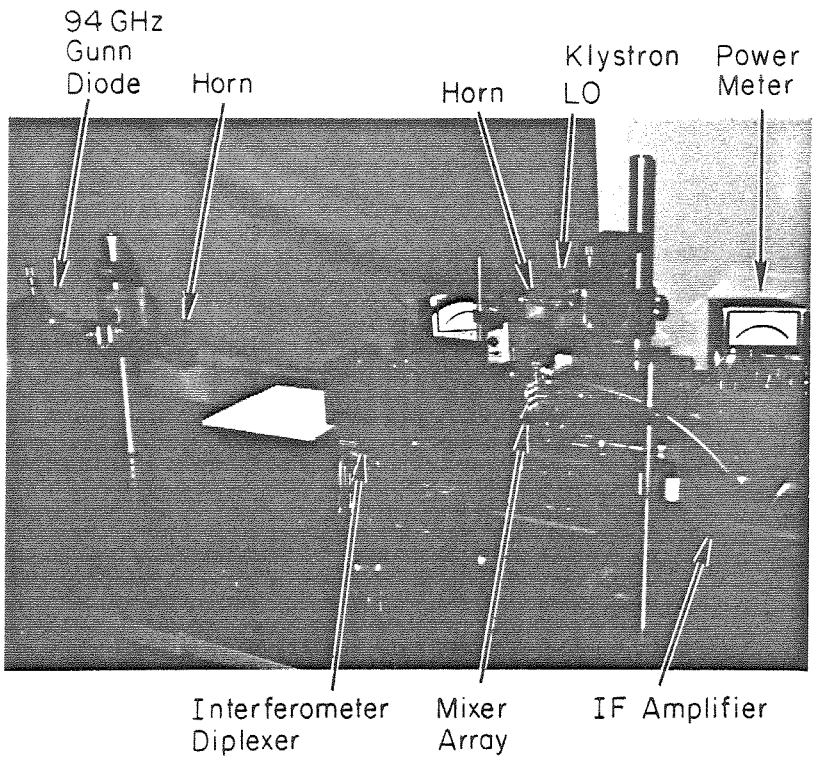

Fig. 6.3a. Photograph of single-sideband heterodyne detection set-up.

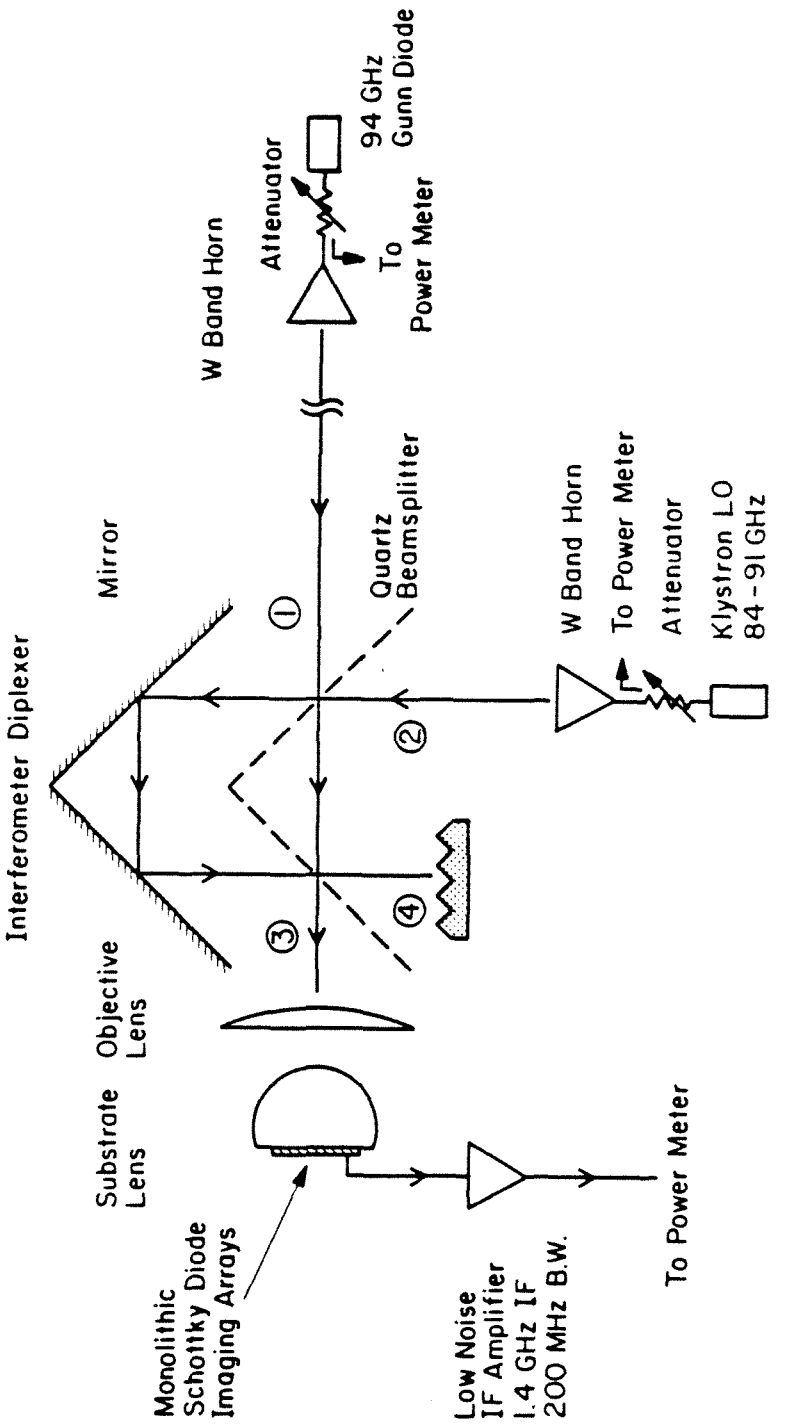

Fig. 6.3b. Schematic drawing of single-sideband heterodyne detection set-up.

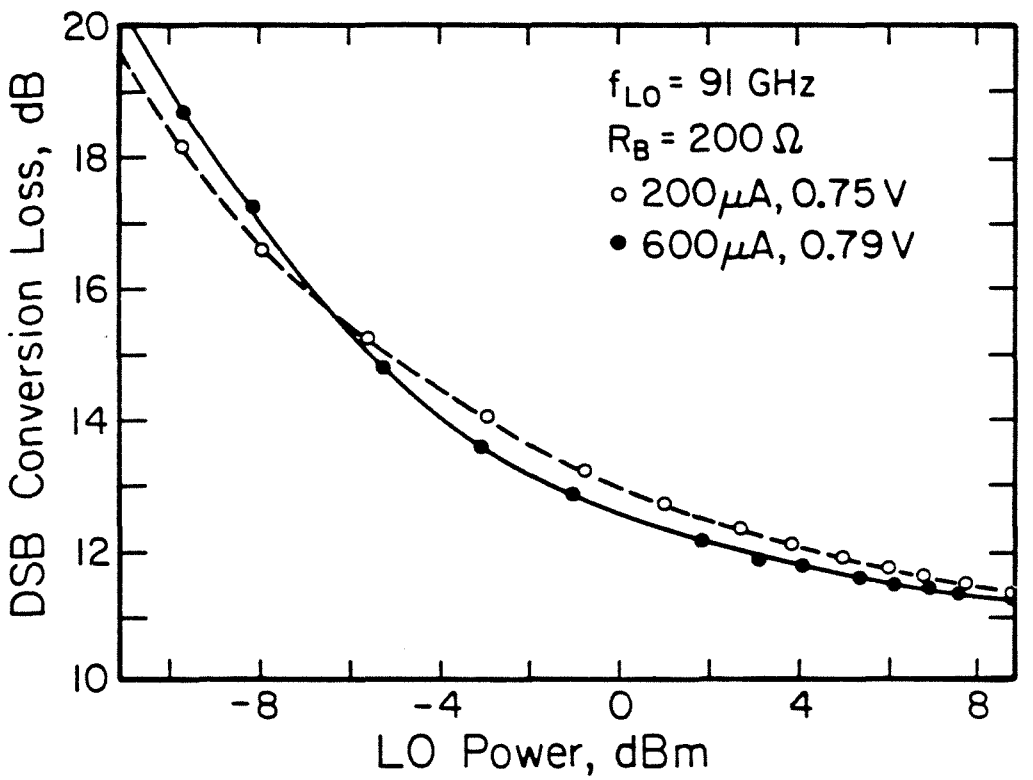

Fig. 6.4a. Double-sideband mixer conversion loss versus LO, with 200 Ω bias resistance. (200 μA, 0.75 V) and (600 μA, 0.79 V) are two DC bias conditions when there is no LO power input.

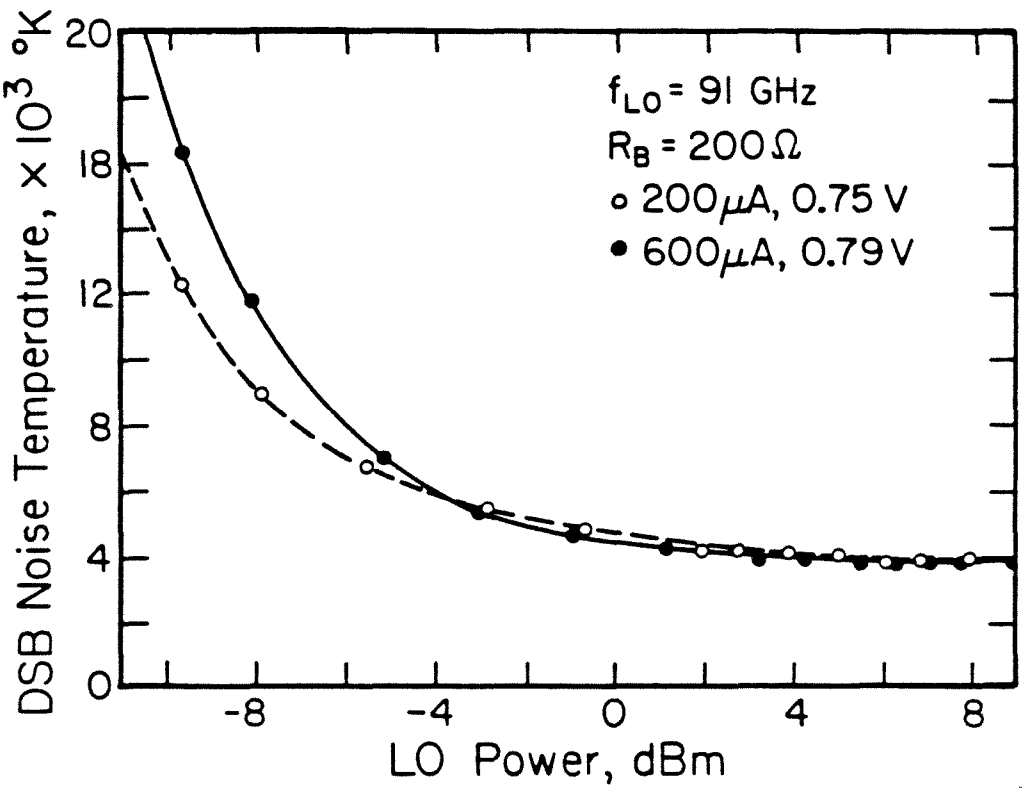

Fig. 6.4b. Double-sideband mixer noise temperature versus LO power with 200 Ω bias resistance. (200 μA, 0.75 V) and (600 μA, 0.79 V) are two DC bias conditions measured across the Schottky diode when there is no LO power input.

and a series resistance loss of 1 dB. The calculated IF impedance is 150 Ω, giving an IF mismatch loss of 1.2 dB and series resistance loss of 0.5 dB. The remaining loss is 1.2 dB which is mainly due to bond wires and IF connections. Table 6.1 gives the complete conversion loss breakdown. The mixer noise temperature is larger than the shot noise partly because of the thermal noise generated by the series resistance [2].

Table 6.1. The detailed breakdown of DSB conversion loss

System coupling efficiency	6.2 dB
Intrinsic conversion loss	0.9 dB
RF mismatch	0.2 dB
IF mismatch	1.2 dB
RF series resistance loss	1.0 dB
IF series resistance loss	0.5 dB
Parasitic loss	1.2 dB
DSB mixer conversion loss	11.2 dB

The total receiver noise temperature including IF amplifier noise is 5170°K. If our imaging system is used as a passive total power radiometer, the minimum detectable temperature ΔT_m is 0.37°K calculated by [9]

$$\Delta T_m = \frac{T_R}{\sqrt{B\tau}} \tag{6.11}$$

with a one second integration time τ and 200 MHz instantaneous bandwidth B.

The conversion loss and the noise temperature also depend on the DC bias [6,10]. Fig. 6.4 and 6.5 show the conversion loss and noise temperature versus LO power under two different DC bias conditions, (200 μA, 0.75 V) and (600 μA,

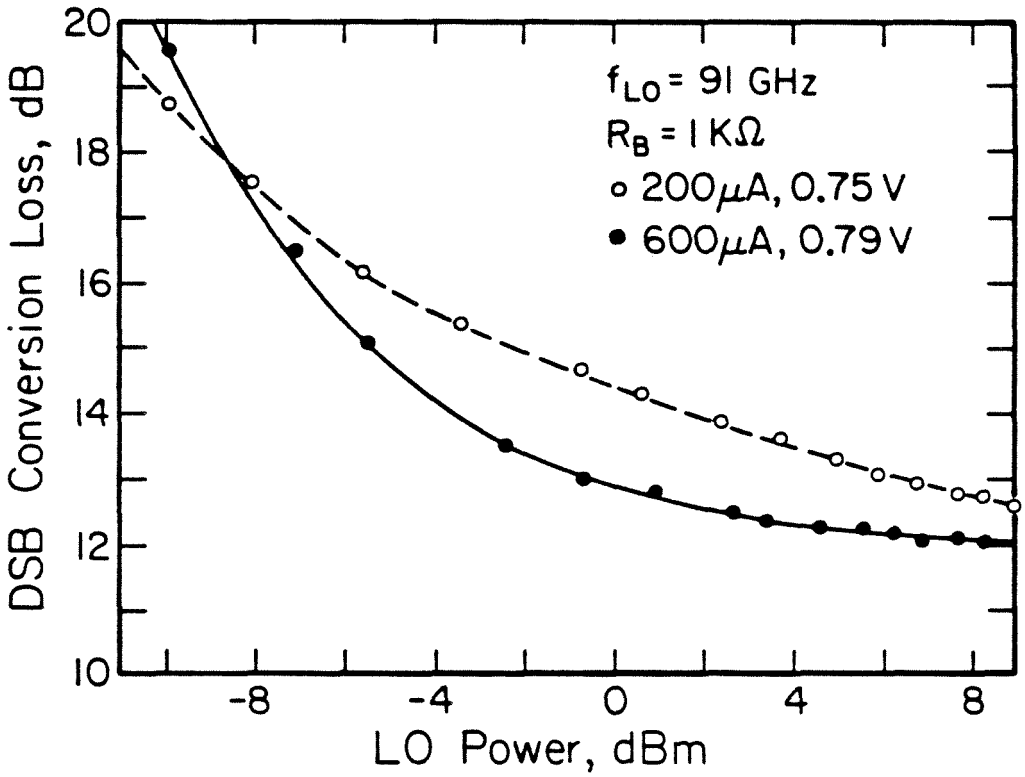

Fig. 6.5a. Double-sideband mixer conversion loss versus LO power with 1 KΩ bias resistance. (200 μA, 0.75 V) and (600 μA, 0.79 V) are two DC bias conditions measured across the Schottky diode when there is no LO power input.

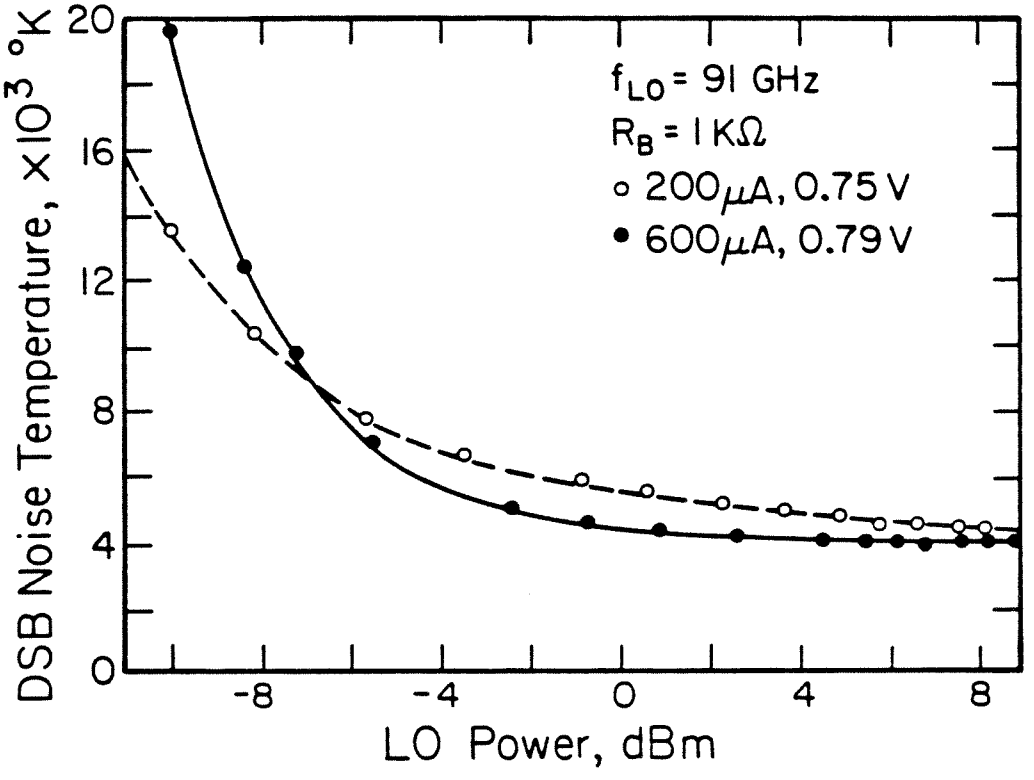

Fig. 6.5b. Double-sideband mixer noise temperature versus LO power with 1 KΩ bias resistance. (200 μA, 0.75 V) and (600 μA, 0.79 V) are two DC bias conditions measured across the Schottky diode when there is no LO power input.

0.79 V). A small DC bias gives better results at low LO power while a large DC bias works better at high LO power. In general, the smallest conversion loss for a particular local oscillator amplitude usually results from the use of a bias voltage that is slightly less than the amplitude of the local oscillator signal [6]. The bias resistance affects the conversion loss and the noise temperature too. Fig. 6.6 shows the current-voltage characteristics of a Schottky diode with and without LO power. Fig. 6.7 shows that the current increases more quickly with LO power for a 200 Ω bias resistance than for 1 KΩ bias resistance. Fig. 6.4 shows little difference in conversion loss and noise temperature between the two initial DC bias conditions with 200 Ω bias resistance at large LO power. On the other hand, Fig. 6.5 shows a large difference between the two initial DC bias conditions with 1 KΩ bias resistance at large LO power. Therefore, the small bias resistance is more suitable for biasing the mixer. From our experience, there is little difference in conversion loss and noise temperature between 100 Ω and 200 Ω bias resistances.

6.4. Single-Sideband Results

Fig. 6.8 shows the single-sideband mixer conversion loss versus LO power. The behavior is similar to the double-sideband conversion loss. The best SSB conversion loss is 14.4 dB which is 3.2 dB higher than the best DSB conversion loss. Although the IF frequency is 3 GHz, instead of 1.4 GHz in DSB detection measurements, these measurements serve as a check on the double-sideband measurements.

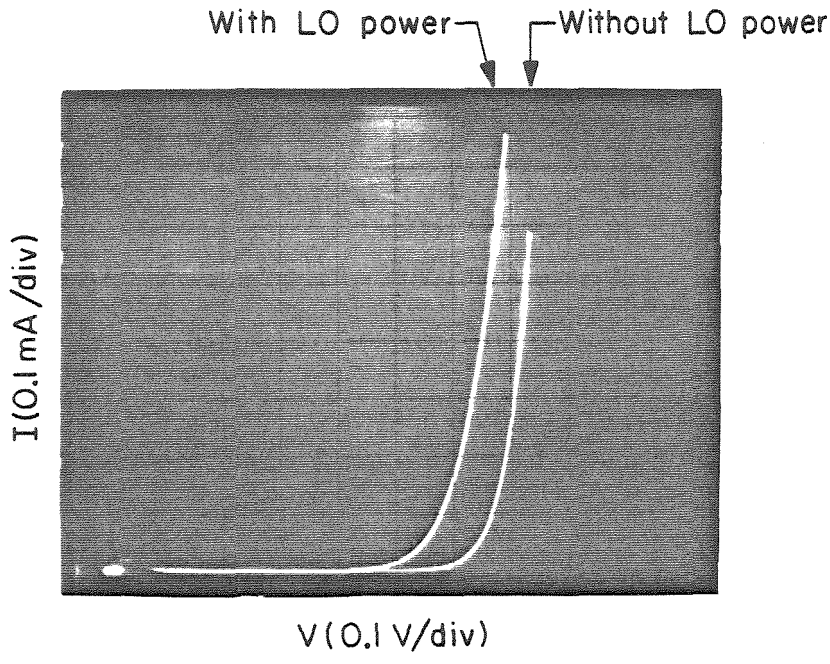

Fig. 6.6. Current-voltage characteristics of a Schottky diode with and without LO power. It was taken from curve tracer.

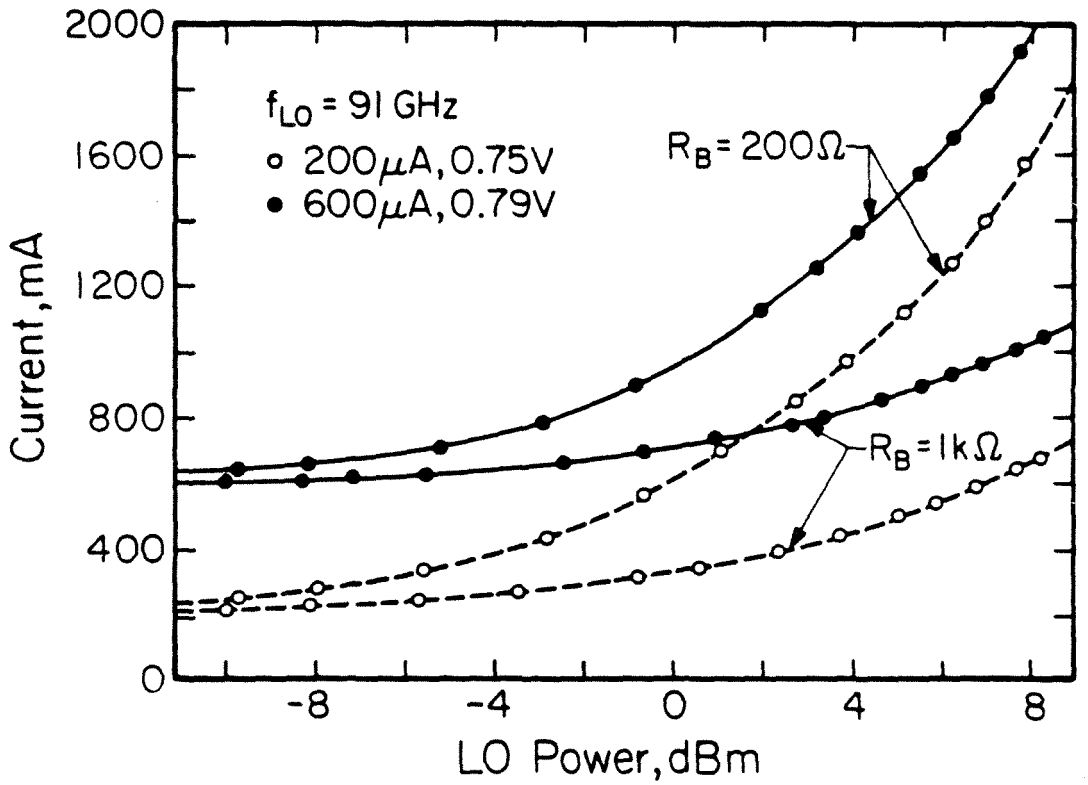

Fig. 6.7. Total diode current versus LO power with 200 Ω and 1 KΩ bias resistances. (200 μA, 0.75 V) and (600 μA, 0.79 V) are the DC bias conditions across the diode when there is no LO power.

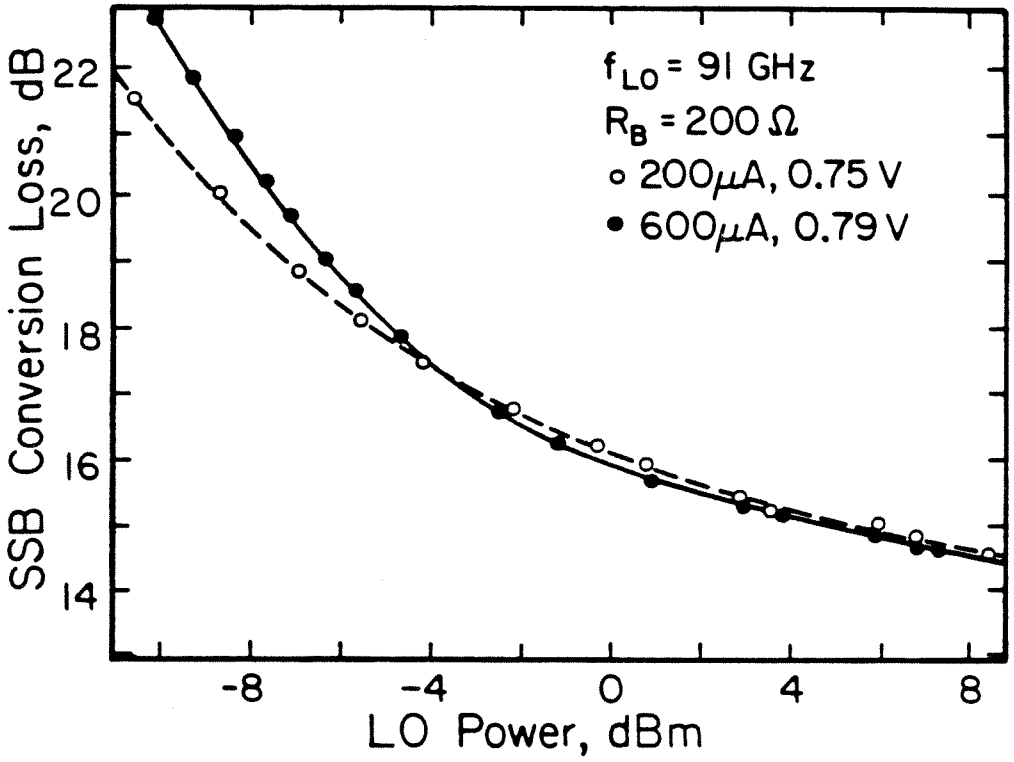

Fig. 6.8a. Single-sideband mixer conversion loss versus LO power with 200 Ω bias resistance. (200 μA, 0.75 V) and (600 μA, 0.79 V) are the DC bias conditions across the diode when there is no LO power.

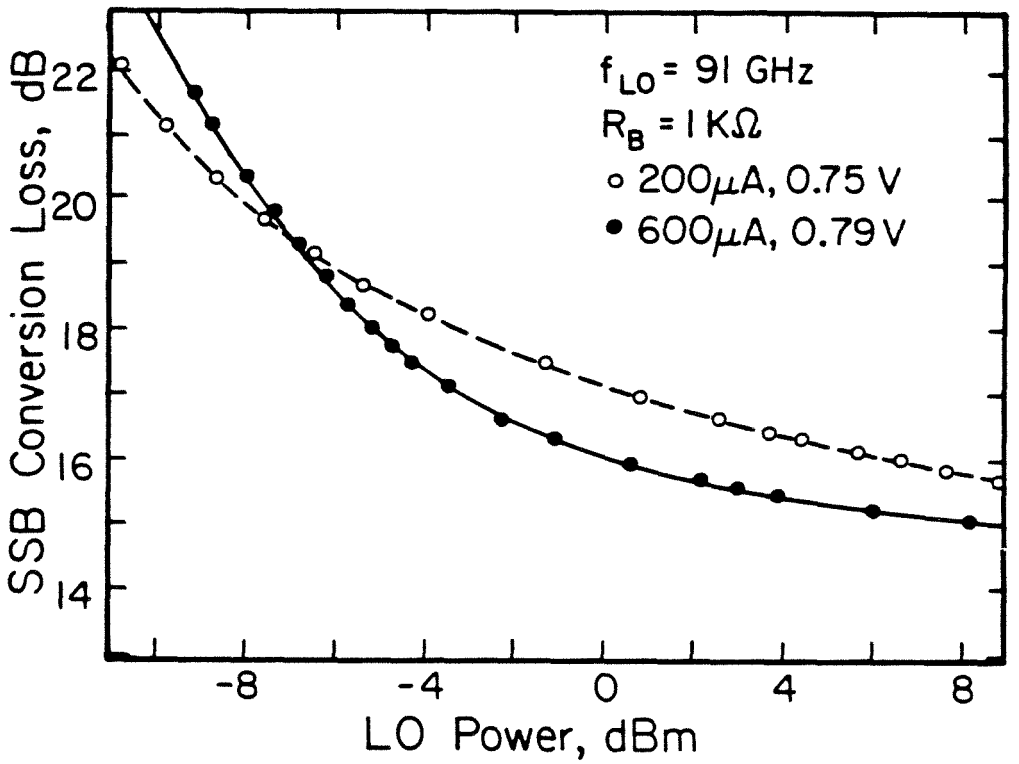

Fig. 6.8b. Single-sideband mixer conversion loss versus LO power with 1 KΩ bias resistance. (200 μA, 0.75 V) and (600 μA, 0.79 V) are the DC bias conditions across the diode when there is no LO power.

References

[1] T. G. Blaney, "Detection Techniques at Short Millimeter and Submillimeter Wavelengths: An Overview," *Infrared and Millimeter Waves*, vol. 3, Chap. 1, pp. 1–75, K. J. Button, ed., Academic Press, New York, 1980.

[2] M. V. Schneider, "Metal-Semiconductor Junction as Frequency Converters," *Infrared and Millimeter Waves*, vol. 6, Chap. 4, pp. 209–275, K. J. Button, ed., Academic Press, New York, 1983.

[3] Perry Miles, "High Efficiency Optical Diplexers", *Applied Optics*, vol. 21, No. 8, pp. 1367–1372, Apr. 1982.

[4] P. F. Goldsmith, "Quasi-Optical Techniques at Millimeter and Submillimeter Wavelengths," *Infrared and Millimeter Waves*, vol. 6, Chap. 5, pp. 277-343, K. J. Button, ed., Academic Press, New York, 1983.

[5] Bernd Vowinkd, "Simplified Receiver Response Measurement," *Microwave & RF*, pp. 147–148, Mar. 1984.

[6] R. V. Pound, *Microwave Mixers*, Chap. 5, sec. 7, pp. 249–256, McGraw-Hill Book Company, Inc., 1948.

[7] A. J. Kelly, "Fundamental Limits on Conversion Loss of Double Sideband Resistive Mixers," *IEEE*, vol. MTT–25, pp. 867–869, Nov. 1977.

[8] P. H. Siegel, A. R. Kerr and W. Hwang, "Topics in the Optimization of Millimeter-Wave Mixers," *NASA Technical paper 2287*, Mar. 1984.

[9] P. Bhartia and I. J. Bahl, "Millimeter Wave Applications and System," *Millimeter Wave Engineering and Application*, Chap. 10, pp. 617–682, John Wiley & Sons, Inc., 1984.

[10] W. Hant, "Short Millimeter Wavelength Mixer with Low Local Oscillator

Power," *IEEE*, vol. MTT-33, No. 2, pp. 135–142, Feb. 1985.

Chapter 7

Future Work in Millimeter-Wave Imaging Arrays

In this thesis, efficiencies of elementary integrated-circuit feed antennas have been discussed. The calculated results do show that the antennas with substrate lenses are potentially better feeds than those without substrate lenses. A polystyrene cap was made and demonstrated to be an effective matching layer for a silicon lens. This makes a monolithic circuit with a gallium-arsenide substrate and a silicon lens much more attractive than before. The planar Schottky diodes were integrated with bow-tie antennas to form a one dimensional imaging array. A self-aligning process and proton isolation have been developed to make these diodes with a 1.1-THz zero-bias cutoff frequency. We also studied the antenna coupling efficiency and imaging properties of the system by video detection at 94 GHz. As a heterodyne receiver, a DSB mixer conversion loss of 11.2 dB and noise temperature of 3770°K have been achieved at 91 GHz. There are several interesting areas where we can further improve our millimeter wave imaging array and find applications for it.

The first is in integrating zero-bias diodes with antennas to form a large imaging array. Since the normal Schottky-barrier height of n-type GaAs is about 0.8 eV, a DC bias is required to obtain the optimum detector sensitivity. The zero-bias diode is highly desirable for a large array application, since the biasing circuit for each detector can be eliminated. In addition, the low-barrier height diode needs less local oscillator power. This is particularly important in arrays. The Schottky-barrier height can be reduced by introducing a very thin, but heavily doped n^+ layer near the metal/GaAs interface [1]. The reduced barrier is due to field-enhanced tunneling. This thin interface layer can be grown by molecular beam epitaxy [2,3], or formed by a gold-germanium alloy [4,5]. The Gap diode

is another promising low turn-on voltage GaAs diode whose I–V characteristic is controlled by a geometric gap between adjacent Schottky barrier regions [6]. The turn-on voltage of the diode is determined by the overlap of depletion widths of Schottky metals on both sides of the gap.

The second interesting area is the harmonic mixing. Due to the lack of powerful solid-state oscillators and difficulties with tube oscillators, harmonic mixing becomes attractive when the frequency is over 100 GHz. It may be the only way to provide enough local oscillator power to each individual mixer in a large heterodyne imaging array. For second-harmonic mixing, low conversion loss and noise temperature can be expected with antiparallel diode pairs [7] or planar doped barrier (PDB) diodes [8], since the symmetric I–V characteristic of these diodes suppresses the fundamental mixing and local oscillator noise sidebands. It is much easier to make a matched diode pair in a monolithic circuit than a hybrid circuit. The PDB diode is a majority carrier device with an n^+-i-p^+-i-n^+ doping configuration in which an extremely thin, fully depleted acceptor layer (20–100 Å) is used to form a triangular potential profile of predetermined shape and height [9].

The third is real-time heterodyne imaging with the array we have built. An array with n detectors should allow each detector to have n times as much integration time as a single detector system allows in doing imaging. It can be applied to image fast changing objects such as plasma density in fusion research or the weak signals in radioastronomy.

References

[1] J. M. Shannon, "Control of Schottky Barrier Height Using Highly Doped Surface Layers," *Solid-State Electronics*, vol. 19, pp. 537–543, 1976.

[2] K. Shenai et al., "Field-Enhanced Tunneling and Barrier Lowing in Al-n^+GaAs-n GaAs Schottky Contacts Grown by MBE," vol. EDL–5, No. 8, pp. 329–332.

[3] S. J. Eglash et al., "Barrier Heights from Ohmic to Boundgap: Modified Al: GaAs Schottky Diode by MBE," *IEDM Tech. Dig.*, pp. 119–122, Dec. 1983.

[4] W. J. Moroney and Y. Anand, "Low Barrier Height Gallium Arsenide Microwave Schottky Diodes Using Gold-Germanium Alloy," *Symp. on GaAs*, paper 31, pp. 259–267.

[5] C. C. Chang et al., "A Zero-Bias GaAs Millimeter Wave Integrated Detector Circuit," *IEEE MTT-S Digest*, pp. 206–208, 1982.

[6] S. J. J. Teng, "The Gap Diode: A New High Frequency Mixer and Detector," *IEEE MTT-S Digest*, C–1, pp. 24–26, 1982.

[7] E. R. Carlson et al., "Subharmonically Pumped Millimeter-Wave Mixers," *IEEE* vol. MTT–26, pp. 706–715, Oct. 1978.

[8] S. Dixon, T. R. AuCoin and R. L. Ross, "60 GHz Planar Doped Barrier Subharmonic Mixer," *8th Int. Conf. on Infrared and Millimeter Waves*, T 6.9, 1983.

[9] R. J. Malik et al., "Rectifying, Variable Planar-Doped-Barrier Structure in GaAs," *Inst. Phys. Conf. Ser.*, No . 56, Chap. 9, pp. 697–710, 1980.

Appendix A

Fabrication Process for Monolithic Schottky Diode Imaging Arrays

The following procedures are used for fabricating Monolithic Schottky diode imaging arrays on semi-insulating GaAs substrate.

Fabrication Process

1. Put down epitaxial layers and in situ aluminum by molecular beam epitaxy (MBE).

   1.4 μm n^+ layer with 3×10^{18} cm^{-3} doping concentration.

   0.1 μm n layer with 10^{17} cm^{-3} doping concentration.

   0.2 μm in situ aluminum.

   (This was done by J. S. Smith in Prof. Yariv's group).

2. Remove indium from backside of the wafer by lapping with 5 μm Al_2O_3 power bought from Buehler; otherwise indium makes wafer uneven and hard to hold by vacuum.

3. Form aluminum bows and leads on upper half plane of the wafer.

   a. Pattern photoresist for etching.

      photoresist : AZ 1350J

      spin speed : 4000 rpm

      prebake : 85°C, 25 min.

      exposure : 25 sec.

      development : 30–60 sec. (shake in AZ or microposit

developer mixed with water in one to one ratio)

Postbake : 120°C, 5 min.

b. Etch aluminum by aluminum etchant–Type D bought from Transene Company, Inc.. The etch rate is 200 Å/sec at 50°C. Shake and watch the sample during etching. Take out the sample and put into DI water immediately after the pattern shows up clearly.

4. Form Schottky electrode and the other half of bow-tie as well as lead on lower half plane of the wafer.

a. Pattern photoresist for lift off

It is the same procedure as 3a. except that the spin speed changes to 3000 rpm to obtain a thicker photoresist which makes photoresist easily lift off.

b. Etch aluminum to form Schottky electrode.

It is the same procedure as 3b.

c. Remove *n* layer in the ohmic contact area to have good ohmic contact by one of the following etchants [1] under constant stirring and room temperature.

etchant	etch rate
$H_2SO_4 : H_2O_2 : H_2O$	
1 : 8 : 160	0.26 μm/min
1 : 8 : 8	4.5 μm/min

d. Evaporate AuGe/Ni/Au (300 Å/200 Å/2000 Å) consecutively within the vacuum evaporator under pressure below 3×10^{-6} torr. (AuGe (88%/12%) evaporation slugs ($\frac{1}{8}$" diameter $\times \frac{1}{8}$") were bought from

Metron Inc..)

e. Lift off unwanted metal by dissolving the photoresist in acetone. If the edges of the sample were not cover by the metal, acetone would go under the metal faster and lift off would be much easier. It is done by blocking the unwanted metal by aluminum foil during the evaporation.

5. Alloy ohmic contact at 430°C for 30 sec. in H_2 ambient. The rising and falling time of substrate temperature should be short to get a good ohmic contact [2].

6. Form proton isolation mask by thick photoresist. In order to block the proton with 320 KeV, it need to be at least 3.5 μm.

photoresist :	AZ 1375	AZ 4620
spin speed :	3000 rpm	4000 rpm
prebake :	85°C, 25 min	85°, 1 hr.
exposure :	1.5 min.	1.5 min.
development :	3.5 min.	3.5 min.
flood exposure :	5 min.	5min.

Don't use AZ 400 K developer since it will attack aluminum. Don't postbake photoresist; otherwise its edge will be rounded and it will be very hard to strip off after proton bombardment.

7. Implant protons in two consecutive steps

320 KeV with 5×10^{14} cm^{-2} dose

200 KeV with 3×10^{14} cm^{-2} dose

(This was done by Frank So and Ali Ghaffari in Prof. Nicolet's group.)

8. Remove the proton isolation mask by agitating in hot acetone.

The procedures listed above can be used as references and might change later on. For example, the exposure time depends on the UV light intensity and the thickness of photoresist. A good reference book for GaAs fabrication process can be found in [3].

Diagnosis

The Nikon microscope with 1000X is a convenient tool for diagnosis during fabrication. The thickness of an epitaxial layer can be estimated under microscope with filar eyepiece as shown in Fig. A.1. It is done by cleaving the wafer and then staining it by $HF/HNO_3/H_2O$ (1 : 3 :4) for 30 sec.. A photoresist is put on top of the wafer before staining to prevent etching down from the top. Fig. A.2 gives the appearances of an alloyed AuGe/Ni/Au contacts under three different alloy conditions. One can judge his alloyed contact by comparing it with Fig. A.2. Only the properly alloyed contact gives low contact resistance. The photoresist profile of the isolation mask as shown in Fig. A.3 can also be examined under microscope after cleaving the wafer.

References

[1] D. W. Shaw, "Localized GaAs Etching with Acid Hydrogen Peroxide Solution," *J. Electrochem. Soc., Solid-State Science and Technology*, pp. 874–880, Apr. 1981.

[2] M. Ogawa, "Alloying Behavior of Ni/Au-Ge films on GaAs," *J. Appl. Phys.*, vol. 51, No. 1, pp. 406–419, 1980.

[3] R. E. Williams, *Gallium Arsenide Processing Techniques*, Artech House, Inc., Dedham, Massachusetts.

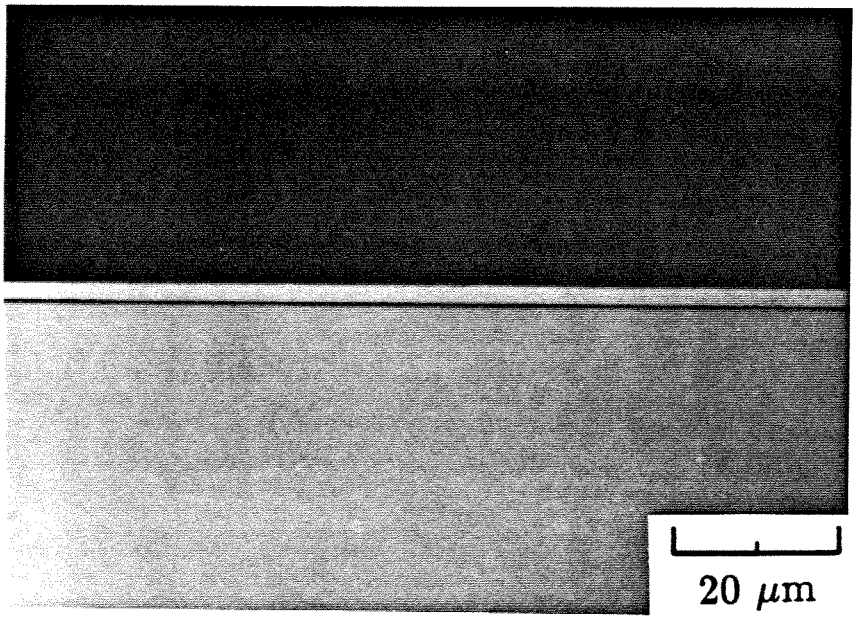

Fig. A.1. Epitaxial layer revealed by staining.

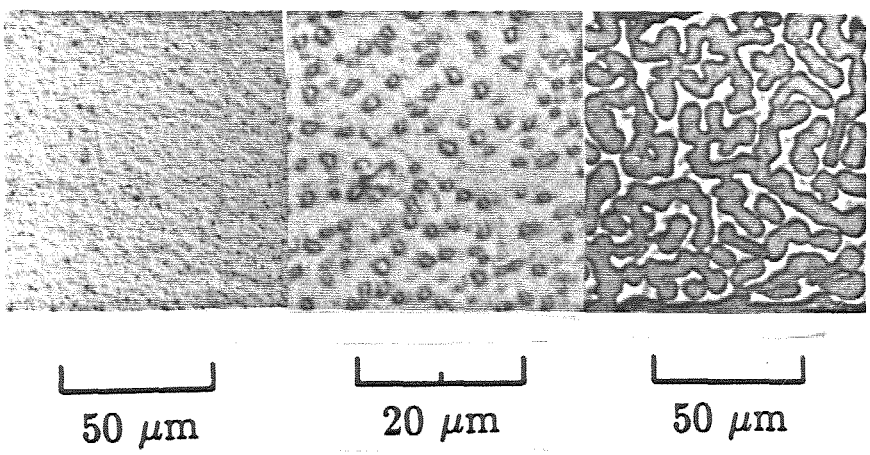

Fig. A.2. Alloyed AuGe/Ni/Au contacts, showing typical pattern if underalloyed (left); alloyed properly (middle); overalloyed (right). The pictures were taken using phase contrast microscopy.

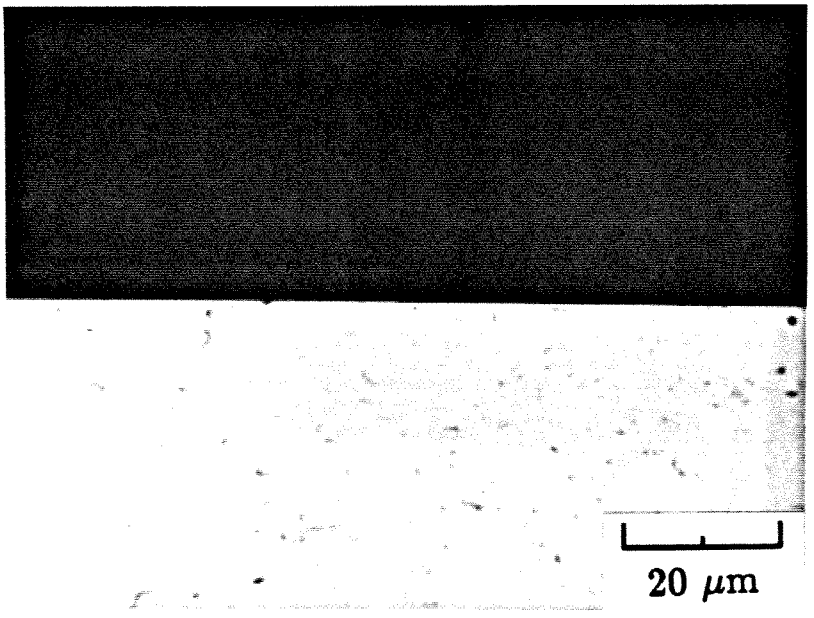

Fig. A.3. Photoresist profile. It is about 5 μm thick with steep edge.

Appendix B

Curve Fitting for the Measured I–V Characteristics of Schottky Diodes

The I–V characteristic of a Schottky diode is given by

$$I = I_S \{\exp[(V - IR_S)/nV_T] - 1\} \qquad (B.1)$$

$$V_T = \frac{kT}{q} \qquad (B.2)$$

where

I_S: reverse saturation current,

R_S: series resistance,

n: ideality factor,

q: electronic charge (1.602×10^{-19} Coul),

k: Boltzmann constant (1.38×10^{-23} J/K), and

T: temperature.

If the Schottky diode is used as a mixer, the loss due to series resistance degrades the conversion loss and increases the noise temperature [1,2]. The shot noise of the Schottky diode is proportional to the ideality factor [3]. Therefore, it is desirable to make the Schottky diode with R_S close to zero and n close to 1.

A method has been developed to determine those parameters of our Schottky diode from the measured I–V characteristic. Under forward bias, Eq. (B.1) can be written as

$$I = I_S \exp[(V - IR_S)/nV_T] \qquad V - IR_S \gg nV_T \qquad (B.3)$$

By taking natural logarithm of Eq. (B.3) and then differentiating it, one obtains a relation without I_S as follows:

$$\frac{dV}{d\ln I} = nV_T + IR_S \qquad (B.4)$$

We can approximate the differentiation by the difference of the consecutive measured data.

$$\frac{dV}{d\ln I}(i) = \frac{V(i+1) - V(i)}{\ln I(i+1) - \ln I(i)} = Y(i) \qquad i = 1, 2, 3, \cdots, N-1 \qquad (B.5)$$

where $V(i)$ and $I(i)$ represent one measured voltage and current pair across the Schottky diode for each i and N is the number of measurements. Eq. (B.4) becomes a set of linear equations with two unknown variables n and R_S which can be determined by least mean square fit

$$R_S = \frac{1}{\Delta} \det \begin{vmatrix} \sum I(i)Y(i) & \sum I(i) \\ \sum Y(i) & N \end{vmatrix} \qquad (B.6)$$

$$n = \frac{1}{V_T \Delta} \det \begin{vmatrix} \sum I^2(i) & \sum I(i)Y(i) \\ \sum I(i) & \sum Y(i) \end{vmatrix} \qquad (B.7)$$

$$\Delta = \det \begin{vmatrix} \sum I^2(i) & \sum I(i) \\ \sum I(i) & N \end{vmatrix} \qquad (B.8)$$

By substituting R_S, n, and the measured I-V data back into Eq. (B.3), I_S can be found as

$$I_S = \exp\left\{ \frac{1}{N} \sum_{i=1}^{N} \left[\ln I(i) - \frac{1}{nV_T}(V - IR_S) \right] \right\} \qquad (B.9)$$

For a room temperature Schottky diode, the diode current is mainly due to thermal emission. The reverse saturation current I_S is given by [4]

$$I_0 = aA^*T^2 \exp\left(-\Phi_{Bn}/V_t\right) \qquad (B.10)$$

where a is the diode area, A^* is effective Richardson constant (0.068$\times$ 120 A/cm^2/K^2 for GaAs at low fields), and Φ_{Bn} is the barrier height of metal-semiconductor barrier which can be calculated from Eq. (B.10), once I_S is found from Eq. (B.9) and a is measured under microscope.

The above formulas have been programmed into an IBM PC. After each fabrication, the computer calculates R_S, n, I_S and Φ_{Bn} from the measured I–V characteristic of the Schottky diode, plots the forward I–V characteristic in semi-log scale by substituting those parameters in Eq. (B.1), and also locates the measured data along the curve for checking as shown in Fig. B.1. One can see the curve fits experimental data quite well. R_S, n, I_S and Φ_{Bn} will be used to calculate the system video responsivity in Chapter 4.

References

[1] W. M. Kelly, "Optimization of Schottky-Barrier Diodes for Low-Noise, Low-Conversion Loss Operation at Near-Millimeter Wavelengths," *Infrared and Millimeter Waves*, vol. 3, Chap. 2, pp. 77–111, K. J. Button, ed., Academic Press, New York, 1980.

[2] M. V. Schneider, "Metal-Semiconductor Junction as Frequency Converters," *Infrared and Millimeter Waves*, vol. 6, Chap. 4, pp. 209–275, K. J. Button, ed., Academic Press, New York, 1983.

[3] A. R. Kerr, "Shot-Noise in Resistive-Diode Mixers and the Attenuator Noise Model," *IEEE*, vol. MTT–27, pp. 135–140, Feb. 1979.

[4] S. M. Sze, *Physical of Semiconductor Devices*, 2nd ed., Chap 5, pp. 245–311, John Wiley & Sons, Inc., New York, 1981.

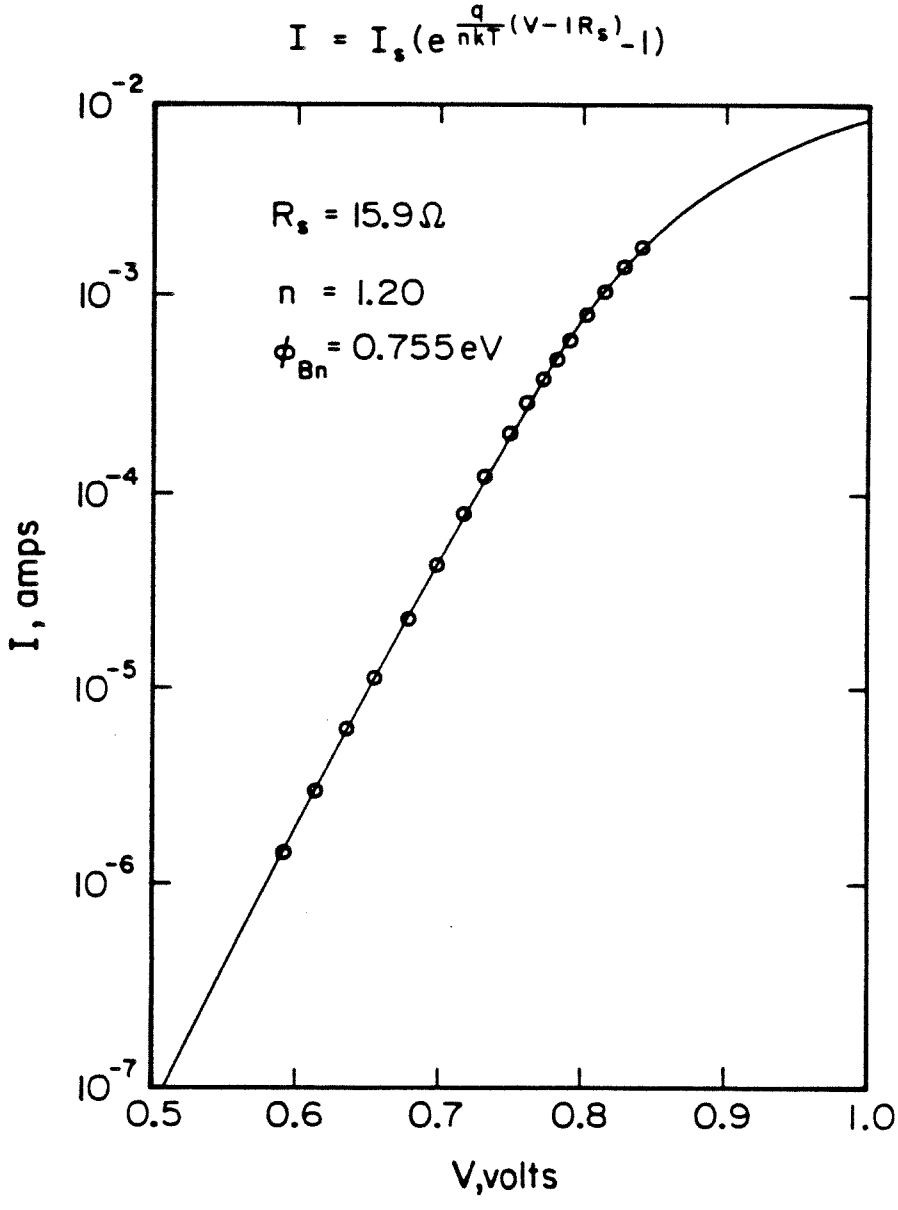

Fig. B.1. I–V characteristic of our Schottky diode. The solid line is obtained by fitting the experimental data in circles to Eq. (B.1).

Appendix C

Theoretical Series Resistance and Capacitance of the Planar Schottky Diode

In order to help us design the planar Schottky diode before fabrication and compare to the experimental results later on, series resistance and capacitance have been calculated analytically from the geometry of the diode and the doping concentration of epitaxial layers. Fig. C.1 shows the schematic drawings of our planar Schottky diode. All the dimensions of the diode are listed in Table C.1 & C.2. Table C.2 also gives electrical properties of epitaxial layers and metal layers. The mobility of the n and n^+ layers is calculated by [1]

$$\mu = \frac{10^4}{\left[1 + \left(\frac{N}{5\times10^{16}}\right)^{0.25}\right]} \qquad (C.1)$$

The skin depth is given by [2]

$$\delta(\text{cm}) = \frac{1}{2\pi}\left[\frac{\rho(\Omega - \text{cm})}{f(GHz)}\right]^{1/2} \qquad (C.2)$$

Since all the epitaxial thickness and metal thickness are either less than or close to the skin depth over the frequency range we tested our planar Schottky diode (75 GHz–170 GHz), the skin effect can be neglected. Moreover, these frequencies are well below the plasma resonant frequency which is about 1 THz [3]. Series resistance and capacitance should not change with frequency. The analytical formulas for calculating their value are listed below.

Series Resistance

Series resistance can be divided into several components as follows.

—Resistance due to undepleted n layer is given by

$$R_{n1} = \frac{\rho_n(t_n - d)}{W_S L_S} \qquad (C.3)$$

Table C.1. Lateral Dimensions of Our Planar Schottky Diode

L_S : 6 μm	length of the Schottky diode
W_S : 0.8 μm	width of the Schottky diode
g : 1 μm	gap between the Schottky electrode and the ohmic contact
L_1 : 4 μm	distance between the proton isolation boundary and the edge of the ohmic contact
W_1 : 18 μm	apex width of bow-tie antenna on the Schottky metal side
W_2 : 54 μm	apex width of bow-tie antenna on the ohmic contact side
W_3 : 508 μm	width of the low frequency lead
L_3 : 0.3 cm	length of the low frequency lead

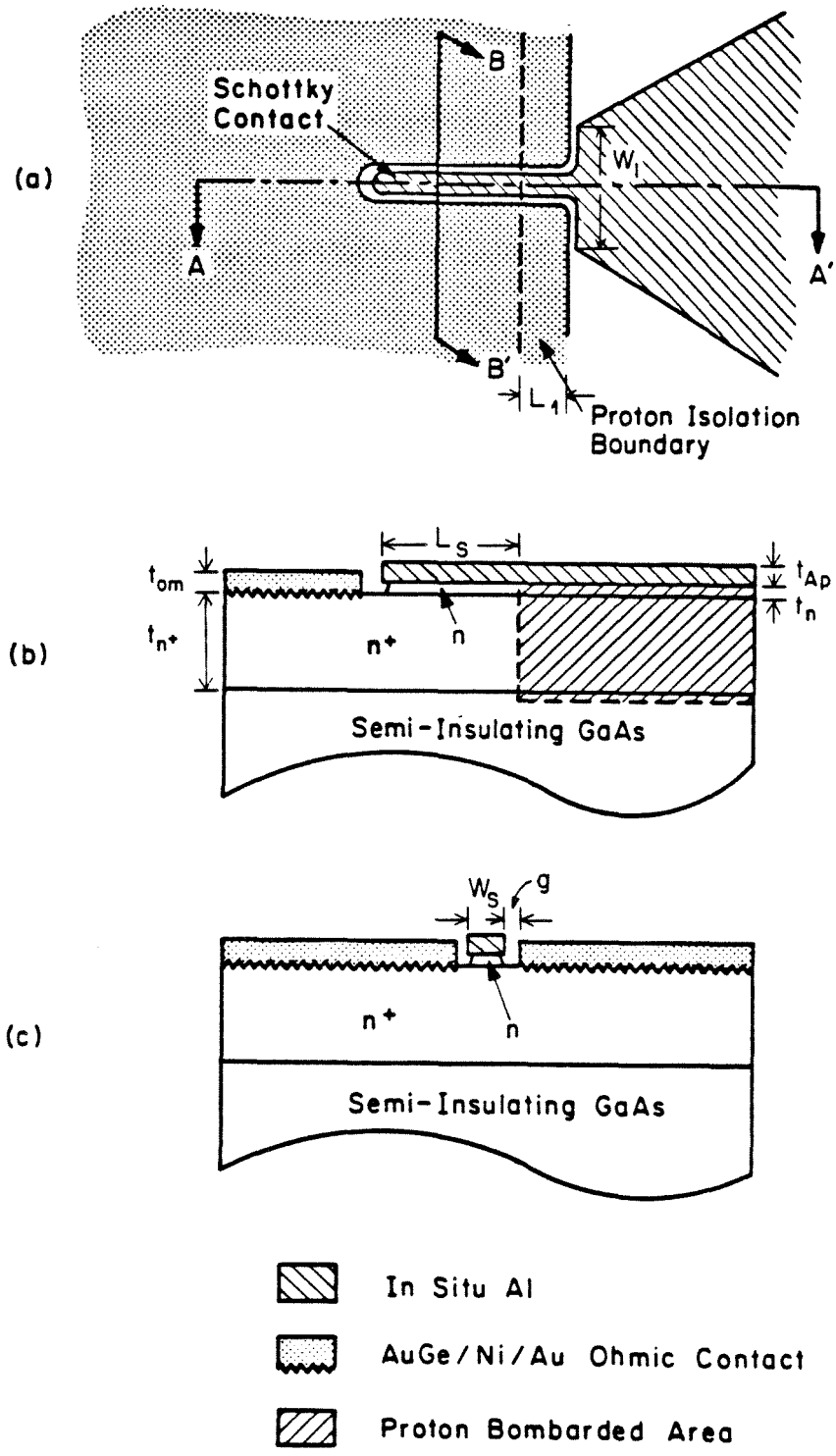

Fig. C.1. Schematic drawings of our planar Schottky diode. (a) top view, (b) A-A' section view, and (c) B-B' section view. All the dimensions are listed in Table I & II.

Table C.2. Thickness and Electrical Properties of Epitaxial Layers and Metal Layers

	n	n^+	Al	AuGe/Ni/Au
t (μm)	0.1	1.4	0.2	0.03/0.02/0.2
N (cm^{-3})	10^{17}	1.5×10^{18} *		
μ (cm^2/V-s)	4570	2990		
ρ (Ω-cm)	1.37×10^{-1}	1.36×10^{-3}	2.74×10^{-6}	2.20×10^{-6} ***
			(4.57×10^{-6}) **	(3.67×10^{-6}) **
$\rho_\square$ (Ω)		9.71	0.137	0.11 ***
			(0.229)	(0.184)
δ (μm)	1.94	6.05	0.272	0.243 ***
			(0.351)	(0.314)

t : thickness

N : doping concentration

μ : mobility

ρ : resistivity

$\rho_\square$: sheet resistance

δ : skin depth at 94 GHz

n, n^+ : epitaxial layers

Al : Schottky metal (aluminum)

AuGe/Ni/Au : ohmic contact metal

* : estimated from ρ_{n^+} determined by contact resistivity measurement using linear transmission line model

** : thin film value = $\frac{5}{3}\times$ bulk value listed above

*** : for gold (Au) only

where d is the depletion width.

—Spreading resistance found by conformal mapping [3,4,5] is given by

$$R_{n2} = \frac{\rho_{n^+}}{2\pi r} \tan^{-1}\left[\frac{t_{n^+}}{r}\right] \times \frac{2(L_S + W_S)}{2L_S + W_S} \tag{C.4}$$

where

$$r = \frac{L_S + W_S}{2K(k_2)} \tag{C.5}$$

$$k_2 = \frac{L_S - W_S}{L_S + W_S} \tag{C.6}$$

and $K(k)$ is the complete elliptic integral with modulus k.

—Resistance due to the gap between the Schottky electrode and the ohmic contact is given by

$$R_{n3} = \frac{\rho_{n^+}}{2\pi t_{n^+}} \ln\left[\frac{r'}{\sqrt{r^2 + t_n^2}}\right] \times \frac{2(L_S + W_S + 2g)}{2L_S + W_S + 2g} \tag{C.7}$$

where

$$r' = \frac{L_S + W_S + 4g}{2K(k_3)} \tag{C.8}$$

$$k_3 = \frac{L_S - W_S}{L_S + W_S + 4g} \tag{C.9}$$

—Ohmic contact resistance calculated by transmission line model [6,7] is given by

$$R_C = Z \coth\left(\alpha(W_2 - W_S - 2g)/2\right) \tag{C.10}$$

where

$$Z = \frac{\sqrt{\rho_{n^+}\rho_C / t_{n^+}}}{2L_S + W_S + 4g} \tag{C.11}$$

$$\alpha = \sqrt{\rho_{n^+}/(\rho_C t_{n^+})} \tag{C.12}$$

and ρ_C is the contact resistivity ($\approx 5 \times 10^{-6}\ \Omega\text{-cm}^2$ for our sample).

—Resistance due to Schottky electrode (the stripe) is given by

$$R_{A0} = \frac{\rho_{Al}(0.5L_S + L_1)}{L_S W_S} \tag{C.13}$$

—Resistance due to bow-tie antenna on the aluminum side is given by

$$R_{A1} = \frac{\rho_{Al}}{2t_{Al}\tan 30^\circ} \ln\left|\frac{W_3}{W_1}\right| \qquad (C.14)$$

—Aluminum lead resistance is given by

$$R_{A2} = \frac{\rho_{Al} L_3}{t_{Al} W_3} \qquad (C.15)$$

—Resistance due to bow-tie antenna on the ohmic contact side is given by

$$R_{O1} = \frac{\rho_{om}}{2t_{om}\tan 30^\circ} \ln\left|\frac{W_3}{W_2}\right| \qquad (C.16)$$

—Ohmic contact lead resistance is given by

$$R_{O2} = \frac{\rho_{om} L_3}{t_{om} W_3} \qquad (C.17)$$

The total series resistance R_S will be

$$R_S = R_{n1} + R_{n2} + R_{n3} + R_C + R_{A0} + R_{A1} + R_{A2} + R_{O1} + R_{O2} \qquad (C.18)$$

Table C.3 gives the calculated results for each component and total series resistance using dimensions and resistivities in Table C.1 & C.2. The measured series resistance (15.9 Ω) from I–V characteristic of the diode is higher than the theoretical value (13 Ω). The extra resistance might be due to the undepleted n layer introduced by the forward bias during I–V measurement and errors in estimating parameters of our Schottky diode in Table C.1 & C.2. This analysis help us understand where the series resistance comes from. Obviously, the contact resistance is the major contributor and should be reduced by increasing doping and thickness of n^+ layer if possible.

Junction Capacitance and Parasitic Capacitance

The capacitance of the Schottky diode can be separated into junction capacitance whose value changes with voltage across the junction and parasitic capacitance whose value doesn't. The junction capacitance is given by [8]

$$C_j = \frac{\epsilon_S \epsilon_0 L_S W_S}{d} \qquad (C.19)$$

Table C.3. Theoretical Series Resistance and Capacitance of Our Planar Schottky Diode.

R_S^*	R_{n1}	R_{n2}	R_{n3}	R_c	R_{A0}	R_{A1}	R_{A2}	R_{O1}	R_{O2}
13	0	1.35	1.02	5.14	2	0.66	1.35	0.36	1.08
(15.9)**									

C_j^{***}	C_p	C_{f1}	C_{f2}
5.5	3.54	0.23	3.31

* : all resistances are in ohms.

** : measured from I-V characteristic

*** : all capacitances are in fF

where ϵ_s is the relative permittivity of GaAs (12.9 at 94 GHz) and ϵ_0 is the permittivity in vacuum (8.85×10^{-14} F/cm).

The parasitic capacitance results from the fringing electric field within the small gap between the Schottky electrode and the ohmic contact. The fringing capacitance C_{f1} on the n^+ layer as shown in Fig. C.2 can be treated as the edge capacitance of a thick electrode above the ground plane (highly conductive n^+ layer). It can be found numerically or graphically in [9]. The fringing capacitor C_{f2} on the semi-insulating area (see Fig. C.2) can be calculated by treating the section between the proton isolation boundary and the apex of the bow-tie as a coplanar waveguide [10] and the line where two bows meet as a bow-tie with very large bow angle [11]. It can be written as

$$C_{f2} = (\epsilon_s + 1)\epsilon_0 \left[2\frac{K(k_a)}{K(k'_a)}(L_1 + g/2) + \frac{K(k'_b)}{2K(k_b)}\frac{W_1 - W_S - g}{2} \right] \quad (C.20)$$

where

$$k_a = \frac{W_S}{W_S + 2g} \quad (C.21)$$

$$k'_a = \sqrt{1 - k_a^2} \quad (C.22)$$

$$k_b = \tan^2(\pi/4 - \theta/4) \quad (C.23)$$

$$\theta = \pi - \tan^{-1}\left(\frac{2g}{W_1 - W_S - g}\right) \quad (C.24)$$

$$k'_b = \sqrt{1 - k_b^2} \quad (C.25)$$

The total parasitic capacitance C_p will be

$$C_p = C_{f1} + C_{f2} \quad (C.26)$$

Table C.3 also gives the calculated results for each capacitance. One can see the parasitic capacitance is mainly attributed to the fringing field within the small gap on the semi-insulating area rather than the n^+ area. It results from the fringing field penetrating the semi-insulting substrate which has a high relative dielectric constant of 12.9.

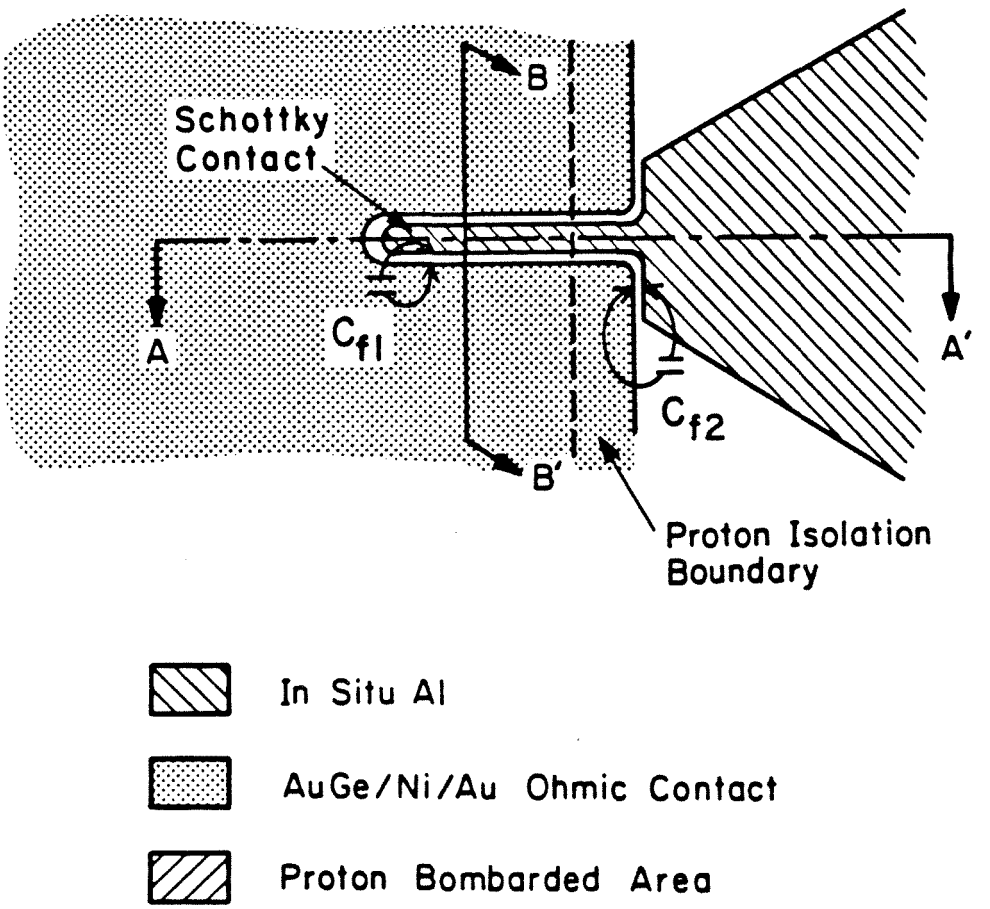

Fig. C.2. Parasitic capacitance due to the fringing field within the gap. C_{f1} is the fringing capacitance on the n^+ area and C_{f2} is the fringing capacitance on the semi-insulating area.

References

[1] H. Fukui, "Determination of the Basic Device Parameters of a GaAs MESFET," *Bell System Technical Journal*, vol. 58, pp. 771–797, Mar. 1979.

[2] S. Ramo, J. R. Whinnery, T. van Duzer, *Fields and Waves in Communication Electronics*, Chap. 4, pp. 252, John Wiley & Sons, New York, 1965.

[3] M. V. Schneider, "Metal-Semiconductor Junctions as Frequency Converters," *Infrared and Millimeter Waves*, vol. 6, Chap. 4, pp. 209–275, K. J. Button, ed., Academic Press, New York, 1983.

[4] E. R. Carlson, "Subharmonically Pumped Millimeter-Wave Mixers," *IEEE*, vol. MTT–26, pp. 706–715, Oct. 1978.

[5] L. T. Yuan, "Low Noise Octave Band with Waveguide Mixer," *IEEE*, MTT–S, pp. 480–482, 1977.

[6] H. H. Berger, "Models for Contacts to Planar Devices," *Solid-State Electronics*, vol. 15, pp. 145–158, 1972.

[7] John L. Heaton, "Analytical Model Speeds Planar-Mixer Diode Design," *Microwave & RF*, pp. 102–110, Sept. 1984.

[8] S. M. Sze, *Physical of Semiconductor Devices*, 2nd. ed., Chap. 5, pp. 245–311, John Wiley & Sons, Inc., New York, 1981.

[9] H. E. Kamchouchi and A. A. Zaky, "A Direct Method for the Calculation of the Edge Capacitance of Thick Electrodes," *J. Phys. D: Appl. Phys.*, vol. 8, 1975.

[10] K. C. Gupta, R. Grag and I. J. Bahl, "Coplanar Lines: Coplanar Waveguide and Coplanar Strips," *Microstrip Lines and Slotlines*, Chap. 7, pp. 257–301, Artech House, Inc., Dedham, Massachusetts, 1979.

[11] D. B. Rutledge and M. S. Muha, "Imaging Antenna Arrays," *IEEE*, vol. AP-30, No. 4, July 1982.

Appendix D

Theoretical Calculation of System Video Responsivity

In order to have a better understanding of a planar Schottky diode used as video detector, as well as the efficiency of the antenna, we introduce a simplified derivation of the responsivity of a planar Schottky diode detector. This method has been used by several authors [1,2,3] to study the behavior of point-contact Schottky diode video detectors in the millimeter and submillimeter wave region.

Under small signal conditions, Fig. D.1 shows equivalent circuits of a Schottky diode video detector. In the RF circuit, R_a is the antenna impedance of the bow-tie antenna on the substrate which is about 90 ohms for a 60° bow-tie on GaAs substrate [4]. γ_a is the coupling efficiency of whole system which takes account of the antenna coupling efficiency and the optical losses due to absorption and reflection in the objective lens as well as the substrate lens. P_{in} is the incident power. The junction resistance R_j and capacitance C_j of the diode depend upon the DC bias [5]. The parasitic capacitance C_p and the shunt resistance R_{sh} are also included. In the low-frequency circuit, the junction capacitance can be neglected since the modulation frequency is quite low (100 Hz–1 kHz). The load impedance $R_L \parallel 1/(j\Omega C_L)$ includes all loads such as bias resistance, lock-in amplifier input impedance and cable capacitance.

Since the diode is biased by a constant current I_B, the time average of the diode current over one RF period should remain equal to I_B. This leads to a relation between the voltage detected in the low frequency circuit V_D and the amplitude of the fundamental component of the RF signal V_d across the junction as follows [1]:

$$V_D = \frac{nkT}{q} \ln \left[I_0(qV_d/nkT) \right] \qquad (D.1)$$

where $I_0(z)$ is the modified Bessel function of first kind and zero order.

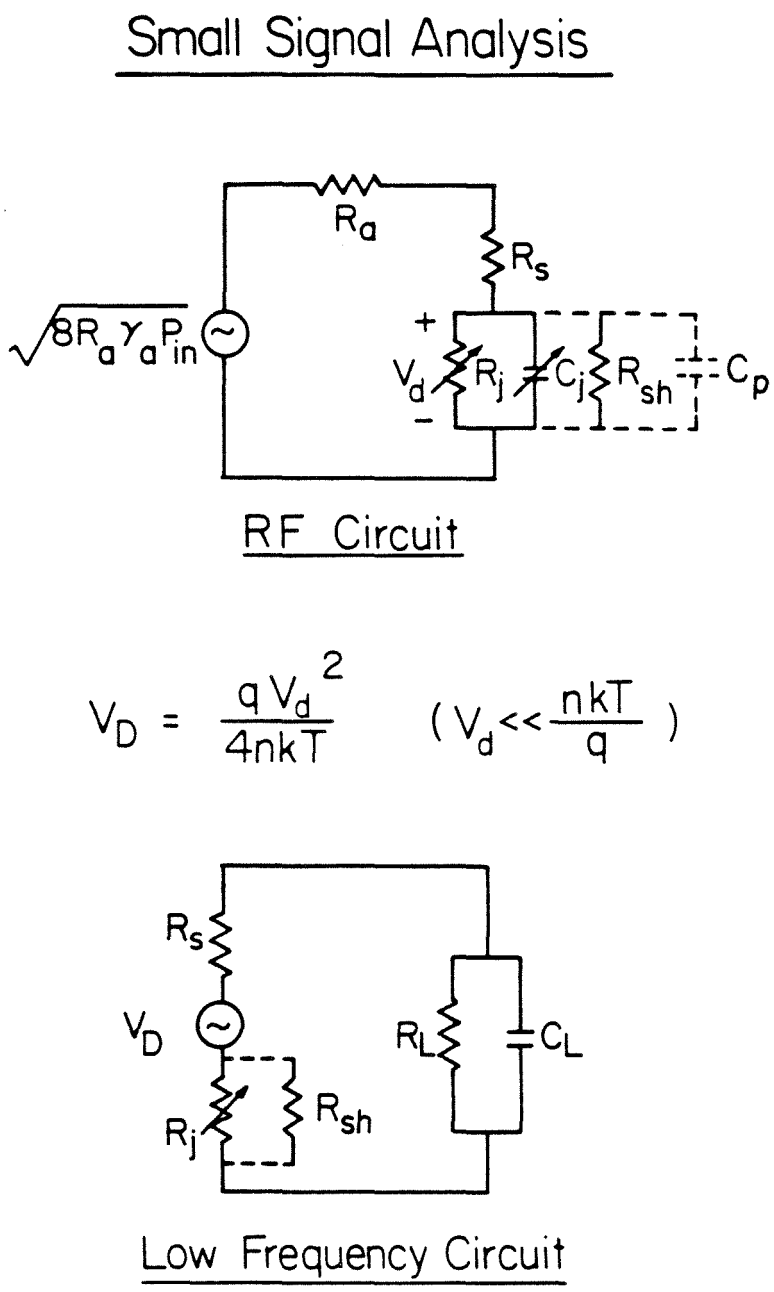

Fig. D.1. Equivalent circuits of a Schottky diode video detector.

There are two approximations, corresponding to the limits $\ln[I_0(z)] \rightarrow z^2/4$ for $z \rightarrow 0$ and $\ln[I_0(z)] \propto z$ for $z \rightarrow \infty$. By these approximations Eq. (D.1) becomes [6]

$$V_D = \frac{qV_d^2}{4nkT} \qquad \text{for } V_d \ll \frac{nkT}{q} \tag{D.2}$$

$$V_D = V_d - \frac{kT}{2q} \ln\left[\frac{2\pi q V_d}{kT}\right] \qquad \text{for } V_d \gg \frac{nkT}{q} \tag{D.3}$$

Therefore, for a small enough signal power, the diode is a square law detector. The detected voltage is proportional to the input power. When the signal power becomes large, the detection changes from square law to linear.

The system video responsivity R_v is the quotient of detected voltage and the incident power. It can be calculated from equivalent circuits in Fig. D.1.

$$R_v = R_{vi}\, \gamma_a\, \gamma_{RF}\, \gamma_{LF} \tag{D.4}$$

R_{vi} is the intrinsic video responsivity of the diode. It can be written as:

$$R_{vi} = \frac{q|Z_j|}{4nkT} \tag{D.5}$$

where $Z_j = R_j \parallel R_{sh} \parallel 1/(j\omega(C_j + C_p))$ is the junction impedance of the diode and ω is the angular frequency of the RF signal.

$$\gamma_a = \frac{\text{Power available from antenna terminals}}{\text{Incident power}} \tag{D.6}$$

$$\gamma_{RF} = \frac{\text{Power available at the junction of the diode}}{\text{Power available from antenna terminals}}$$

$$= \frac{8R_a|Z_j|}{|R_a + Z_d|^2} \tag{D.7}$$

where $Z_d = Z_j + R_s$ is the diode impedance.

$$\gamma_{LF} = \frac{\text{Voltage detected across the load}}{\text{Voltage detected across the junction of the diode}}$$

$$= \frac{R_L}{\sqrt{(R_L + R_s + R_j \parallel R_{sh})^2 + (R_s + R_j \parallel R_{sh})^2 R_L^2 C_L^2 \Omega^2}} \qquad (D.8)$$

In this work, we tested the diodes from 70 GHz to 170 GHz. These frequencies are well below the plasma resonant frequency which is about 1 THz [7]. In addition, all the epitaxial thicknesses and metal thicknesses of our planar Schottky diode are less than or about the same as the skin depth. For this reason, DC series resistance value is used in the calculation. The shunt resistance due to the diode leakage current is estimated from the reverse current by curve tracer. The zero-bias junction capacitance is estimated from the area of the diode. One can see the video responsivity is a strong function of biasing current and RF frequency. There are two estimated parameters γ_a and C_p which can be determined by curve fitting.

References

[1] A. Kreisler, M. Pyée and M. Redon, "Parameters Influencing for Infrared Videodetection with Submicron-Size Schottky Diodes," *Int. J. of Infrared and Millimeter Waves*, vol. 5, No. 4, pp. 559–584, 1984.

[2] F. L. Warner, *Millimetre and Submillimetre Waves*, Chap. 22, F. A. Benson ed., Iliffe Books Ltd., London, 1969.

[3] A. Godone and E. Bava, "The μ-Size Schottky Diodes as Detectors and Harmonic Generators in the 100 GHz–1 THz Ranges," *Int. J. of Infrared and Millimeter Waves*, vol. 2, No. 6, 1981.

[4] D. B. Rutledge, D. P. Neikirk, D. P. Kasilingam, "Integrated-Circuit Antenna," *Infrared and Millimeter Waves*, vol. 10, Chap. 1, pp. 1–90, K. J. Button, ed., Academic Press, New York, 1983.

[5] S. M. Sze *Physics of Semiconductor Devices*, Chap. 5, 2nd ed., John Wiley & Sons, Inc., New York, 1981.

[6] S. Wetenkamp, "Comparison of Single Diode vs. Dual Diode Detectors for Microwave Power Detection," *IEEE MTT-S*, pp. 361–365, 1983.

[7] M. V. Schneider, "Metal-Semiconductor Junctions as Frequency Converters," *Infrared and Millimeter Waves*, vol. 6, Chap. 4, pp. 209–275, K. J. Button, ed., Academic Press, New York, 1983.

Appendix E

Diplexer

In the millimeter and submillimeter wave region, there are various quasi-optical diplexers available for heterodyne detections to combine signal power and local oscillator power into a single beam [1,2]. Two diplexers have been tried in our experiments. Fig. E.1 shows a simple beam splitter made out of 10 mil mylar. The mylar has an index of refraction 1.83 [3]. The reflectance and the transmittance depend on the film thickness as well as the incident angle and the polarization of the in-coming wave. Fig. E.2 shows the theoretical reflectance and transmittance of a 10 mil mylar set at an angle of 45° to the in-coming wave with perpendicular polarization. Airy's formulas [4] are used in the calculation. The circle shows the measured 94 GHz transmittance, which is quite close to the calculated result. Fig. E.3 shows a mylar beam splitter used in our heterodyne measurement. Although this beam splitter is simple to make, it only transmits 65% (−1.9 dB) of the 94 GHz signal power and reflects 34% (−4.7 dB) of the 91 GHz local oscillator power to the receiver.

Due to lack of power in the millimeter region, it is desirable to combine the signal power and local oscillator power without any loss. Fig. E.4 shows a more elaborate diplexer, based on a Mach-Zehnder interferometer. Both signal power and local oscillator power are split into two beams at the first beam splitter and recombined at the second beam splitter after traveling two seperate paths differed by $2d$. The transmittance from port 1 to port 3 and from port 2 to port 3 are given by [5]

$$T_{1\to 3} = 1 - 2R(1-R)\left[1+\cos\left(\frac{4\pi d}{\lambda}\right)\right] \qquad (E.1)$$

$$T_{2\to 3} = 2R(1-R)\left[1+\cos\left(\frac{4\pi d}{\lambda}\right)\right] \qquad (E.2)$$

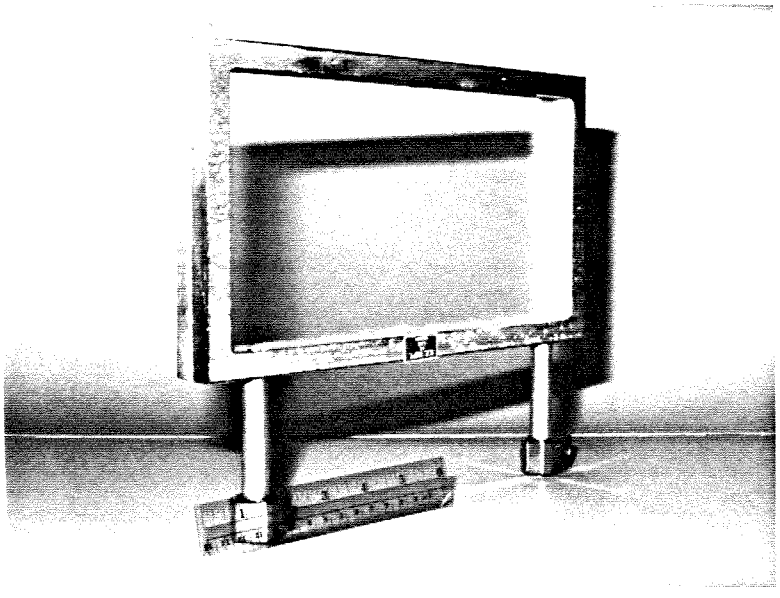

Fig. E.1. Photograph of a simple mylar beam splitter.

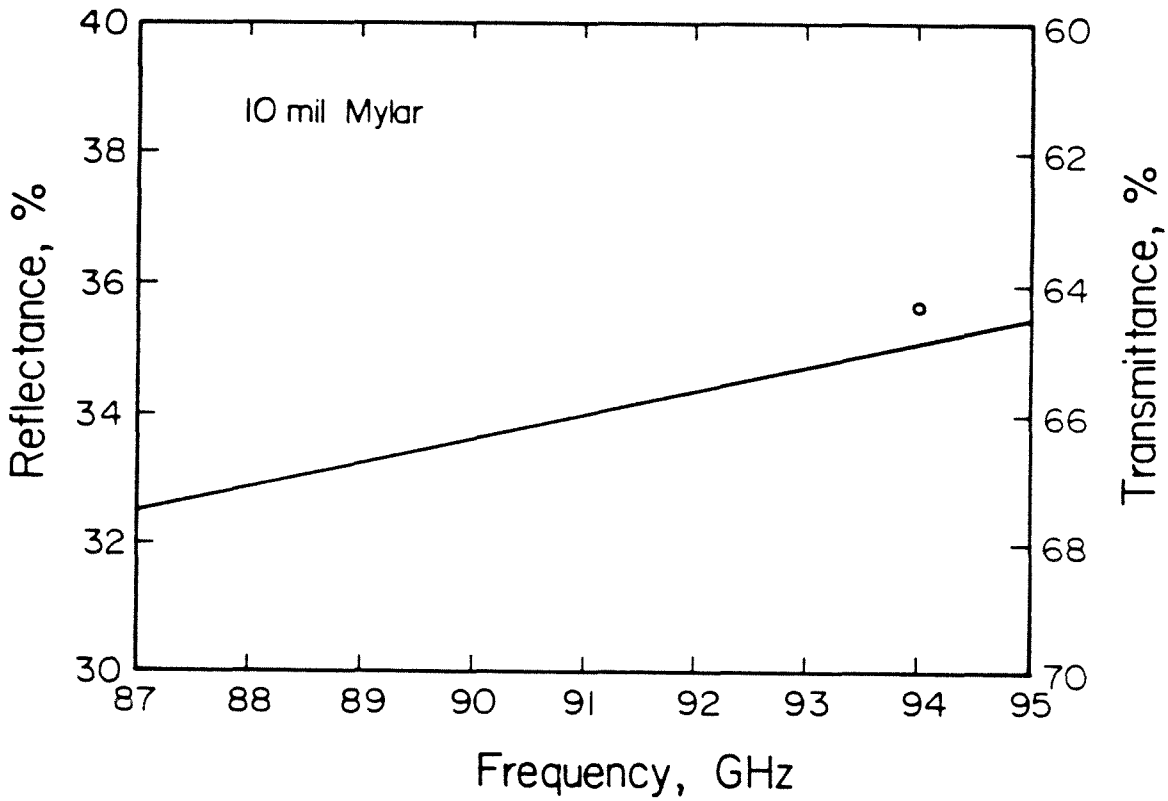

Fig. E.2. Theoretical reflectance and transmittance of a 10 mil mylar set at angle of 45° to the in-coming wave with perpendicular polarization. The circle is a measured result at 94 GHz.

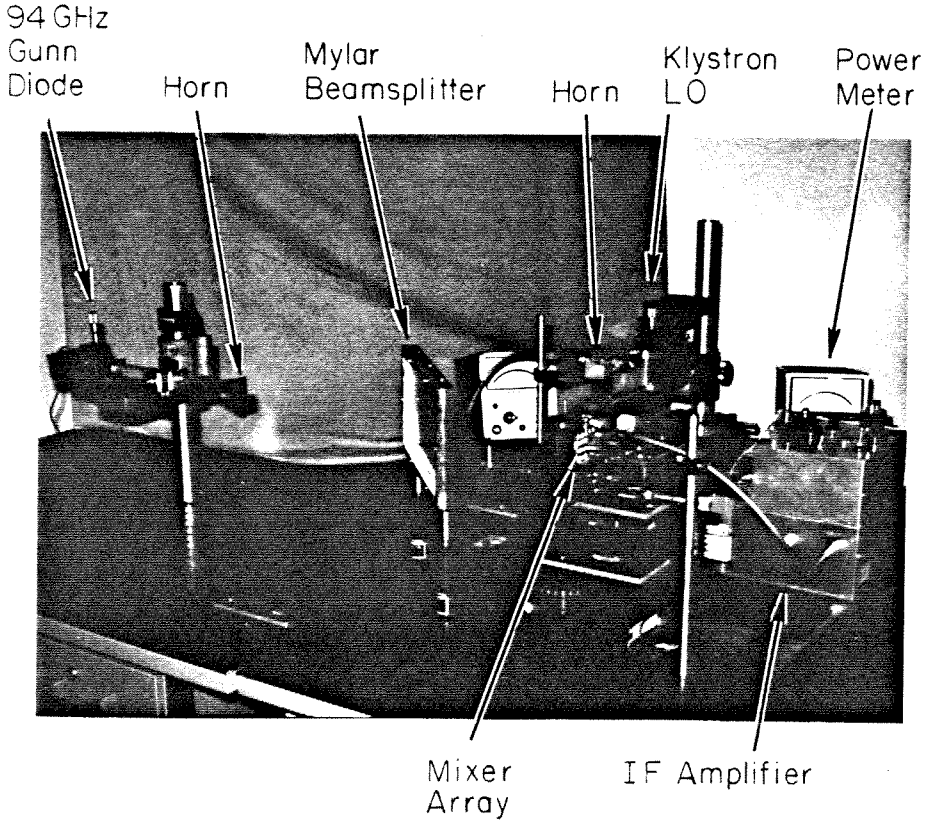

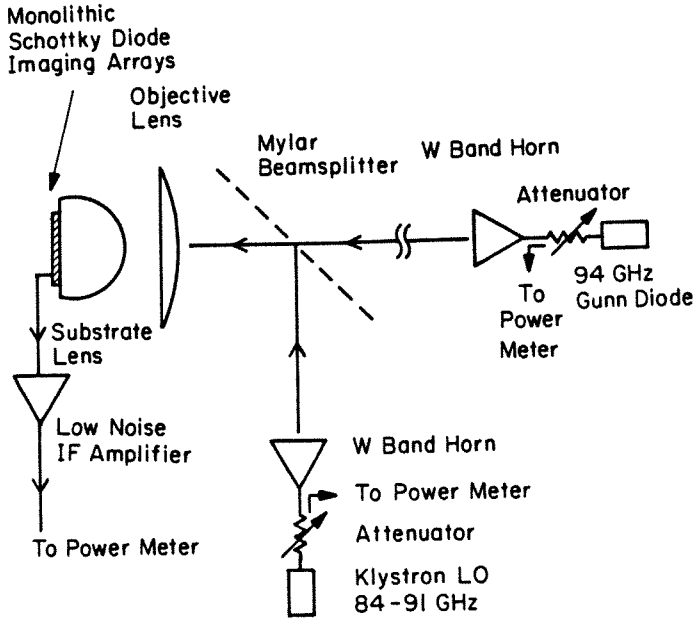

Fig. E.3. Photograph of our single sideband heterodyne measurement set-up using a mylar beam splitter (top). Schematic drawing of set-up (bottom).

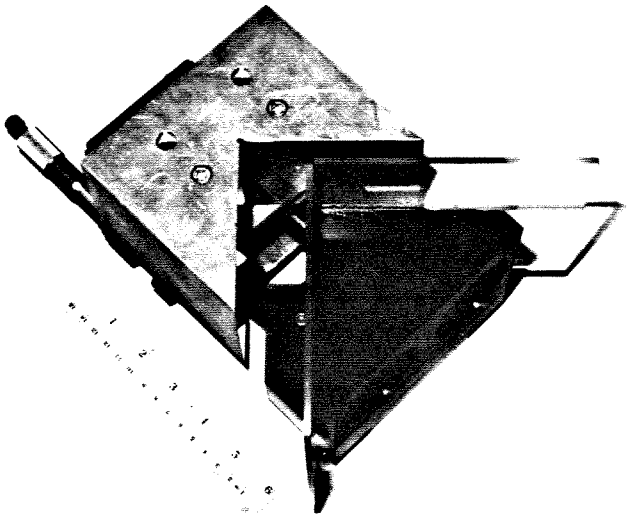

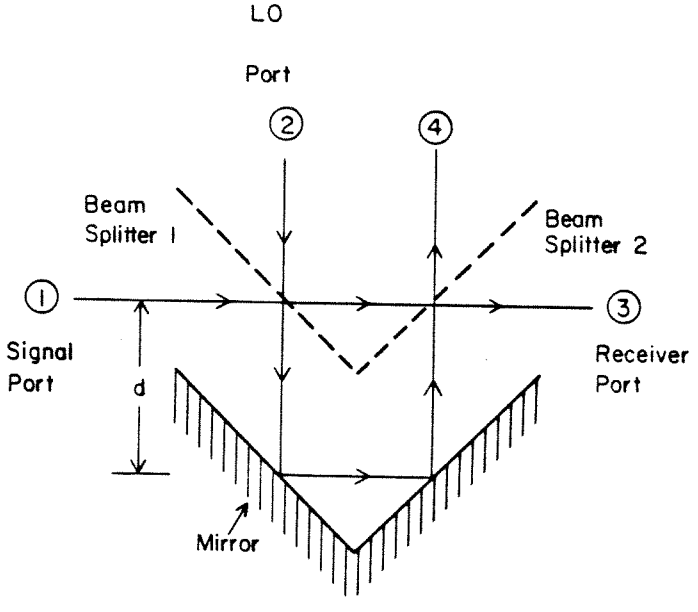

Fig. E.4. Photograph of a dual-beam Interferometer (top). Schematic drawing of the dual-beam Interferometer (bottom). The path length difference $2d$ can be adjusted by a micrometer to reach the resonant condition.

where R is the reflectance of the beam splitter and λ is the wavelength. In order to have maximum transmittance for both signal power and local oscillator power, one need to choose

$$2d \approx (2k-1)(\lambda_{IF}/2) \qquad k = 1, 2, 3\cdots \tag{E.3}$$

where λ_{IF} is the wavelength of IF signal. Since $(T_{13})max = 1$ and $(T_{23})max = 4R(1-R) \leq 1$, we always choose port 1 as signal port, port 2 as local oscillator port and port 3 as receiver port. Besides, R should be close to 0.5 to have $(T_{23})max$ close to 1.

Fig. E.5 shows the theoretical reflectance of our quartz beam splitter with a thickness of 129 mil. This thickness is chosen because it gives 50% reflectance at our local oscillator frequency (91 GHz) and is in stock on the market. The absorption loss of this beam splitter calculated from data in [6] is negligible (-0.03 dB). This interferometer is designed for a 1.4 GHz IF frequency with $k = 1$ in Eq. (E.3). In our hot and cold measurements, the dual-beam interferometer is tuned for a local oscillator frequency of 91 GHz and a IF frequency of 1.4 GHz. Fig. E.6 shows the calculated response. One can see that both sidebands are coupled to the receiver port. Since the noise from the hot and cold loads is broadband, a double sideband mixer conversion loss and noise temperature are measured. The instantaneous bandwidth is determined by the IF amplifier chain. This diplexer not only uses all the available power but also suppresses local oscillator noise within sidebands. During the experiments, d is set to be 5.3 cm to start with. Then the interferometer is tuned by a micrometer to maximize the transmittance from local oscillator port to receiver port. At the same time, the transmittance from signal port to receiver port will be maximized automatically.

In our single sideband heterodyne measurement, the IF frequency is 3 GHz ($f_{LO} = 91$ GHz and $f_{USB} = 94$ GHz). In order to use the same diplexer without

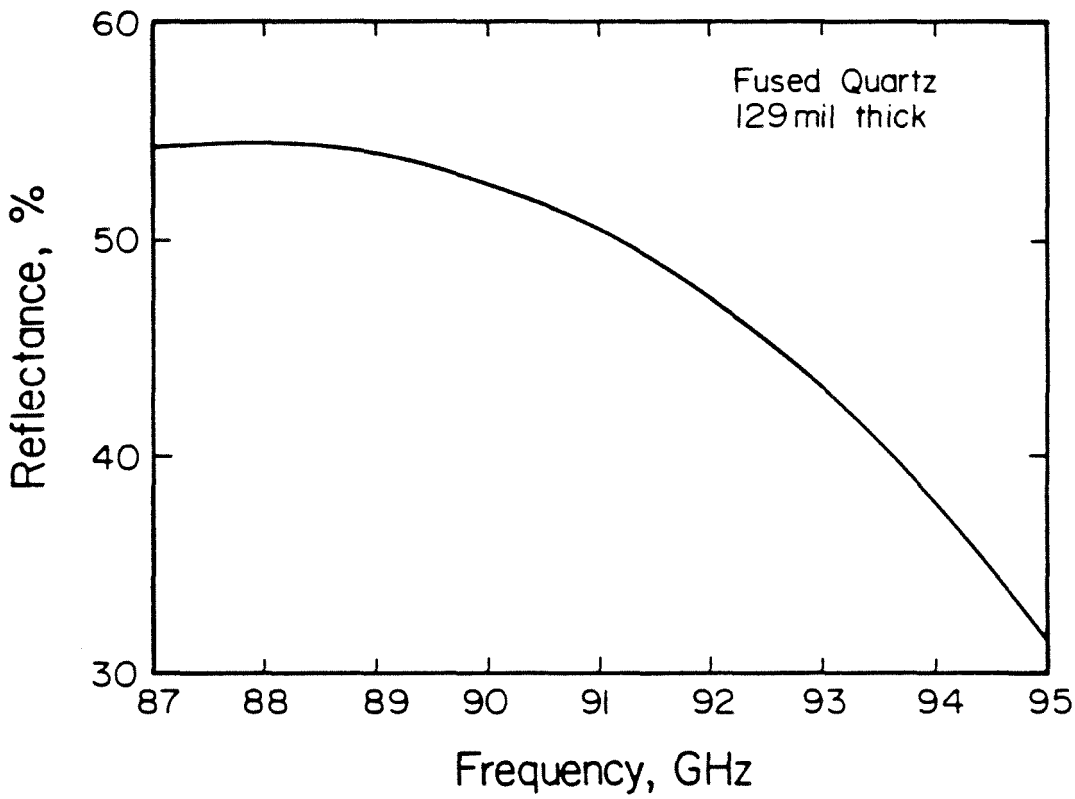

Fig. E.5. Theoretical reflectance of a quartz beam splitter set at 45° angle for perpendicular polarization. Its thickness is 129 mil.

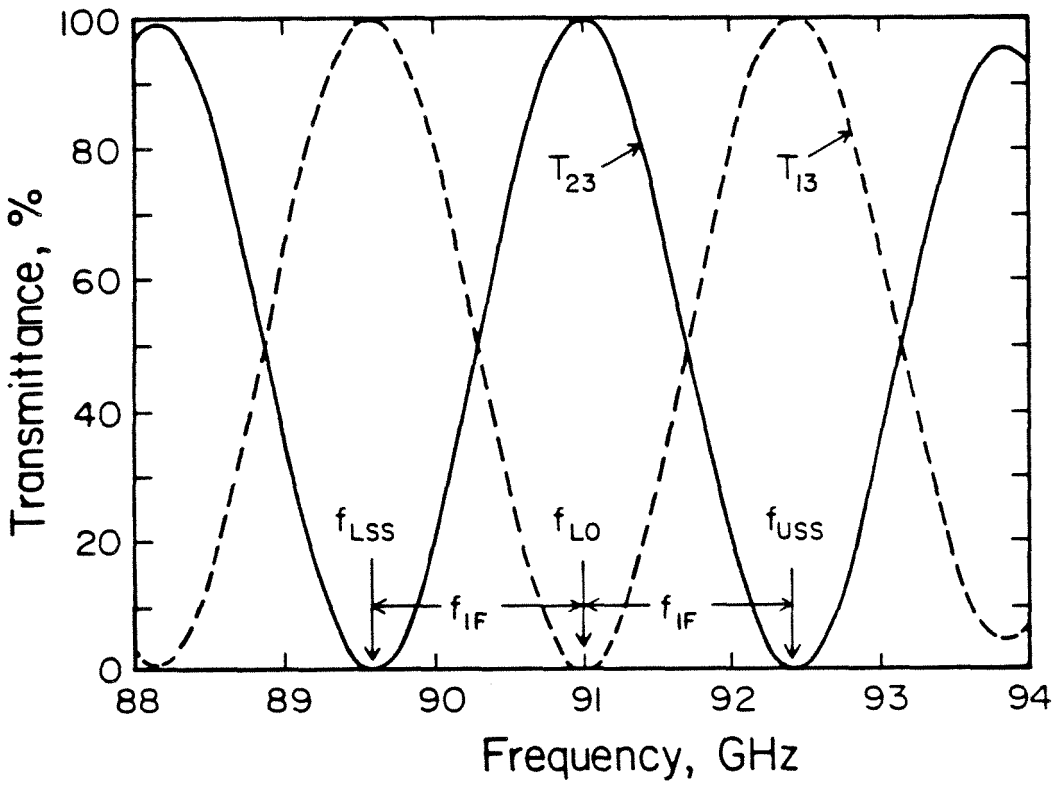

Fig. E.6. Calculated response of dual-beam interferometer tuned for a local oscillator frequency of 91 GHz and a IF frequency of 1.4 GHz. ($d = 5.275$ cm)

reducing apertures of ports 1 and 3, we choose $k = 3$ in Eq. (E.3). Fig. E.7 shows the calculated response. The bandwidth of sidebands is 3 times narrower than that of $k = 1$ shown in Fig. E.6. However, the signal is generated by a 94 GHz Gunn diode with a bandwidth much narrower than that of the diplexer. The diplexer is tuned to the resonant condition by the following procedure. First, d is set to be 7.5 cm. Then, adjusting the micrometer maximizes transmittance from signal port to receiver port. Finally, the transmittance from local oscillator port to receiver port is optimized by fine adjusting local oscillator frequency with a mechanical tuner of klystron.

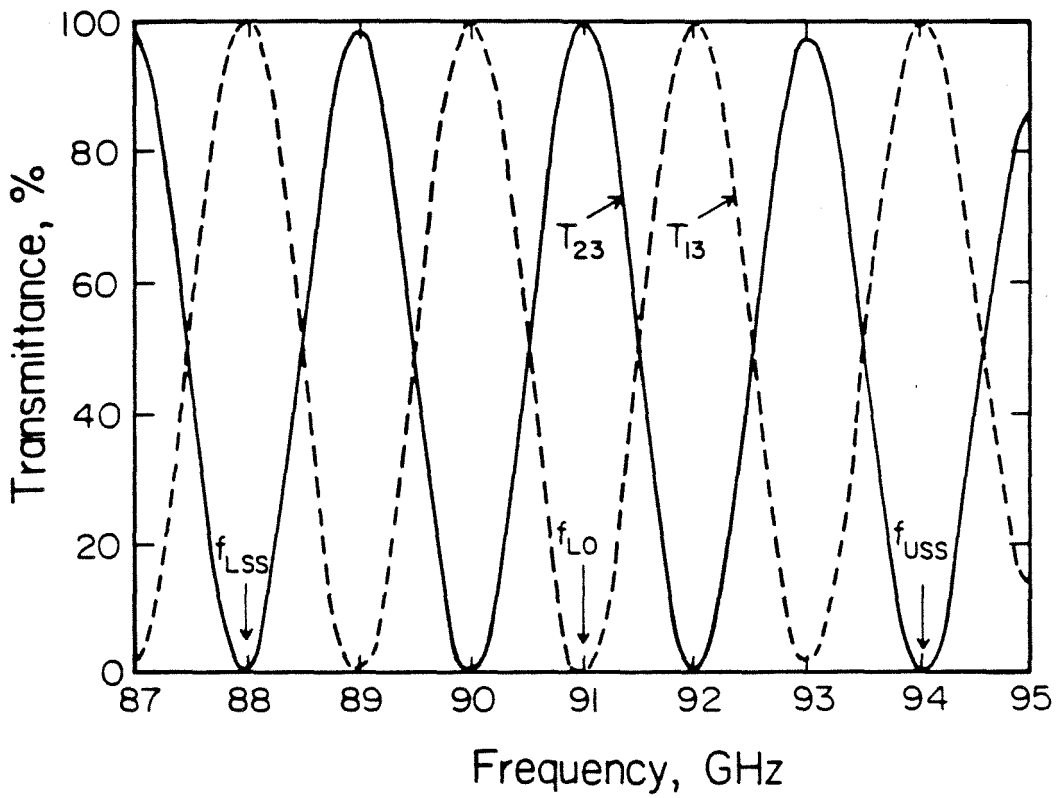

Fig. E.7. Calculated response of dual-beam interferometer tuned for a local oscillator frequency of 91 GHz and a signal frequency of 94 GHz. ($d = 7.418$ cm)

References

[1] Perry Miles, "High Efficiency Optical Diplexers," *Applied Optics*, vol. 21, No. 8, pp. 1367–1372, Apr. 1982.

[2] G. T. Wrixon and W. M. Kelly, "Low Noise Schottky Barrier Diode Mixers for Wavelengths < 1 mm," *Infrared Physics*, vol. 18, pp. 413–428, 1978.

[3] F. Sovel, F. L. Wentworth and J. C. Wiltse, "Quasi-Optical Surface Waveguide and Other Components for 100 to 300–Gc Region," *IRE*, vol. MTT, pp. 512–518, Nov. 1961.

[4] M. Born and E. Wolf, *Principles of Optics*, 6th ed., Chap. 7, pp. 323–329, Pergamon Press, Oxford.

[5] P. F. Goldsmith, "Quasi-Optical Techniques at Millimeter and Submillimeter Wavelengths," *Infrared and Millimeter Waves*, vol. 6, Chap. 5, pp. 277–343, K. I. Button, ed., Academic Press, New York, 1983.

[6] M. N. Afsar and K. J. Button, "Millimeter-Wave Dielectric Properties of Materials," *Infrared and MIllimeter Waves*, vol. 12, Chap. 1, pp. 1–42, K. J. Button, ed., Academic Press, New York, 1984.

Appendix F

Hot and Cold Load Measurements

The conversion loss and the noise temperature of a millimeter-wave receiver are often measured by putting hot and cold loads alternately in front of the receiver, since other well-calibrated noise sources are not available. The noise power delivered to the receiver in a single polarization from a perfectly matched (black body) load at an absolute physical temperature T is given by [1]

$$P_L = \frac{h\nu B}{\exp(h\nu/kT) - 1} \qquad (F.1)$$

where k is Boltzmann's constant ($1.38 \times 10^{-23}\ J \cdot K^{-1}$), B is the receiver bandwidth, h is Planck's constant ($6.626 \times 10^{-34}\ J \cdot s$), and ν is the frequency. In the millimeter wave region, one can apply the Rayleigh-Jeans approximation to the Planck distribution since $h\nu/k = 4.8°K$ at 100 GHz frequency is much less than room temperature and liquid nitrogen temperature. A simple relation between the available power to the receiver and the physical load temperature can be written as

$$P_L = kTB \qquad h\nu \ll kT \qquad (F.2)$$

For convenience, the microwave absorber (ECCOSORB CV3) at room temperature (295°K) serves as a hot load. From specifications, the reflected power is 40 dB down at 96 GHz up to incidence angles of at least 70° [2]. The cold load is the same absorber soaked with liquid nitrogen (77°K) in a styrofoam box and is reflected to the receiver by a metallic mirror. The power reflection coefficient at the liquid nitrogen surface is 0.03 (15.56 dB), calculated from the index of refraction of liquid nitrogen (1.4) at low frequencies [3]. The absorber must cover the whole antenna beam width to get an accurate measurement. Experiments are performed by recording the receiver output powers (P_H and P_C) due to the

hot and cold loads (T_H and T_C). The gain G and the noise temperature T_R of the entire receiver are calculated by [4].

$$G = \frac{P_H - P_C}{T_H - T_C} \cdot \frac{1}{kB} \tag{F.3}$$

$$T_R = \frac{T_H - Y T_C}{Y - 1} \tag{F.4}$$

where $Y = P_H/P_C$. Fig. F.1 shows output power versus input load temperature. One can obtain the noise temperature from the X intercept and the gain from the slope.

In order to measure the output power due to the temperature load by the HP 435B power meter, a low noise IF amplifier chain with 80 dB gain and 106°K noise temperature is used to amplify the output power of the mixer. Fig. F.2 shows its photograph and circuit diagram. The mixer conversion loss L_M and the mixer noise temperature T_M are calculated by

$$L_M = G_{IF} - G \tag{F.5}$$

$$T_M = T_R - L_M T_{IF} \tag{F.6}$$

where G_{IF} and T_{IF} are the gain and the noise temperature of the IF amplifier chain. L_M and T_M include the loss and the noise from mixer itself and the system but not from the IF amplifier chain. The IF amplifier chain is calibrated by the same method. The SMA 50 Ω terminations at room temperature and liquid nitrogen temperature are used as loads instead of absorbers. Since the noise from the black body radiation is broad band and is accepted by the receiver at both signal and image frequencies, double-sideband mixer conversion loss and noise temperature are obtained by this way.

Hot and Cold Load Measurements

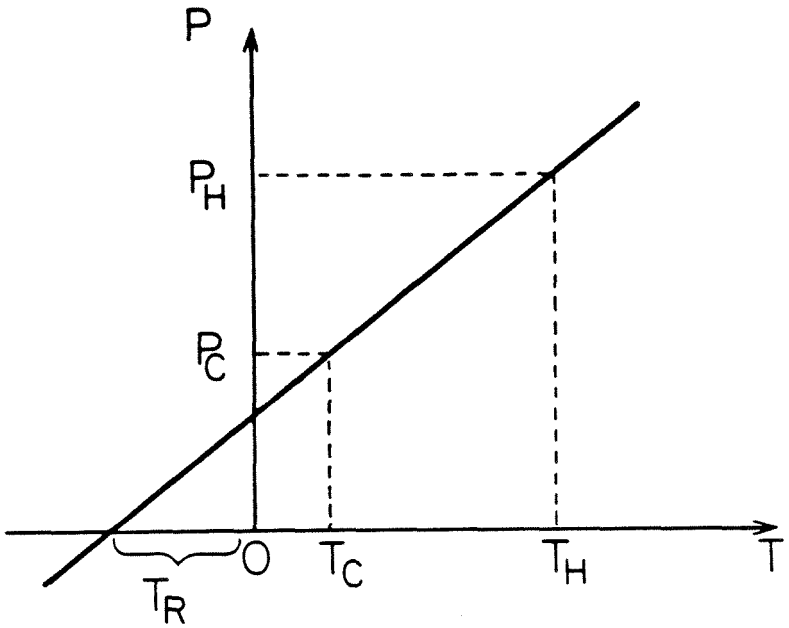

$$G = \frac{P_H - P_C}{T_H - T_C} \cdot \frac{1}{kB}$$

$$Y = \frac{P_H}{P_C}$$

$$T_R = \frac{T_H - Y T_C}{Y - 1}$$

Fig. F.1. Receiver output power versus input load temperature. The X intercept gives the receiver noise temperature and the slope is related to the gain.

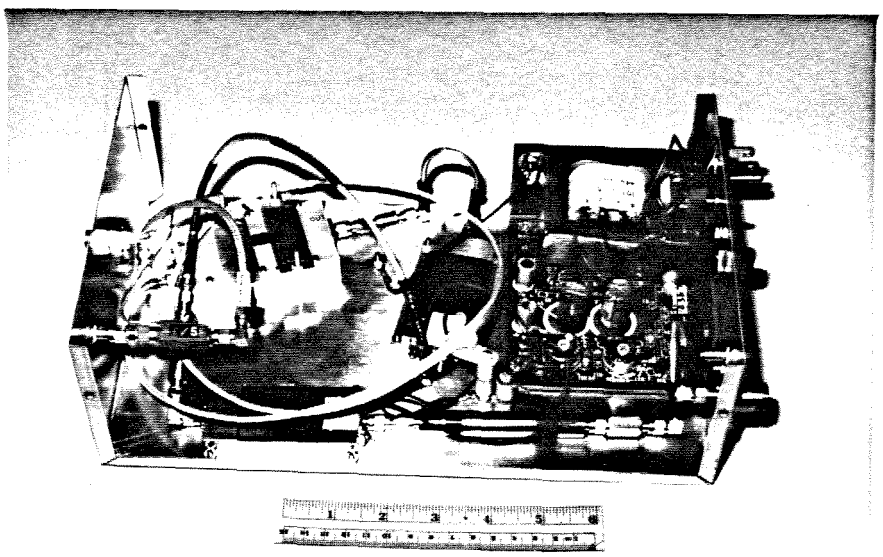

Fig. F.2a. Photograph of low noise IF amplifier chain with 80 dB gain and 106°K noise temperature.

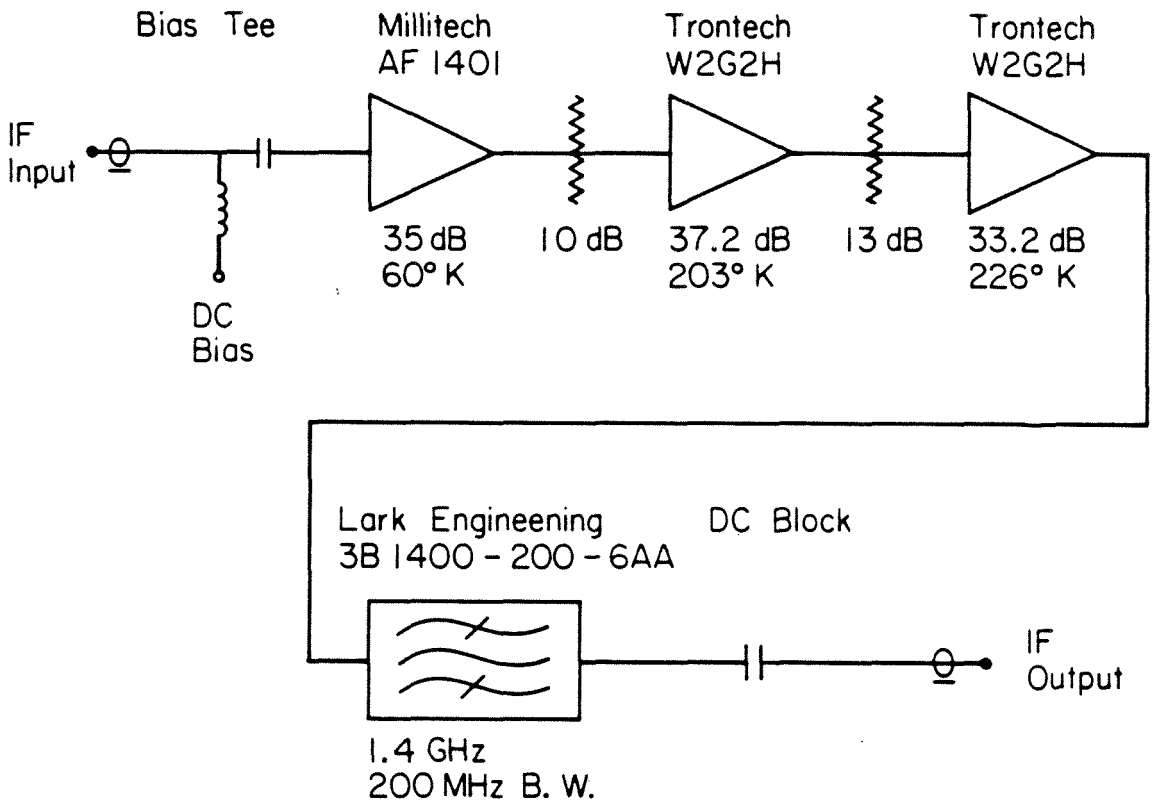

Fig. F.2b. Circuit diagram. The gain and the noise temperature of each amplifier from specification are written below each amplifier.

References

[1] B. L. Ulich et al., "Absolute Brightness Temperature Measurements at 3.5-mm Wavelength," *IEEE*, vol. AP-28, No. 3, pp. 367–377, May 1980.

[2] Technical Bulletin 8–2–14, Emerson & Cuming.

[3] P. F. Goldsmith, "A Quasioptical Feed System for Radioastronomical Observations at Millimeter Wavelength," *the Bell system Technical Journal*, pp. 1483–1501, Oct. 1977.

[4] Bernd Vowinkd, "Simplified Receiver Response Measurement," *Microwave & RF*, pp. 147–148, Mar. 1984.